



SAPIENZA
UNIVERSITÀ DI ROMA

Sapienza University of Rome

Dipartimento di Fisica
PhD in Accelerator Physics

THESIS FOR THE DEGREE OF DOCTOR OF PHILOSOPHY

Beam coupling impedance and collective effects for the Future Circular Lepton Collider

Thesis Advisor
Mauro Migliorati
Frank Zimmermann

Candidate
Emanuela Carideo
1889107

*A mia madre sempre nel mio cuore e nei
miei pensieri*

*To you who are the first to believe in
myself and support me, always*

Abstract

Improving the accuracy of the impedance model of an accelerator is important in order to keep beam instabilities and power loss under control. This is particularly relevant in the context of the FCC–ee, a future electron–positron circular collider that requires very intense multi-bunch colliding beams with a very small transverse beam size at the collision points. Achieving this high beam quality while avoiding machine performance degradation poses a major challenge, and requires a careful study of collective effects and identification of stabilizing mechanisms.

To address this challenge, the FCC–ee impedance model is being constantly updated to closely follow the vacuum chamber design and parameter evolution. The impedance database is also becoming more complete and the impedance model is being refined. These updates are important to accurately evaluate the longitudinal microwave instability threshold, which can be done using a time domain macro–particle tracking code such as PyHEADTAIL.

Two collective effects codes will be compared on results of the transverse beam dynamics: PyHEADTAIL and DELPHI, a Vlasov equation solver. Both are important to estimate coherent beam stability margins for FCC–ee.

Moreover, we present the results of beam dynamics simulations, including both the longitudinal and transverse wakefields, to evaluate the influence of the bunch length on the transverse mode coupling instability.

Overall, studying collective effects and identifying stabilizing mechanisms is crucial to preserve high beam quality and avoid machine performance degradation in the FCC–ee and other high intensity particle accelerators.

Contents

List of Figures	vi
List of Tables	x
Nomenclature	xii
Introduction	1
1 CERN accelerator complex	2
1.1 The Future Circular Collider	4
1.1.1 Introduction	4
1.1.2 Machine layout and beam parameters	6
1.1.3 FCC project: State-of-the-art	10
2 Collective effects	12
2.1 Introduction	12
2.1.1 Wakefields and Impedances	13
2.1.2 Wake potentials and loss factors	15
2.2 Pipe Model	18
2.3 Simulation codes:	19
2.3.1 ImpedanceWake2D	19
2.3.2 PyHEADTAIL	25
2.4 PyHT simulations: Wake potentials	26
2.5 Machine Devices	31
2.5.1 Wake potential and loss factor	31
2.5.2 Collimator system	39
2.6 FCC Impedance Repository	43
3 Collective effects: Longitudinal plane	45
3.1 Microwave instability	45
3.1.1 New parameters for the longitudinal dynamics analysis	47
3.2 Interplay between beam-beam and longitudinal impedance	49
4 Collective effects: Transverse plane	54
4.1 PyHEADTAIL and Delphi	54
4.1.1 Longitudinal wakefield in the transverse dynamics	56
4.1.2 PyHEADTAIL simulations: new devices and parameters	59
5 Mitigation	61
5.1 Chromaticity	61
5.2 Higher momentum compaction	63
5.3 Higher harmonic cavity	68

5.4	Feedback system and transverse coupled beam instability.	69
5.5	Reduction of β function at the interaction point	75
6	Conclusion	78
	Bibliography	80
	Acknowledgement	86

List of Figures

1.1	The new CERN accelerator complex. The circumference and first year of operation of each accelerator are indicated, as well as the particle species that can be accelerated.	3
1.2	Schematic view of the FCC tunnel in the Geneva area.	5
1.3	Expected baseline luminosities of the current worldwide lepton colliders as a function of the center-of-mass energy. The variable s on the x-axis is the Mandelstam variable and \sqrt{s} represents the total center-of-mass energy during collision[1].	6
1.4	Technical schedule of the FCC integrated project with year 1 equal to 2021 [2]	7
1.5	Schematic FCC-ee layout and its booster with a circumference of 91.2 km and four IP	9
1.6	On the left, schematic layout of the pre-injector chain and, on the right, the injector complex.	10
2.1	Reference system with a source particle q_1 (in red) and a test particle q_2 (in green)[1].	14
2.2	Example of longitudinal (top) and transverse (bottom) wake functions for ultra-relativistic particles ($\beta = 1$)[1].	15
2.3	Integral transformation to compute the energy loss of a slice due to the entire bunch [1].	16
2.4	On the left, the vacuum chamber model and on the right, the four simulated layers. .	18
2.5	Real and imaginary part of the longitudinal resistive wall impedance, calculated by IW2D	19
2.6	Longitudinal and transverse impedances, respectively, for the case of 150 nm and 100 nm of NEG.	20
2.7	Real (top) and imaginary (bottom) part of the impedance, for the case of 200 nm and 100 nm of NEG.	21
2.8	PyHT simulation results. Bunch length and energy spread as a function of intensity for three different NEG thickness models: 200 nm, 150 nm, and 100nm.	22
2.9	CST pipe shape model considering a more realistic representation, without neglecting lateral winglets.	23
2.10	Resistive wall longitudinal (top) and transverse (bottom) impedance for FCC-ee obtained with CST considering the realistic model of the winglets and compared with the results of IW2D with four layers for a circular pipe, and multiplied by a factor 1.1 [3].	24
2.11	The figure shows the principle of beam slicing for PyHT. On the left, the bunch is represented as a collection of macro-particles. We have to evaluate the effect of the wakefield generated by all the macro-particles on the red one. In order to decrease the calculation time, the bunch is instead sliced as pictured on the right. In each slice there are several thousands of macro-particles, and it is the effect of all slices on the red one that is computed. Pictures courtesy of M.Schenk [4]	25
2.12	Energy spread (top) and bunch length (bottom) for different values of slices with a nominal bunch length of 3.5 mm and using the same number of macro-particles. .	27
2.13	Energy spread (on the top) and bunch length (on the bottom) as a function of bunch population using, as pseudo Green function, the wake of different short bunches, 0.4 mm, 0.35 mm and 0.31 mm.	28

2.14 Wake potential for a Bellow of a 3.5 mm Gaussian bunch obtained directly by CST (blue curve) and with the convolution by using the wake potential of 0.4 mm Gaussian bunch (orange dots), the "pseudo Green-function".	29
2.15 Wake potential for a Bellow of a 12.1 mm Gaussian bunch obtained directly by CST (blue curve) and with the convolution by using the wake potential of 0.4 mm Gaussian bunch (orange curve), the "pseudo Green-function".	29
2.16 Wake potential for an RF cavity of a 3.5 (left) and 12.1 mm Gaussian bunch (right) obtained directly by CST (blue line), with convolution by using the wake potential of 0.4 mm Gaussian bunch (green line) and with the result obtained directly by ABCI (orange line), the "pseudo Green-function".	30
2.17 Wake potential for a BPM 3.5 and 12.1 mm Gaussian bunch obtained directly by CST (blue line) and with the convolution using the wake potential of 0.4 mm Gaussian bunch (orange line), the "pseudo Green-function".	30
2.18 Wake potential for Taper of 3.5 and 12.1 mm Gaussian bunch obtained directly by ABCI (blue line) and with the convolution using the wake potential of 0.4 mm Gaussian bunch (orange line), the "pseudo Green-function".	30
2.19 Resistive wall wake potential of a 3.5 mm Gaussian bunch (blue line) and the wake potential obtained as convolution by using the wakefield (orange curve).	31
2.20 Longitudinal wake potentials for a Gaussian bunch with nominal bunch length $\sigma_z = 3.5\text{mm}$ due to the main FCC-ee components, considering an old configuration machine.	33
2.21 Simulated models of FCC-ee beam vacuum chamber including bellows. On the left there is a simplified model with circular geometry (Circular, green line in the Fig. 2.22), in the centre a simplified model with winglets (Winglets, orange line in the Fig. 2.22), , on the right the realistic model of the bellow including RF fingers (Realistic, blue line in the Fig. 2.22).	34
2.22 Longitudinal wake potential and impedance for the three studied models of the bellow.	34
2.23 Comparison between the induced voltage (total wake multiplied by the bunch charge) produced by 8000 bellows (blue line) and, 20000 bellows (red line) for the same machine configuration, bunch length of 3.5 mm.	35
2.24 Microwave instability analysis considering a number of 8000 bellows and a number of 20000 bellows. Shown are the rms bunch length in mm (top) and the rms energy spread in % (bottom) as a function of the bunch population in units of 10^{10} . The microwave threshold is reached where the energy spread starts to increase.	36
2.25 Longitudinal wake potential for a 0.4 mm Gaussian bunch due to different devices using the new machine parameters and used as input for beam dynamics simulations	37
2.26 Transverse dipolar wake potential for a 0.4 mm Gaussian bunch due to different devices using the new machine parameters.	38
2.27 CST perspective view of the four-button BPM.	38
2.28 CST collimator models for the SuperKEKB (thanks to Takuya Ishibashi), on the left, and for the FCC-ee, on the right.	39
2.29 Schemes for the collimator models. On the top the scheme of the SuperKEKB model and on the bottom the FCC one.	40
2.30 For the resistive wall contribution we suppose parallel plates with infinite thickness and use IW2D for the impedance and wakefield evaluation.	41
2.31 Dipolar vertical (left) and horizontal impedance (right) of the collimator system.	41
2.32 Real and imaginary part of the total longitudinal impedance.	42
2.33 Real and imaginary part of the total dipolar transverse impedance.	42
2.34 Real and imaginary part of the total quadrupolar transverse impedance.	42
2.35 Geometric longitudinal wake potential of a 5 mm Gaussian bunch from ECHO3D and CST [5].	43
2.36 Online FCC-ee repository page [6].	44

3.1	Longitudinal phase space at different phases of the synchrotron oscillations with the machine parameters of Table 2.1, a bunch population of 22×10^{10}	45
3.2	RMS bunch length in units of mm (left) and RMS energy spread in % (right), as a function of bunch population in units of 10^{10} , considering only the longitudinal RW and for the parameters of Table 2.1.	46
3.3	Microwave instabilities analysis, RMS bunch length (bottom) and RMS energy spread (top), for the parameters of table 2.1, as a function of bunch population in the case without (red curve) and with (green curve) beamstrahlung effect, which is considered here independent of beam intensity.	47
3.4	Bunch shape distortion at nominal intensity in the single operational mode.	47
3.5	RMS bunch length (bottom) and RMS energy spread (top) for the new parameters of Table 1.2, as a function of the bunch population in the case with (BS) and without (SR) beamstrahlung, which is considered here independent of beam intensity.	48
3.6	Bunch length (left) and RMS energy spread (right) as a function of bunch population in the 3 different cases to understand the influence of the transverse impedance on the longitudinal dynamics.	49
3.7	Collision with large Piwinski angle [7].	49
3.8	Comparison between IBB, orange line, and PyHEADTAIL, blue line, of energy spread σ_p (top) and bunch length σ_z (bottom) as a function of the bunch population without collision[3].	51
3.9	Blow-up of the horizontal beam size σ_x/σ_{x_0} as a function of the bunch population and of the horizontal tune scan without impedance [3].	52
3.10	Blow-up of the horizontal beam size σ_x/σ_{x_0} as a function of the bunch population and of the horizontal tune scan, if including the impedance [3].	52
3.11	Bunch length (left) and energy spread (right) at the nominal bunch population as a function of the horizontal betatron tune [3].	53
4.1	The real part of the frequency shift of the first coherent oscillation modes as a function of the bunch population corresponds to non-colliding bunches, without beamstrahlung, by considering only the RW impedance produced by a NEG film with 150 nm thickness given by IW2D. The green dots represent the Delphi results, instead the colours come from PyHEADTAIL simulations which are proportional to the amplitude of the frequency spectrum of the various moments of the distribution: red corresponds to the largest amplitude, blue to the lack of signal.	55
4.2	Real part of the coherent tune shift as a function of intensity considering the longitudinal resistive wall wakefield and non-colliding bunches, by using PyHEADTAIL. .	56
4.3	Real part of the frequency shift of the first coherent oscillation modes as a function of the bunch population for a non-colliding bunches and by considering both the longitudinal and transverse RW impedance produced by a NEG film with 150 nm thickness, given by IW2D.	57
4.4	Real part of the frequency shift of the first coherent oscillation modes as a function of the bunch population by considering transverse RW and colliding bunches, so with a bunch length of 12.1 mm.	58
4.5	Real part of the frequency shift of the first coherent oscillation modes as a function of the bunch population by considering both longitudinal and transverse RW impedance produced by a NEG film with 150 nm thickness and colliding bunches, so with a bunch length of 12.1 mm.	58
4.6	Real part of the frequency shift of the first coherent oscillation modes as a function of the bunch population with a nominal bunch length of 4.37 mm, by considering only the transverse wakefield and non-colliding bunches.	59

4.7	Real part of the frequency shift of the first coherent oscillation modes as a function of the bunch population by considering both the transverse and longitudinal wakefields and non-colliding bunches.	60
4.8	TMCI: Longitudinal and transverse wake by considering colliding bunches, so with a nominal bunch length of 14.5 mm (BS)	60
5.1	Real part of the frequency shift of the first coherent oscillation modes as a function of the bunch population without beamstrahlung, with a value of chromacity of +5.	62
5.2	Real part of the frequency shift of the first coherent oscillation modes as a function of the bunch population, with a value of Chromaticity of +50.	62
5.3	Real part of the frequency shift of the first coherent oscillation modes as a function of the bunch population without beamstrahlung, with a value of Chromaticity of -5.	63
5.4	RMS Energy spread and bunch length of the longitudinal RW with the parameters of Table 2.1 and considering a NEG of 100 nm, with two different momentum compaction factors: 1.48×10^{-3} and 2.5×10^{-3}	64
5.5	Energy spread and bunch length with the updated impedance model and the parameters of 2.1, with two different momentum compaction factors: 1.48×10^{-3} and 2.5×10^{-3}	65
5.6	Transverse dynamics analysis considering the transverse RW with a higher momentum compaction and bunch length of 4.5 mm, non-colliding bunches. We compared the result obtained by using PyHT with the results obtained by using Delphi code.	66
5.7	Removing Delphi simulation results from Fig. 5.6: Transverse dynamics analysis considering the transverse RW with a higher momentum compaction and bunch length of 4.5 mm, non-colliding bunches.	67
5.8	Transverse dynamics analysis considering the transverse RW with a higher momentum compaction and bunch length of 15.2 mm, considering colliding bunches, so the beamstrahlung effect.	67
5.9	Blow-up of the horizontal beam size σ_x / σ_{x_0} as a function of the bunch population and of the horizontal tune scan for arc cell of $45^\circ / 45^\circ$	68
5.10	Bunch length, on the left, and energy spread, on the right, as a function of bunch population with and without the higher harmonic cavity system.	69
5.11	Transverse wakefield as a function of frequency.	70
5.12	Growth rate of the coupled bunch as function of the tune fractional part.	71
5.13	Transverse mode coupling instabilities analysis considering only the transverse wakefield and using resistive feedback after 10 turns damping time.	72
5.14	Turn by turn intra-bunch motion at a bunch population of 16×10^{10}	72
5.15	Turn by turn, intra-bunch motion at a bunch population of 18×10^{10}	73
5.16	TMCI analysis considering both the longitudinal and transverse wakefield using a resistive feedback with 10 turns damping time.	73
5.17	Turn by turn intra-bunch motion at intensity of 34×10^{10} considering both the longitudinal and transverse wakefield.	74
5.18	TMCI analysis considering both the longitudinal and transverse wakefield using a stronger resistive feedback, with 4 turns damping time.	74
5.19	Turn by turn intra-bunch motion at a bunch population of 46×10^{10} considering both the longitudinal and transverse wakefield.	75
5.20	Normalized horizontal beam size $\sigma_x \setminus \sigma_{x_0}$ as a function of horizontal tune for a bunch population of $N_p = 2.8 \times 10^{11}$ (on the top) and $N_p = 1.4 \times 10^{11}$ (on the bottom) at different chromaticities (Q'_x) with $\beta_x^* = 10\text{cm}$ [3].	76
5.21	Luminosity per IP at different chromaticities with $N_p = 2.8 \times 10^{11}$ and $N_p = 1.4 \times 10^{11}$ and with $\beta_x^* = 10\text{cm}$ [3].	77

List of Tables

1.1	Key parameters of FCC–ee (K. Oide, 2021), as evolved from the CDR parameters, with a shorter circumference of 91.2 km, and a new arc optics for Z and W running. Luminosity values are given per interaction point (IP), for scenarios with either 2 (left) or 4 IPs (right). Both the natural rms bunch lengths (b. lengths) and rms relative beam energy spreads (en. spreads) due to synchrotron radiation (SR) and their collision values including beamstrahlung (BS) are shown. The FCC-ee considers a combination of 400 MHz radiofrequency systems (at the first three energies, up to 2×2 GV) and 800 MHz (additional cavities for $t\bar{t}$ operation), with respective voltage strengths as indicated.[2].	8
1.2	Baseline Beam Parameters, used for our analysis, for the FCC–ee for different energies. Circumference is almost 91.17 km, SR and BS stand for synchrotron radiation and beamstrahlung.	11
2.1	Old FCC–ee key parameters.	32
2.2	Power loss contribution of the main FCC–ee components at nominal intensity and bunch length of $\sigma_z = 3.5\text{mm}$ and 12.1 mm (old configuration machine), in the lowest energy case of 45.6 GeV.	32
2.3	$\sigma_z = 12.1\text{mm}$, for the new configuration machine but with the old machine parameters, at nominal intensity and in the lowest energy case of 45.6 GeV.	37
2.4	Summary of the collimator settings for the Z mode and for the 4 IP layout. The table includes both betatron and off-momentum collimators. The synchrotron collimators and masks upstream the IP are not included in the table.	40
5.1	Harmonic cavity parameters	68

Nomenclature

CERN European Organization for Nuclear Research

CDR Conceptual Design Report

CDR Conceptual Design Report

CEPC Circular Electron Positron Collider

CLIC Compact Linear Collider

FCC–ee Future Circular Collider Electron Positron

FCC–hh Future Circular Collider Proton Proton

FS Feasibility Study

HL–LHC High-Luminosity Large Hadron Collider

ILC International Linear Collider

IP Interaction Point

ITSR Imaginary Tune Split and Repulsion

IW2D ImpedanceWake2D

LHC Large Hadron Collider

MW MicroWave instability

NEG Non-Evaporable Getter

PS Proton Synchroton

PSB Proton Synchrotron Booster

PyHT PyHEADTAIL

RW Resistive Wall

SPS Super Proton Synchrotron

TMCI Transverse Mode Coupling Instability

Introduction

In a particle collider, the luminosity is the figure of merit of its performance. It is proportional to the number of events per second generated in the collisions. When studying rare events as in the Large Hadron Collider (LHC) at CERN, one needs a very high luminosity, such that the more likely rare processes can occur and be observed. The upgrade of the LHC is the High-Luminosity LHC (HL-LHC) project, delivering proton-proton collisions at centre-of-mass energy of 14 TeV. It aims to increase the luminosity by a factor of 10 beyond the LHC design value. This updated machine will allow finding answers to the several open questions about the Standard Model theory. For the next 20 years, the HL-LHC is expected to run, but for the post-LHC era, CERN launched the Future Circular Collider (FCC) study for the design of different circular colliders. This study is investigating a high energy proton-proton machine (FCC–hh) to reach a center-of-mass energy of 100 TeV and a high luminosity electron-positron collider (FCC–ee) as a potential first step to cover a beam energy range from 45.6 GeV to 182.5 GeV.

The FCC–ee accelerator complex, the configuration and beam parameters of the lepton collider will be presented in detail in Chapter 1. Chapter 2 describes the theoretical framework needed to understand the core of this research activity, dedicated to the study of the main limitations of FCC–ee. At high beam intensity, necessary to reach the high luminosity foreseen for FCC–ee, collective effects due to the electromagnetic fields generated by the interaction of the beam with the vacuum chamber represent a serious issue by producing instabilities that can limit the machine operation and performance. The first part of this thesis is focused on the wake potential and the FCC–ee impedance model. The resistive wall impedance is representing the major source of wakefields in the machine due to its large circumference. Moreover, besides the resistive wall, other impedance sources have been analysed, in particular for their effects on the stability of the beam, such as bellows, BPMs, and collimators and the new FCC impedance repository is presented.

The impedance model thus obtained has been used to study single bunch instabilities, to predict their effects on beam dynamics, and to identify possible mitigation techniques. In fact, for FCC–ee at 45.6 GeV in Chapter 3 the longitudinal dynamics with the microwave instability analyses will be shown and in Chapter 4 the transverse dynamics study through the analysis of the TMCI instability threshold. In Chapter 5 further possible mitigations are also related to the beam-beam head-tail instability (X–Z instability) are proposed.

Chapter 1

CERN accelerator complex

The European Organization for Nuclear Research (CERN) was founded in 1954 by 12 European states. It had the purpose of rebuilding the European nuclear physics landscape that had been shattered by the Second World War and of sharing the increasing cost of research instruments among its members [8]. In November 2009, a new era of discovery in particle physics was opened at CERN with the inauguration of the Large Hadron Collider, LHC. The LHC is the world's largest particle accelerator, with a circumference of 27 km. It has been built in a tunnel 100 meters under the ground, and it can bring into collision proton beams at a center of mass energy of 14 TeV. The LHC is only the last element of a more complex chain of accelerators, as shown in Fig.1.1. In fact, to reach high energies a chain of accelerators was designed, and each machine gives a contribution for increasing the energy of the beam. First of all, the hydrogen atoms are ionized producing H–ions (consisting of a hydrogen atom with an additional electron) to be injected into Linac4. When the H–ions reach an energy of 160 MeV, they are fully stripped and transferred as protons to the Proton Synchrotron Booster (PSB), where these are accelerated to the energy of 2 GeV. After this, they pass through the Proton Synchrotron (PS) and the Super Proton Synchrotron (SPS) at energies of 25 GeV and 450 GeV respectively. At the end, the protons are ready for the LHC, where they are accelerated to a final energy of 7 TeV.

From the beginning, the LHC design foresaw the use of cutting-edge technologies: 8 T superconducting magnets to guide the beam along the 27 km ring. The two counter rotating beams are kept separate from one another, requiring twin-aperture magnets, and they are accelerated by superconducting radio frequency cavities. The cold bore magnets are maintained at ≈ 2 K with a flow of superfluid helium created by large cryogenic plants [8]. By using the LHC, on 4 July 2012 it was announced that a new particle with the centre-of-mass energy near 125 GeV [9, 10] has been observed, consistent with the Higgs boson predicted by the Standard Model. In October 2013, P. Higgs and F. Englert were awarded the Nobel Prize in Physics in recognition of their work on the Higgs mechanism. Although this discovery experimentally validated the standard model, the theory is still incomplete with several open questions. As the understanding of the standard model progressed further, the energy reached by the colliders became insufficient to explore rare phenomena. For that reason, the CERN launched the High Luminosity LHC (HL-LHC) project [11], an upgrade of LHC, aiming to increase the total number of collisions by a factor of 10 compared to the LHC baseline program. The HL-LHC project will be operational for the next 20 years and will help to address the many outstanding questions in fundamental physics. After the era of LHC,

The CERN accelerator complex

Complexe des accélérateurs du CERN

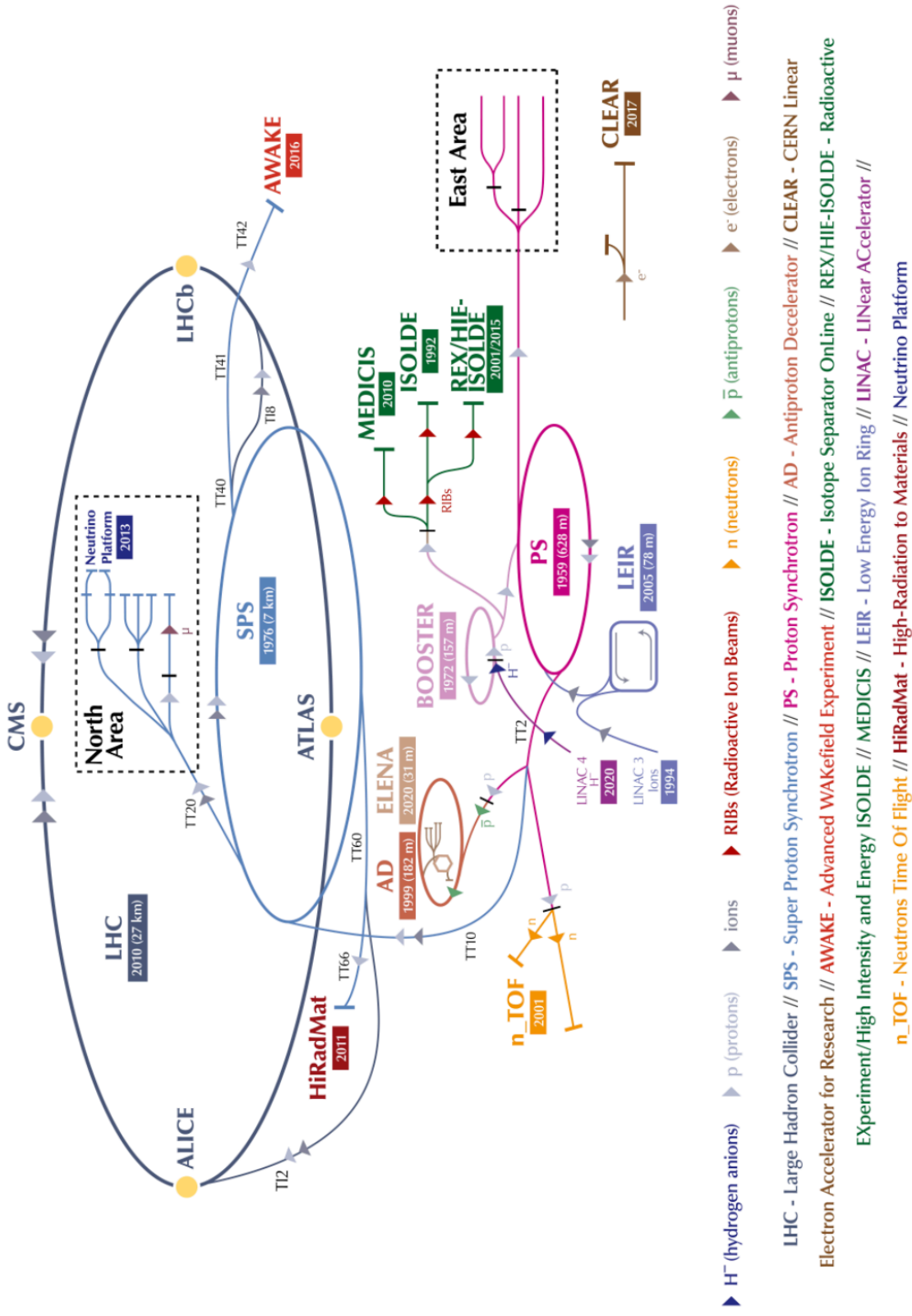


Figure 1.1: The new CERN accelerator complex. The circumference and first year of operation of each accelerator are indicated, as well as the particle species that can be accelerated.

CERN launched in 2014 the Future Circular Collider (FCC) Study [11] aiming to design different particle accelerators to ensure worldwide particle physics. Nowadays, more than 120 institutes are part of this international collaboration, whose ultimate goal is a hadron collider (FCC–hh) with a centre-of-mass energy of 100 TeV, an order of magnitude above the LHC [1]. Increasing the energy of collisions and the luminosity with future accelerators currently opens the opportunity to explore the secrets of the structure of matter. In fact, for example, the FCC study would enable us to investigate with high precision the properties of the Higgs boson.

The Higgs particle is unique and raises profound questions about the fundamental laws of nature. On the other hand, the study of Higgs properties is in itself a powerful experimental tool to look for answers, and this could be possible with what is called the Higgs factory, an electron-positron (e^-e^+) collider. Furthermore, by using a collider with significantly higher energies than Higgs factory, we could understand the fabric of the universe analyzing the Higgs boson pair-production study.

As stated in the key points of the 2020 Update of the European Strategy for Particle Physics [12]: *"An electron-positron Higgs factory is the highest-priority next collider. In the longer term, the European particle physics community has the ambition to operate a proton-proton collider at the highest achievable energy. Accomplishing these compelling goals will require innovation and cutting-edge technology: the particle physics community should ramp up its R&D effort focused on advanced accelerator technologies, in particular that for high-field superconducting magnets, including high-temperature superconductors; Europe, together with its international partners, should investigate the technical and financial feasibility of a future hadron collider at CERN with a centre- of-mass energy of at least 100 TeV and with an electron-positron Higgs and electroweak factory as a possible first stage. Such a feasibility study of the colliders and related infrastructure should be established as a global endeavour and completed on the timescale of the next strategy update. The timely realization of the electron-positron International Linear Collider (ILC) in Japan would be compatible with this strategy, and in that case the European particle physics community would wish to collaborate."*

Different e^+e^- linear circular Higgs factories are currently under design study [13]. The Future Circular Collider examines scenarios for two different types of particle collisions: hadron (proton–proton and heavy ion) collisions, FCC–hh [14], electron–positron collisions, FCC–ee [15]. Other options include proton-electron collisions or proton-heavy-ion collisions. The FCC–ee would be the first step, and this machine will envisage a 80-100 km tunnel in the Geneva area, as shown in Fig.1.2 [16].

1.1 The Future Circular Collider

1.1.1 Introduction

In the previous section, we introduced the FCC, Future Circular Collider, and now we will analyze it more in detail. The purpose of the FCC is to move the energy and intensity frontiers of particle colliders to reach collision energies of 100 TeV in search of new physics. FCC–ee is considered as a potential first step towards the 100 TeV hadron collider FCC–hh in the same almost 100 km tunnel. In fact, the lepton and hadron colliders would share the technical infrastructures. Moreover, the FCC could reuse CERN’s existing infrastructure. For example, one possibility could be that the existing chain of hadron accelerators, from Linac4 to PSB, PS and SPS to LHC, can serve as an injector complex for the FCC–hh [2]. The lepton collider is aimed at covering a beam energy

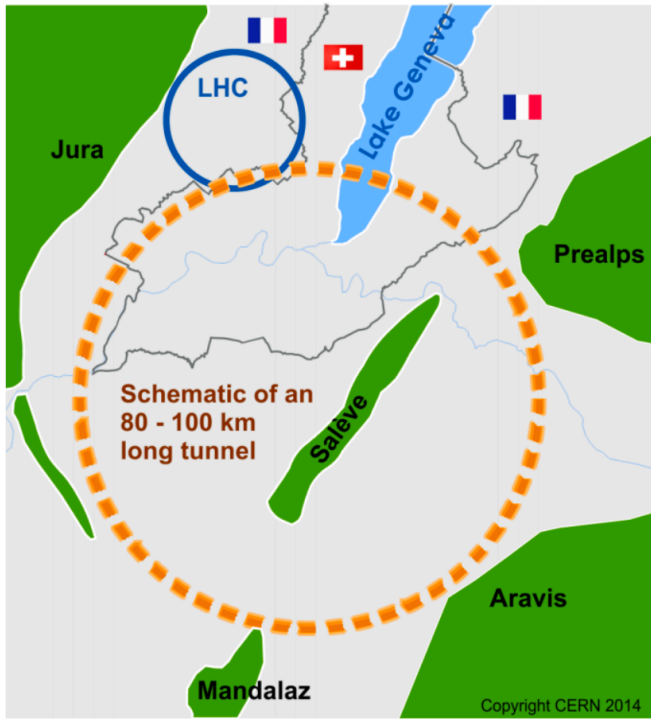


Figure 1.2: Schematic view of the FCC tunnel in the Geneva area.

range from 45.6 GeV to 182.5 GeV, thus allowing us to study the properties of the Higgs, W and Z bosons and top quark pair production thresholds with unprecedented precision. Currently, there are other e^+e^- collider projects, such as ILC [17, 18], CLIC [19, 20], and CEPC [21]. Out of all these machines, FCC-ee is expected to deliver the highest luminosity at each centre-of-mass energy as shown in Fig.1.3, allowing very precise measurements of all known heavy particles.

The successful past of the Large Electron Positron Collider (LEP) and, of course, of the Large Hadron Collider (LHC) projects have inspired the FCC "integrated program". In 2021 CERN has launched the FCC Feasibility Study (FS), which is based not only on the technical aspects of the accelerators but also on the feasibility of tunnel construction and technical infrastructure, and the possible financing of the proposed future facility. The FCC FS is organized as an international collaboration with, currently, about 150 participating institutes from around the world[2]. In Fig. 1.4 the technical schedule of the FCC is shown. The project foresees the start of FCC tunnel construction around 2030, the first lepton collisions at FCC-ee in the early 2040s, and the first FCC-hh hadron collisions by 2065-70 [2]. For the cases of physics description, the design of the lepton and hadron colliders, and the underpinning technologies and infrastructures [15, 22, 23], the Conceptual Design Report (CDR) for the FCC was published in 2019.

As already mentioned, the FCC-ee integrated project is an electron positron collider e^+e^- , which would serve as a Higgs factory, an electroweak and top factory at the highest luminosities, and will run at four different center-of-mass energies. In fact, the FCC-ee is designed to collide beams at four different energies, namely at the Z pole, at the WW threshold, at the ZH production peak and at the $t\bar{t}$ threshold. In this thesis, we will concentrate on the FCC-ee at the Z pole.

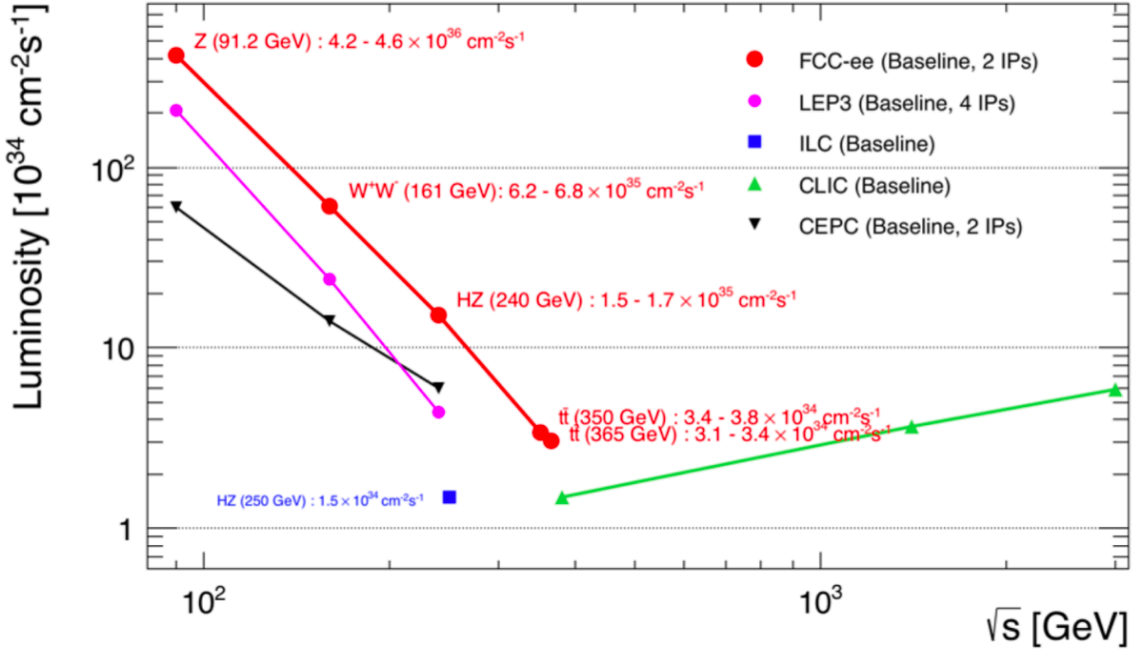


Figure 1.3: Expected baseline luminosities of the current worldwide lepton colliders as a function of the center-of-mass energy. The variable s on the x-axis is the Mandelstam variable and \sqrt{s} represents the total center-of-mass energy during collision[1].

1.1.2 Machine layout and beam parameters

The FCC is an ongoing project and for that reason the layout and parameters are still in progress. In fact, the 2019 FCC CDR describes the baseline FCC design with a circumference of 97.75 km, 12 surface sites, and two primary collision points. Instead, in 2021, further design optimization has resulted in an optimized placement of much lower risk, with a circumference of about 91.2 km and only 8 surface sites, and which would be compatible with 2 or 4 collision points [2]. In Table 1.1 the preliminary key FCC-ee parameters for the cases of two or four IPs, respectively, are shown.

Certainly, the beam parameters such as the emittances, bunch length, lifetime, and luminosity must still need to be validated with more realistic evaluations (for example by considering strong-strong beam-beam simulations, errors, and optical corrections). The table shows how the luminosity values for two IPs are a bit higher than for four IPs.

As a result of adaptations of the CDR design and re-optimization of the machine parameters, Fig.1.5 drafts the layout and possible straight-section functions for the electron-positron collider.

For the two counter-rotating electron and positron beams, there are two separate beam pipes. They are important for two main aspects: at low energy they allow avoiding parasitic collisions and therefore an operation with a large number of bunches, while at the highest energy the double ring allows the tapering of the magnets to compensate for effect of synchrotron radiation (SR) loss along the ring. [24]. In addition, we have to consider beamstrahlung (BS) which is one of the main luminosity limitations in the machine. As illustrated in the next chapters, the effect of BS of increasing the equilibrium energy spread and bunch length will help to overcome single bunch instabilities at low energy. Primarily, the initial *FCC - ee* injection scheme was based on CLIC concepts [25], to maintain the stored beam current and the highest luminosity; however, it has been

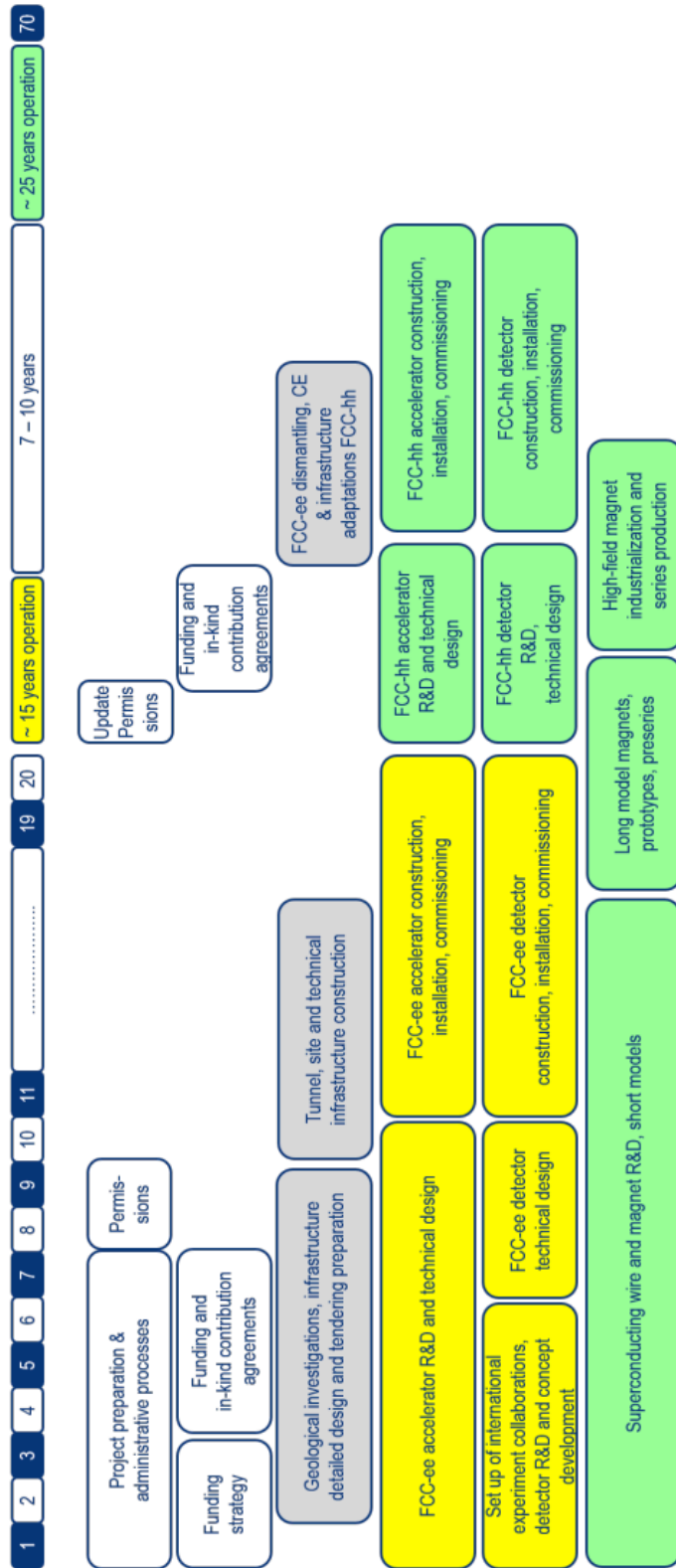


Figure 1.4: Technical schedule of the FCC integrated project with year 1 equal to 2021 [2]

Table 1.1: Key parameters of FCC–ee (K. Oide, 2021), as evolved from the CDR parameters, with a shorter circumference of 91.2 km, and a new arc optics for Z and W running. Luminosity values are given per interaction point (IP), for scenarios with either 2 (left) or 4 IPs (right). Both the natural rms bunch lengths (b. lengths) and rms relative beam energy spreads (en. spreads) due to synchrotron radiation (SR) and their collision values including beamstrahlung (BS) are shown. The FCC–ee considers a combination of 400 MHz radiofrequency systems (at the first three energies, up to 2×2 GV) and 800 MHz (additional cavities for $t\bar{t}$ operation), with respective voltage strengths as indicated.[2].

Running mode	Z	W	ZH	$t\bar{t}$	Z	W	ZH	$t\bar{t}$
Number of IPs			2				4	
Beam energy (GeV)	45.6	80	120	182.5	45.6	80	120	182.5
Bunches/beam	12000	880	272	40	10000	880	248	36
Bunch population (10^{11})	2.02	2.91	1.86	2.37	2.43	2.91	2.04	2.64
Beam current [mA]	1280	135	26.7	5.0	1280	135	26.7	5.0
Lum. / IP [10^{34} cm $^{-2}$ s $^{-1}$]	193	22.0	7.73	1.31	182	19.4	7.26	1.33
Energy loss / turn [GeV]	0.039	0.37	1.87	10.0	0.039	0.37	1.87	10.0
Synchr. Rad. Power [MW]			100				100	
RF Volt. 400MHz[GV]	0.12	1.0	2.08	4.0	0.12	1.0	2.08	4.0
RF Volt. 800MHz[GV]	0	0	0	7.25	0	0	0	7.25
Rms b. length (SR) [mm]	4.38	3.55	3.34	2.02	4.38	3.55	3.34	2.02
(+BS)[mm]	12.1	7.06	5.12	2.56	14.5	8.01	6.00	2.95
Rms en. spread (SR) [%]	0.039	0.069	0.103	0.157	0.039	0.069	0.103	0.157
(+BS)[%]	0.108	0.137	0.158	0.198	0.130	0.154	0.185	0.229
Rms hor. emit. ε_x [nm]	0.71	2.17	0.64	1.49	0.71	2.17	0.64	1.49
Rms vert. emit. ε_y [pm]	1.42	4.32	1.29	2.98	1.42	4.32	1.29	2.98
Norm. hor. em. $\gamma\varepsilon_x$ [μm]	63	340	150	530	63	340	150	530
Norm. vert. em. $\gamma\varepsilon_y$ [μm]	0.13	0.68	0.30	1.06	0.13	0.68	0.30	1.06
Longit. damp. time [turns]	1170	216	64.5	18.5	1170	216	64.5	18.5
Hor. IP beta β_x^* [mm]	100	200	300	1000	100	200	300	1000
Vert. IP beta β_y^* [mm]	0.8	1.0	1.0	1.6	0.8	1.0	1.0	1.6
Beam lifetime [min].	35	32	9	16	19	18	6	9

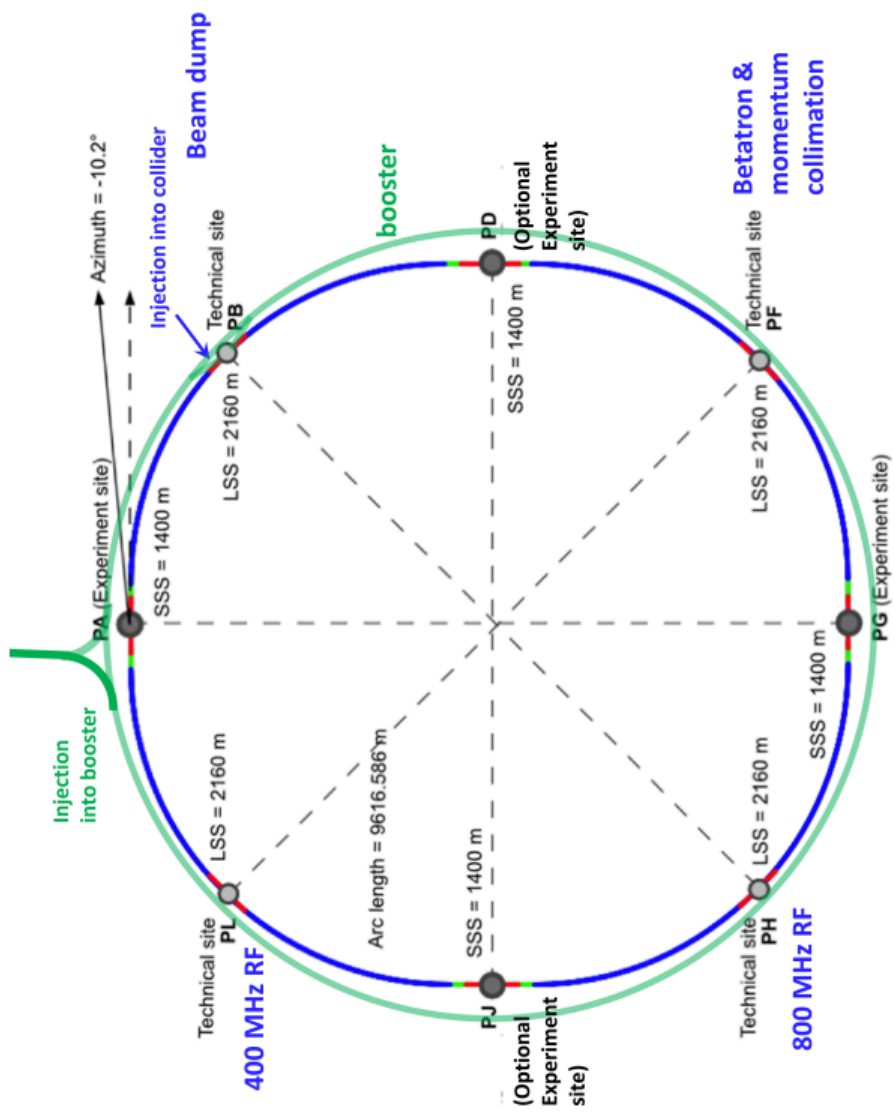


Figure 1.5: Schematic FCC–ee layout and its booster with a circumference of 91.2 km and four IP

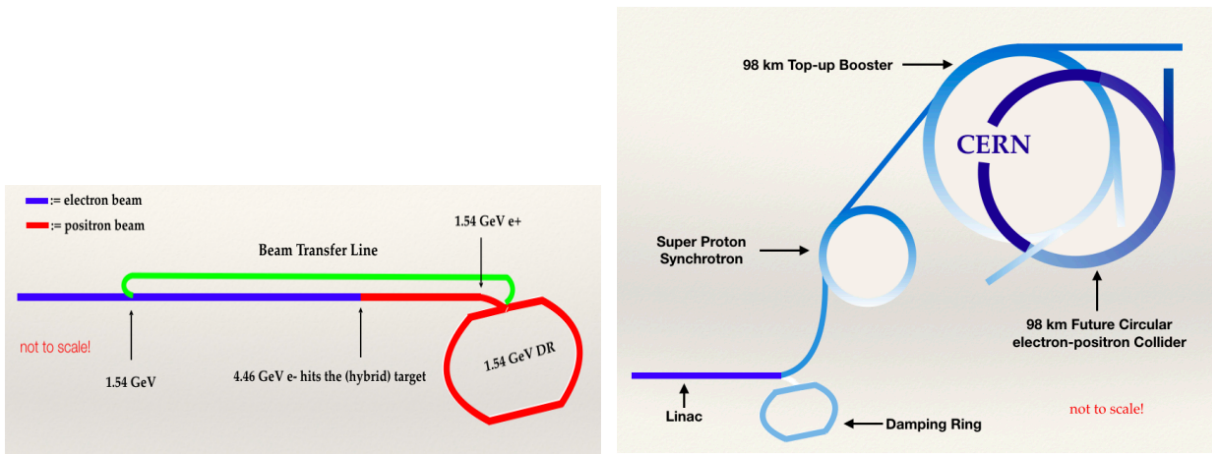


Figure 1.6: On the left, schematic layout of the pre-injector chain and, on the right, the injector complex.

preferred for the final design a SuperKEKB approach using short bunches with high current. In fact, the SuperKEKB collider presents many features of the key elements of FCC-ee, such as a double ring, a large crossing angle, a low vertical IP beta function β_y^* and a short design beam lifetime of a few minutes [2]. An important fact to highlight is that the SuperKEKB has achieved, in both rings, the smallest β_y^* of 0.8mm and in June 2021 it reached a word record luminosity of $3.81 \times 10^{34} \text{ cm}^{-2} \text{ s}^{-1}$ [2].

The injector baseline description can be found in [26] while in Fig.1.6 we show the injection complex layout. The FCC-ee injection system is composed of a 320 m long e^+e^- linac able to accelerate a bunch up to 6 GeV with a rate of 100–200 Hz. In the same linac, at 4.46 GeV, we have positron production. Then, a 242 m circumference damping ring at 1.54 GeV is needed for both the positron and electron beams [27]. Following the damping ring, there is the Super Proton Synchrotron (SPS) to accelerate positron and electron beams up to 20 GeV [28]. The beams are finally accelerated from 20 GeV to the FCC-ee collision energies in the top-up booster ring [29].

1.1.3 FCC project: State-of-the-art

Since the FCC is a project under development, all design parameters have changed in recent years. In Table 1.2 the latest baseline beam parameters that we use as reference are shown.

In general, the beam dynamics presented in this thesis will focus on the Z resonance at 45.6 GeV, because it represents the most challenging scenario from the beam stability point of view. In fact, it presents high beam current, high number of bunches per beam, the lowest emittance, and the longest longitudinal damping time: all these combinations make this machine configuration more critical with respect to the others. Another important point that I would like to highlight is the effect of the beamstrahlung. In the table, we observe that we have two different values of energy spread and bunch length, depending whether we take into account only the synchrotron radiation or also the beamstrahlung. This is very important for the collective effects because the beam behavior is very different.

Table 1.2: Baseline Beam Parameters, used for our analysis, for the FCC–ee for different energies. Circumference is almost 91.17 km, SR and BS stand for synchrotron radiation and beamstrahlung.

Layout	PA31-1.0			
	Z	WW	ZH	$t\bar{t}$
Circumference (km)	91.174117 km			
Beam energy (GeV)	45.6	80	120	182.5
Bunch population (10^{11})	2.53	2.91	2.04	2.64
Bunches per beam	9600	880	248	36
RF frequency (MHz)		400		400/800
RF Voltage (GV)	0.12	1.0	2.08	4.0/7.25
Energy loss per turn (GeV)	0.0391	.37	1.869	10.0
Longitudinal damping time (turns)	1167	217	64.5	18.5
Momentum compaction factor 10^{-6}	28.5		7.33	
Horizontal tune/IP	55.563		100.565	
Vertical tune/IP	55.600		98.595	
Synchrotron tune	0.0370	0.0801	0.0328	0.0826
Horizontal emittance (nm)	0.71	2.17	0.64	1.49
Vertical emittance (pm)	1.42	4.34	1.29	2.98
IP number	4			
Nominal bunch length (mm)(SR/BS)*	4.37/14.5	3.55/8.01	3.34/6.0	2.02/2.95
Nominal energy spread (%) (SR/BS)*	0.039/0.130	0.069/0.154	0.103/0.185	0.157/0.229
Piwinski angle (SR/BS)*	6.35/21.1	2.56/5.78	3.62/6.50	0.79/1.15
ξ_x/ξ_y	0.004/0.152	0.011/0.125	0.014/0.131	0.096/0.151
Horizontal β^* (m)	0.15	0.2	0.3	1.0
Vertical β^* (mm)	0.8	1.0	1.0	1.6
Luminosity /IP ($10^{34}/\text{cm}^2 \text{ s}$)	181	17.4	7.8	1.25

Chapter 2

Collective effects

In this second chapter, we will enter more in details for explaining the concept of collective effect: wakefield and impedance. We will discover how to calculate the loss factor and the method and codes we used to estimate the wake potentials of the machine devices studied until now. The model used, and the devices, will be analysed and the updated configuration will be presented. Moreover, at the end of this chapter the new impedance repository created for the FCC–ee project will be introduced.

2.1 Introduction

External electromagnetic fields, provided by bending and focusing magnets (dipoles and quadrupoles, respectively) and RF cavities, produce the Lorentz force, which interacts with a beam of charged particles when it propagates in an accelerator. However, the beam particles can interact with the surrounding environment and with themselves, producing additional electromagnetic fields that can act back on the beam and perturb its motion. In the equations of motion of the beam, these additional fields have to be included. Considering the total electromagnetic fields in the Lorentz force given by the sum of the external and perturbation fields, we can write:

$$\vec{F} = q \left[\left(\vec{E}_{\text{ext}} + \vec{E}_{\text{wake}} \right) + \vec{v} \times \left(\vec{B}_{\text{ext}} + \vec{B}_{\text{wake}} \right) \right] \quad (2.1)$$

Collective effects refer to the category of phenomena in which the evolution of the beam depends on the combination of external fields and interaction between beam particles. Different categories of collective effects can be defined depending on the type of interaction:

- space charge effects due to the interaction of beam particles with themselves and with perfectly conducting vacuum chamber
- beam-beam effects due to interaction of the beam with the counter-rotating beam in a collider
- wakefield (in time domain) or impedance (in frequency domain) effects generated by the interaction of the beam with the vacuum chamber and accelerator devices.
- electron cloud effects due to the interaction between beam and electrons produced in the accelerator.

All of these perturbations can cause instability in both the longitudinal and transverse directions. This represents one of the main limitations in machine operation and its performance. Studying these instabilities and their underlying mechanisms is critical during the design stage of any accelerator, as it enables the identification of possible mitigation methods and the control of beam stability during operation. The research activity presented in this thesis focuses on the study of the third type of collective effects. A short summary of the theory of wakefields and impedances in particle accelerators is described in the next section.

2.1.1 Wakefields and Impedances

We know that the beam is not composed of a single particle but of several billions of them travelling in an environment that is not perfectly conducting; thus, the image currents induced on the beam pipe boundaries will generate parasitic electromagnetic fields. These fields will, in turn, perturb the other particles present in the bunch itself or the following bunches, if present. The more the particles the bunch contains, the stronger these fields get, and thus the stronger are the perturbations. These perturbations must be included in the equations of motion to study their impact on the beam dynamics. Detailed explanations of the concept of wakefields and derivations for different structures can be found in [30–33].

In order to introduce wakefields and beam coupling impedances, consider the reference system in Fig.2.1, where a source particle $q_1(z_1, r_1)$ and a test particle $q_2(z_2, r_2)$ travel with constant velocity $v \simeq c$, where c is the speed of light. The two particles are ultrarelativistic; therefore, causality imposes that the test particle cannot affect the source. If the two particles move inside a perfectly conducting and smooth chamber, the test particle does not feel any force. However, if the chamber has some geometry variation or the pipe walls have finite conductivity, the electromagnetic fields generated behind the source (denoted as wakefields) can interfere with the test particle and disrupt its motion. In the entire accelerator, we have different types of fields: to force the circulating beam to follow a closed orbit there is an external magnetic field induced in the dipoles; the field induced by alternating focusing and defocusing quadrupoles controls the amplitude of the transverse betatron oscillation of the beam; the electric field in the RF cavities allows acceleration and RF manipulations; the beam quality can be controlled by several higher-order magnetic and electric fields. In addition, to these external electromagnetic fields, the beam itself produces self-induced fields. Related to these last fields, the Lorentz force generated by the source particle q_1 and acting on the test particle q_2 can be written as: the Lorentz force generated by the source particle q_1 and acting on the test particle q_2 can be written as:

$$\mathbf{F} = q_2 [E_z \hat{z} + (E_x - cB_y) \hat{x} + (E_y + cB_x) \hat{y}] = \mathbf{F}_{\parallel} + \mathbf{F}_{\perp} \quad (2.2)$$

where \mathbf{E} and \mathbf{B} are the electric and magnetic fields generated by q_1 inside the structure. This force is given by the sum of two components, which have different effects on the test charge. In fact, we have a longitudinal force that changes its energy and a transverse force that deflects its trajectory.

If we consider a device of length L and assume that z is the distance between the two particles that does not change during the passage through the structure (rigid beam approximation), the energy variation is defined as the integrated longitudinal force acting on the test particle along the

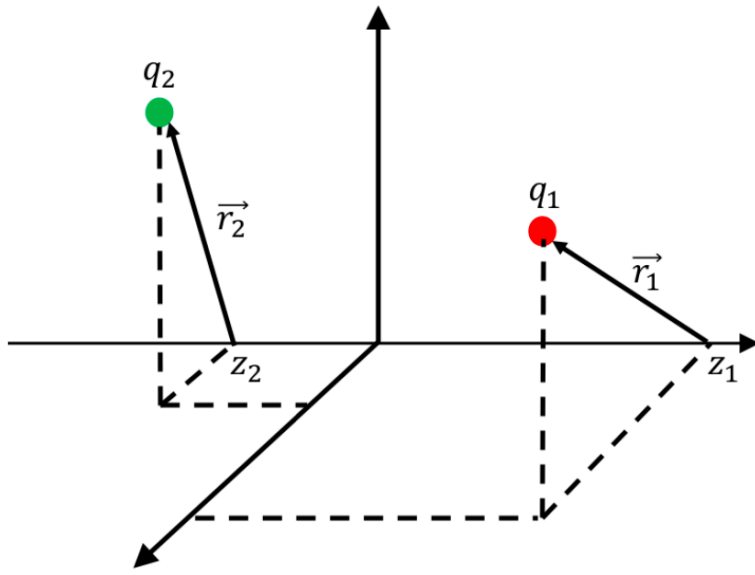


Figure 2.1: Reference system with a source particle q_1 (in red) and a test particle q_2 (in green)[1].

length L of the object:

$$U(r_2, r_1, z) = \int_0^L F_{\parallel} ds \simeq U(z) \quad (2.3)$$

in which r_2, r_1 are the transverse positions of the test and source charges, respectively. The longitudinal wake function is defined as the energy change normalized by the two charges.

$$w_{\parallel}(z) = -\frac{U(z)}{q_1 q_2} \quad (2.4)$$

From this equation, we can make several observations. First, the longitudinal wake function obtained by Eq.2.4 does not depend on the transverse positions r_1, r_2 . On the other hand, most of the structures in the beam pipe have a symmetric shape. In the particular case of cylindrical symmetry and ultrarelativistic charges, the wake function can be expanded in multipolar terms. In the longitudinal case, the first term of the monopole is dominant, and the wake function depends only on z [32]. Moreover, the minus sign in Eq. 2.4 means that, for a positive wake, the test particle is losing energy.

In the transverse plane and with asymmetrical shape, the deflecting kicks are distinguished in a dipolar kick defined as the integrated transverse force from an offset source acting on an on-axis test particle along the length L of the object:

$$\mathbf{M}^{\text{dip}}(\mathbf{r}_2, \mathbf{r}_1, z) = \int_0^L \mathbf{F}_{\perp} \Big|_{\mathbf{r}_2=0} ds \simeq r_1 \mathbf{M}^{\text{dip}}(z) \quad (2.5)$$

and a quadrupolar kick defined as the integrated transverse force from an on-axis source acting on an offset test particle along the length L of the object:

$$\mathbf{M}^{\text{quad}}(\mathbf{r}_2, \mathbf{r}_1, z) = \int_0^L \mathbf{F}_{\perp} \Big|_{\mathbf{r}_1=0} ds \simeq r_2 \mathbf{M}^{\text{quad}}(z) \quad (2.6)$$

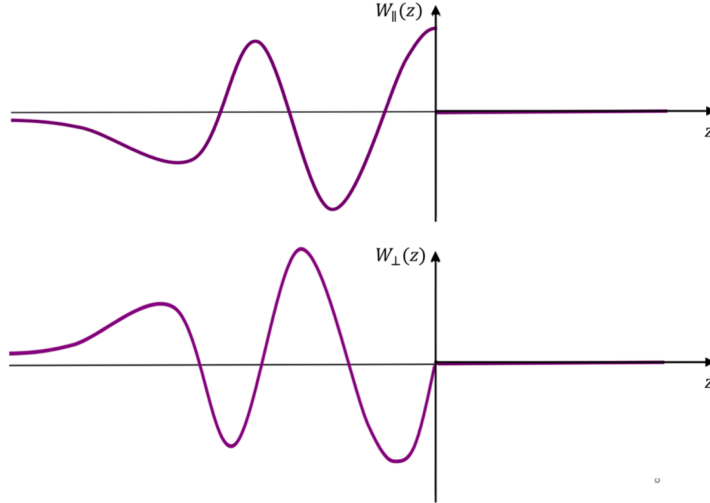


Figure 2.2: Example of longitudinal (top) and transverse (bottom) wake functions for ultra-relativistic particles ($\beta = 1$)[1].

In this thesis, we are using the dipolar and quadrupolar terms considering the detuning impedances. With the definition of the transverse deflecting kicks, we can introduce the transverse dipolar and quadrupolar wake functions. They are given by the corresponding transverse kick normalized by the two charges and by the offset of the source and test particle, respectively:

$$w_{\perp}^{\text{dip}}(z) = \frac{\mathbf{M}^{\text{dip}}(z)}{q_1 q_2} \quad (2.7)$$

$$w_{\perp}^{\text{quad}}(z) = \frac{\mathbf{M}^{\text{quad}}(z)}{q_1 q_2} \quad (2.8)$$

A positive transverse wake corresponds to a defocusing transverse force. The Fourier transforms of the wake functions in the frequency domain define the longitudinal and transverse (dipolar and quadrupolar) beam coupling impedances.

$$Z_{\parallel}(\omega) = \frac{1}{c} \int_{-\infty}^{+\infty} w_{\parallel}(z) e^{j \frac{\omega z}{c}} dz \quad (2.9)$$

$$Z_{\perp}^{\text{dip}}(\omega) = -\frac{j}{c} \int_{-\infty}^{+\infty} w_{\perp}^{\text{dip}}(z) e^{j \frac{\omega z}{c}} dz \quad (2.10)$$

$$Z_{\perp}^{\text{quad}}(\omega) = -\frac{j}{c} \int_{-\infty}^{+\infty} w_{\perp}^{\text{quad}}(z) e^{j \frac{\omega z}{c}} dz \quad (2.11)$$

2.1.2 Wake potentials and loss factors

Another useful definition that should be introduced is the loss factor, representing the normalized energy lost by the source particle in the creation of the wake:

$$k = -\frac{U(z=0)}{q_1^2} = w_{\parallel}(z=0) \quad (2.12)$$

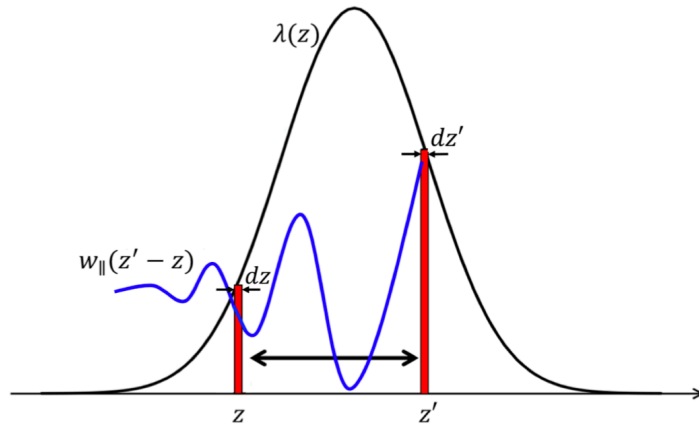


Figure 2.3: Integral transformation to compute the energy loss of a slice due to the entire bunch [1].

The Eq. 2.12 is valid only for non-ultrarelativistic particles. For charges travelling at the speed of light, causality requires that the longitudinal wakefield is discontinuous at $z = 0$, as shown in Fig. 2.2 on the top plot. At the speed of light, the lost factor is given by the beam loading theorem [34]:

$$k = \frac{w_{||}(z \rightarrow 0^-)}{2} \quad (2.13)$$

This theorem affirms that an ultrarelativistic particle can only see half of its own wake and the wake exists only in the region $z < 0$, as shown in Fig. 2.2. On the other hand, in the transverse case, the wake vanishes for $z > 0$ because of the ultrarelativistic approximation. For $z = 0$ it is equal to zero because the source and test particles have the same longitudinal position and move in parallel and can only interact through the space charge. This concept is valid for the resistive wall and geometrical impedances, however, wakes due to CSR can propagate forward even for ultrarelativistic case.

Examples of wakefields and impedances such as resistive wall impedance, collimators, RF cavities, tapers, beam position monitors and bellows will be given in the next sections of this chapter.

The wake functions generated by point charges and defined by Eqs. 2.4 - 2.7 and 2.8 represent the Green functions that describe the response of the structure to an impulsive source. These quantities can be used to calculate the longitudinal and transverse wakefields produced by any bunch distribution. Consider the longitudinal plane, and a bunch with longitudinal distribution $\lambda(z)$. As shown in Fig. 2.3, the energy $dU(z)$ lost or gained by a test slice $e\lambda(z)dz$ at position z in the bunch can be obtained as the integral of the contributions of the wakefields generated by all previous slices $e\lambda(z')dz'$ at the position z' . The energy loss of a bunch is then obtained by integrating $dU(z)$ over the full bunch extension:

$$U = \int_{-\infty}^{+\infty} dU(z)dz = -e^2 \int_{-\infty}^{+\infty} \lambda(z)dz \int_z^{+\infty} \lambda(z') w_{||}(z' - z) dz' \quad (2.14)$$

or if we want to write it in terms of Fourier transforms [31]:

$$U = -\frac{e^2}{2\pi} \int_{-\infty}^{\infty} |\Lambda(\omega)|^2 \operatorname{Re} [Z_{||}(\omega)] d\omega \quad (2.15)$$

where $\Lambda(\omega)$ is the bunch spectrum and $\text{Re}[Z_{\parallel}(\omega)]$ is the real part of the longitudinal beam coupling impedance. The longitudinal wake potential of the distribution is defined as the convolution between the longitudinal wake function $w_{\parallel}(z)$ and the bunch distribution $\lambda(z)$:

$$W_{\parallel}(z) = \int_{-\infty}^z w_{\parallel}(z' - z) \lambda(z') dz' \quad (2.16)$$

Integrating the product of the wake potential and the bunch distribution, we can obtain the longitudinal loss factor:

$$k_{\parallel} = \int_{-\infty}^{+\infty} W_{\parallel}(z) \lambda(z) dz \quad (2.17)$$

The energy loss of a bunch can be written in terms of loss factor using Eq 2.16 and 2.17 as:

$$U = -e^2 k_{\parallel} \quad (2.18)$$

The Eq. 2.14 and 2.15 are valid for a bunch passing through the impedance once. If we consider also the wakes generated during the previous turns, these equations can be generalized, respectively, as [31]:

$$U = -e^2 \int_{-\infty}^{+\infty} \lambda(z) dz \int_{-\infty}^{+\infty} \lambda(z') \sum_{k=-\infty}^{+\infty} w_{\parallel}(kC + z' - z) dz' \quad (2.19)$$

or, in frequency domain:

$$U = -\frac{e^2 \omega_0}{2\pi} \sum_{p=-\infty}^{\infty} |\Lambda(p\omega_0)|^2 \text{Re}[Z_{\parallel}(p\omega_0)] \quad (2.20)$$

where C is the circumference of the accelerator, k is the sum of turns, and $\omega_0 = \frac{2\pi c}{C}$ is the revolution frequency.

The total energy lost, in a turn, by a bunch of particles has to be compensated by the RF system. If we consider linear oscillations around the synchronous phase ϕ_s , we can write the relation:

$$U = -\Delta\phi e V_{RF} \cos(\phi_s) \quad (2.21)$$

where $\Delta\phi$ is the phase shift depending on the bunch intensity, and V_{RF} is the RF voltage. From the Eq. 2.18 and 2.21 we can obtain the following formula for the longitudinal loss factor:

$$k_{\parallel} = \frac{\Delta\phi V_{RF} \cos(\phi_s)}{e N_p} \quad (2.22)$$

The total energy loss by the beam, for a uniformly filled machine, with N_b equally spaced bunches covering the full ring circumference with bunch spacing $\tau_b = \frac{2\pi}{h\omega_0}$ where $h = N_b$ is the harmonic number, is given by:

$$U = -\frac{e^2 N_b^2 N_p^2 \omega_0}{2\pi} \sum_{p=-\infty}^{\infty} |\Lambda(pN_b\omega_0)|^2 \text{Re}[Z_{\parallel}(pN_b\omega_0)] \quad (2.23)$$

where Np is the single bunch population. The total power loss is:

$$P_{\text{loss}} = \frac{U}{T_0} = I^2 \sum_{p=-\infty}^{+\infty} |\Lambda(pN_b\omega_0)|^2 \text{Re} [Z_{\parallel}(pN_b\omega_0)] \quad (2.24)$$

where $I = \frac{N_b N_p e}{T_0}$ is the average beam current with T_0 the machine revolution period. The fraction of energy lost in the pipe walls or other devices installed in the machine can be very dangerous because it causes additional heating of the equipment and eventual damage. Therefore, evaluating the energy loss of a beam is very important. Also in the transverse plane, we can apply similar definitions. For example, the transverse wake potential is defined as:

$$W_{\perp}(z) = \int_{-\infty}^z w_{\perp}(z' - z) \lambda(z') dz' \quad (2.25)$$

and consequentially, the transverse loss factor, also called the kick factor, which represents the deflection or kick exerted by the transverse wake fields on the beam, is:

$$k_{\perp} = \int_{-\infty}^{+\infty} W_{\perp}(z) \lambda(z) dz \quad (2.26)$$

2.2 Pipe Model

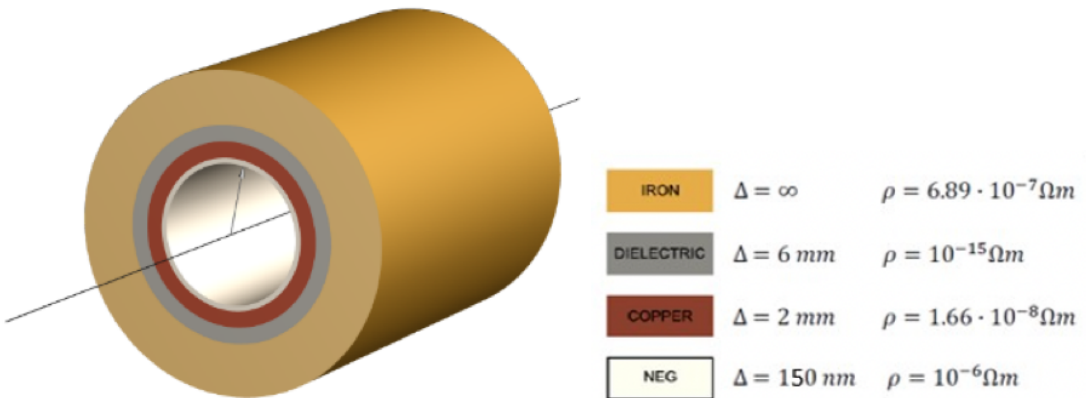


Figure 2.4: On the left, the vacuum chamber model and on the right, the four simulated layers.

The beam pipe model used for the evaluation of the coupling impedance and the wakefield is assumed to be circular with a radius of 35 mm, as shown in Fig.2.4. The walls are supposed to be made of four layers: a first thin layer of Non-Evaporable Getter (NEG) coating 150 nm thick, used to reduce the secondary electron yield for electron cloud mitigation and, in some cases, to help the pumping process, a copper substrate with a thickness of 2 mm, followed by a 6 mm dielectric (air) and, finally, the magnet chamber modelled as an outer layer of iron with resistivity $\rho = 10^{-7} \Omega m$ (stainless steel) and infinite thickness [1]. After some studies at CERN [1], in particular, for collective effects, we decide to use for our simulations a NEG film thickness of 150 nm, as a result of a compromise between having a minimum thickness and satisfying the vacuum and electron cloud requirements. The presence of the coating affects the RW impedance, making its contribution more critical; in the next section, we analyse different models using different values of NEG film thickness.

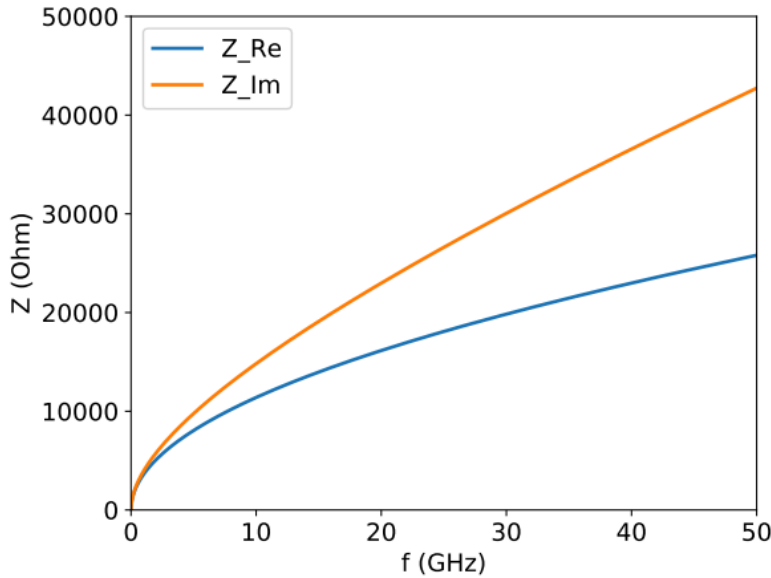


Figure 2.5: Real and imaginary part of the longitudinal resistive wall impedance, calculated by IW2D

2.3 Simulation codes:

For the evaluation of the impedances and wake potential, we used in particular two fundamental codes, ImpedanceWake2D and PyHEADTAIL, which will be analyzed in the next sections.

2.3.1 ImpedanceWake2D

ImpedanceWake2D is a package containing four different codes that compute the longitudinal and transverse beam coupling impedances and wake functions in a multilayer axisymmetric or flat structure that is longitudinally invariant [35]. Since, as we saw in the previous chapter, we have a beam pipe made of multiple system with 4 different layers, IW2D is perfect for our analysis. In Ref. [36] the theory of coupling impedance and wakefields in cylindrical structures has been described.

The real and imaginary parts of the longitudinal impedance due to the resistive wall (RW) for FCC–ee are shown in Fig. 2.5. The excess of the imaginary part compared to the real part is mainly due to the thin coating layer, as demonstrated in [37]. We could reduce this difference by decreasing the coating thickness because it is proportional to this quantity. As a result, in order to reduce the RW contribution, the NEG layer should be as thin as possible, but, at the same time, we need the coating for mitigating the electron cloud build-up, in particular for the positron machine, and for pumping reasons. Fig. 2.6 shows the real and imaginary parts of longitudinal and transverse impedance, left and right hand side, respectively, and in these plots we analyze in particular two cases, 150 nm and 100 nm of NEG thickness. As can be seen from the figure, by increasing the thickness only the imaginary part of the impedance is affected. Since the real part does not change, also, the loss factor remains the same for the two cases. The comparison between 200 and 100 nm of NeG thickness is shown in Fig. 2.7. For FCC–ee at low energy, the contribution of the RW impedance can be reduced by decreasing the thickness of the coating. Following these results, we decided to consider for the new configuration machine a NEG film thickness of 150 nm. Indeed, if we evaluate the bunch length and energy spread as a function of intensity (more details of the

simulations will be discussed in the next section), as shown in Fig. 2.8, we can see that at a given threshold, around 20×10^{10} particles, the energy spread starts to grow. This is called the microwave instability threshold, and above it the bunch oscillates, manifesting a turbulent motion. This regime should be avoided during the operation of the machine. By reducing the NEG thickness, we can increase the threshold. However, according to [38], a uniform thickness of 100 nm for almost 100 km of vacuum chamber could not be guaranteed [39].

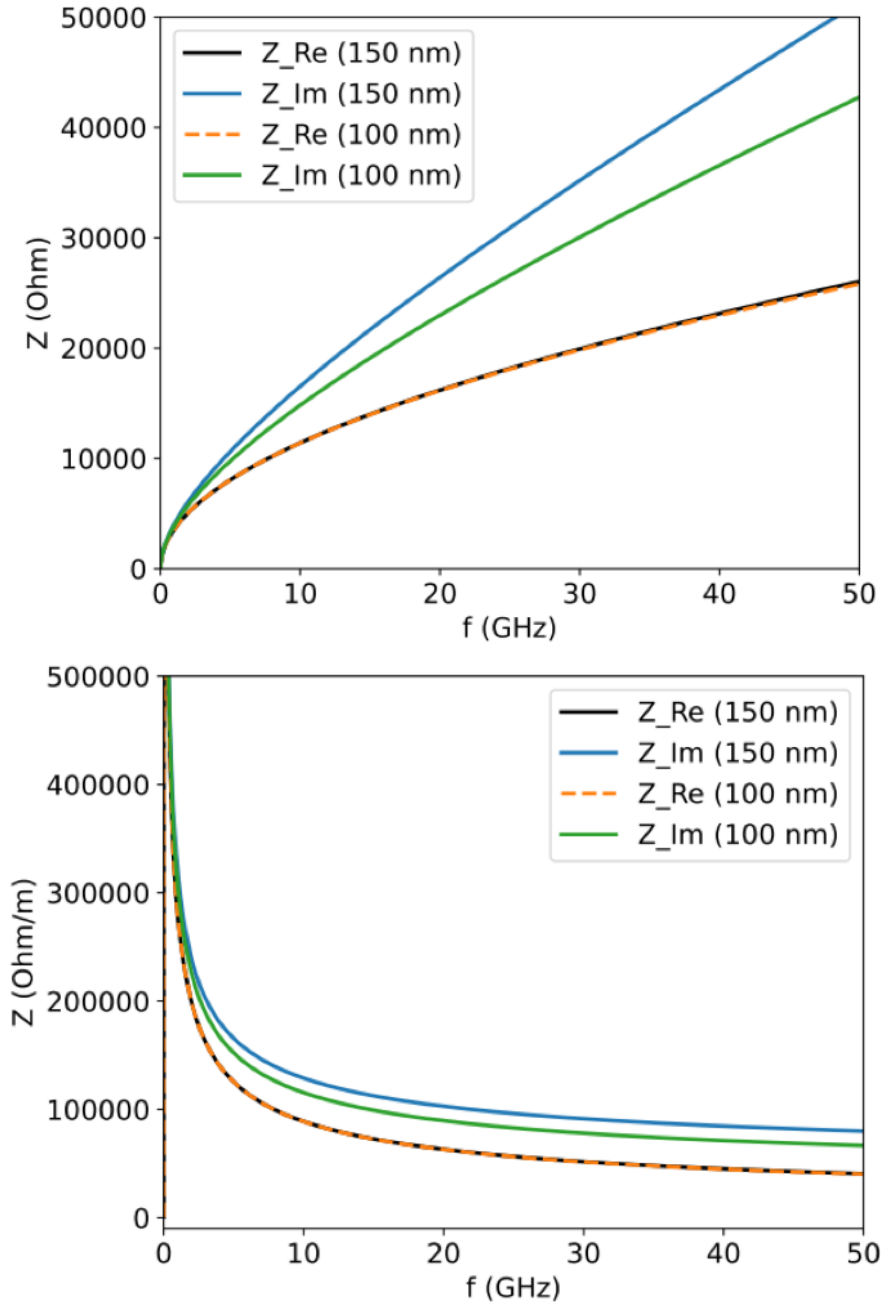


Figure 2.6: Longitudinal and transverse impedances, respectively, for the case of 150 nm and 100 nm of NEG.

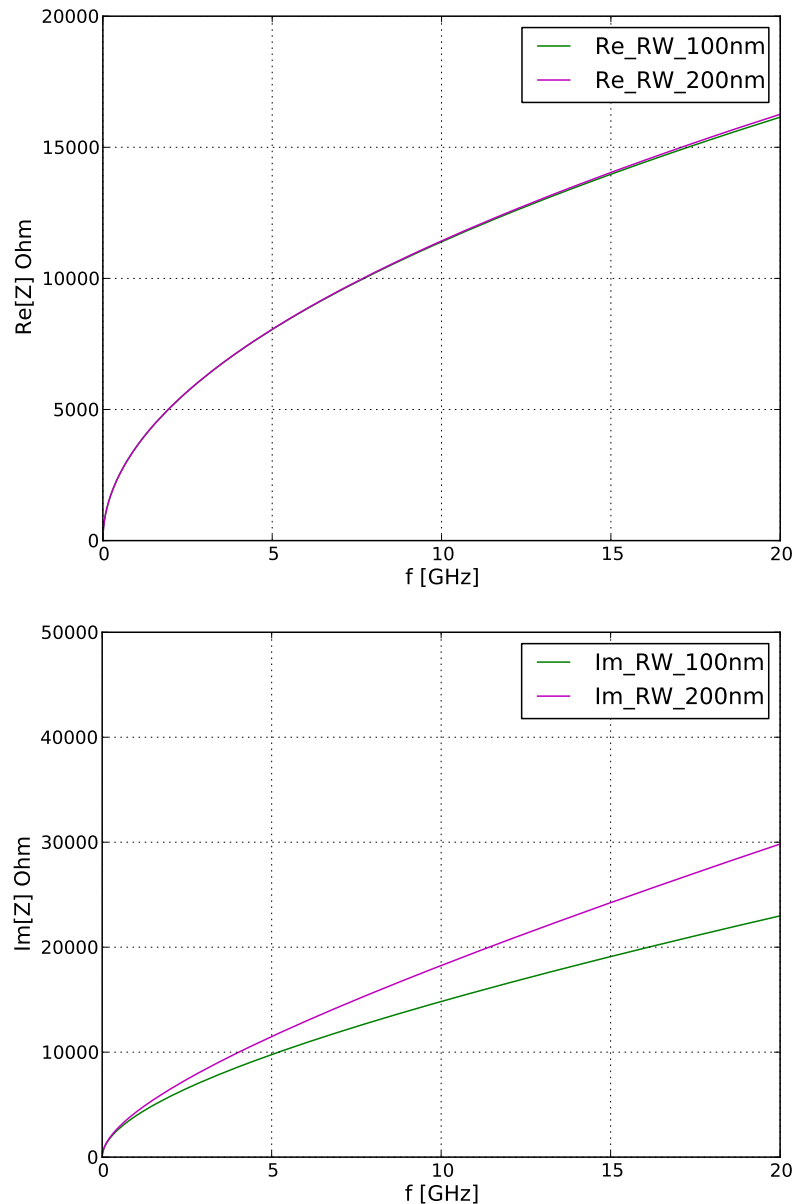


Figure 2.7: Real (top) and imaginary (bottom) part of the impedance, for the case of 200 nm and 100 nm of NEG.

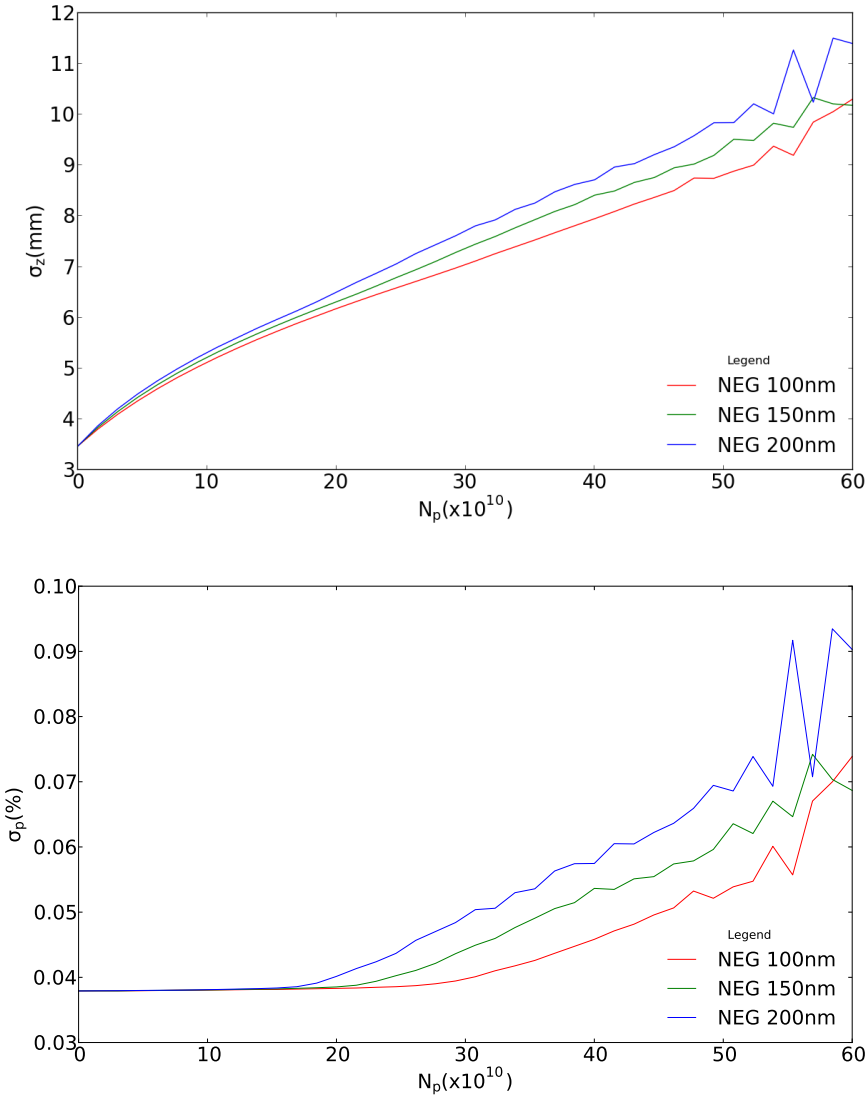


Figure 2.8: PyHT simulation results. Bunch length and energy spread as a function of intensity for three different NEG thickness models: 200 nm, 150 nm, and 100nm.

Moreover, in order to implement a more realistic model in our new simulations, we have, also, taken into account the small perturbations introduced by the lateral winglets necessary for synchrotron radiation absorption, as shown in Fig. 2.9. Since IW2D considers only circular or flat geometries, in order to evaluate the winglets we used CST. This software, is not optimised to evaluate the RW impedance for a multi-layer system because it considers the surface impedance due to the first layer. To overcome the problem, we used a model with a low conductivity material, $\sigma_c = 10^5 S/m$, but still in a good conductor regime, to evaluate the impedance of a single thick wall in order to find an impedance not too small which could have had the same order of magnitude of the numerical noise, as described in [3]. After calculating the impedance of the CST model, we divided it by its surface impedance considering just one layer, Z_{s1} and multiplied it by the surface

impedance but considering two layers, NEG and copper, given by [40]

$$Z_{s2}(\omega) = (1 + j) \sqrt{\frac{\omega Z_0}{2\sigma_c c} \frac{\alpha \tanh \left[\frac{1+j}{\delta_1} \Delta \right] + 1}{\alpha + \tanh \left[\frac{1+j}{\delta_1} \Delta \right]}}. \quad (2.27)$$

In this equation σ_c is the coating conductivity, Z_0 the vacuum impedance, Δ is the thickness of the coating, δ_1 the skin depth of the coating and δ_2 the skin depth of the substrate, supposed to be infinite. For a good conductor $\alpha \approx \delta_1/\delta_2$. In Fig. 2.10 we show the final impedance, for the longitudinal and transverse planes, and the results of IW2D of a circular geometry with four layers and multiplied by a factor of 1.1 in both planes. We considered a range of frequency up to 30 GHz because in CST we used a Gaussian bunch of 2 mm having then a cut-off frequency of almost 24 GHz. From the comparison, we can say that in this frequency range the results are in a good agreement. Due to the lossy metal material type used, we can observe a marginal difference for the real part of the transverse impedance of CST at small frequency.

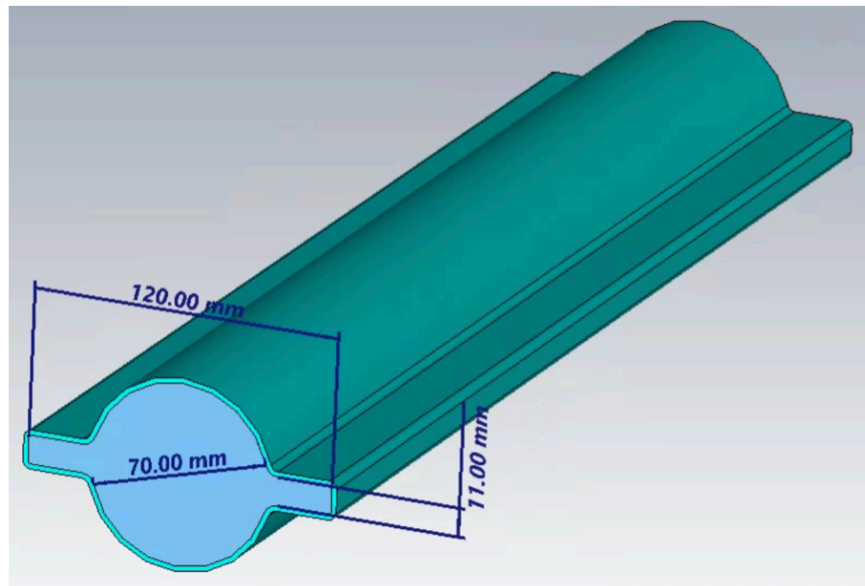


Figure 2.9: CST pipe shape model considering a more realistic representation, without neglecting lateral winglets.

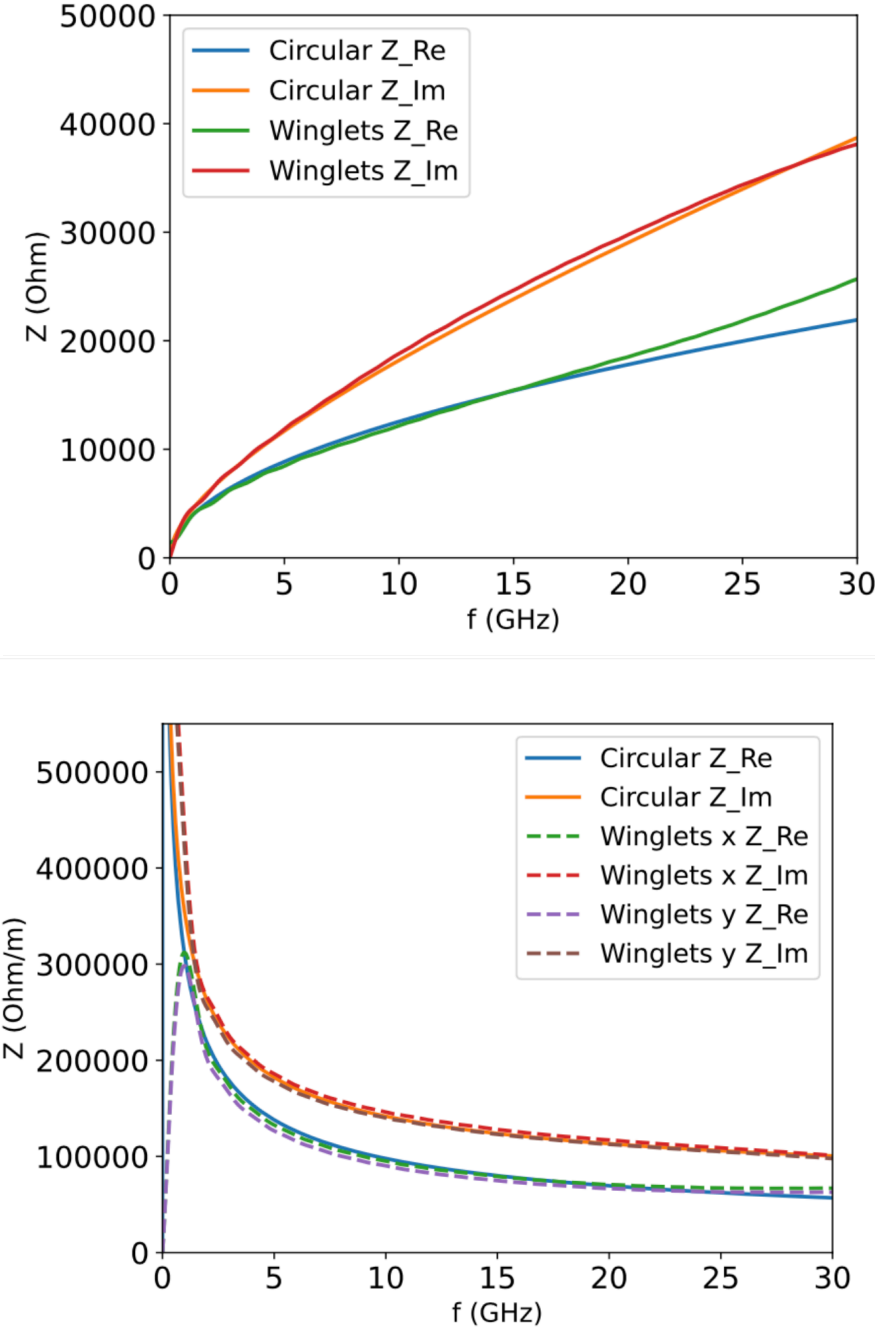


Figure 2.10: Resistive wall longitudinal (top) and transverse (bottom) impedance for FCC-ee obtained with CST considering the realistic model of the winglets and compared with the results of IW2D with four layers for a circular pipe, and multiplied by a factor 1.1 [3].

From the results, we can conclude that the winglets produce a very small perturbation to the resistive wall impedance of the order of 10% or even less. For taking into account this effect, we have then multiplied the impedance of the circular pipe, given by IW2D, by a factor 1.1. Moreover, due to the breaking of the cylindrical symmetry, the winglets also give a contribution to the quadrupolar impedance. However, by using this method, we observed that the quadrupolar impedance is a factor of about 20 less than the dipolar one. Therefore, in beam dynamics studies, we neglect this quadrupolar contribution.

2.3.2 PyHEADTAIL

PyHEADTAIL [41] is a time-domain macro-particle code, used at CERN to study coherent instabilities in the presence of wake fields, space charge, and feedbacks. The simulated bunch is supposed to be made up of macro-particles, each one tracked through the machine. In the simulations of FCC-ee we use between 10^6 and 2×10^6 macro-particles. However, for collective effects, we are not much interested in the microscopic motion of the single macro-particle that is irrelevant to coherent beam instabilities. It is the macroscopic motion, i.e. modes having wavelengths in the order of the beam pipe or the bunch length dimensions, that are of interest. The bunch can be studied as a whole and its coherent modes of oscillation can be analyzed in the frequency domain or taking into account the wakefields [8], by considering some global parameters such as the longitudinal and transverse oscillations of the bunch centre of mass, the root mean squares of the phase space distributions (bunch length, energy spread, transverse RMS dimensions,...). The particles in the bunch head generate a wake, affecting, due to the causality principle, the bunch tail. The energy variation ΔE_i and the dipolar wake kick $\Delta x'_i$ in macro-particle i caused by all other macro-particles are :

$$\Delta E_i = -e^2 \sum_{j=1}^N W_{\parallel}(z_{ij}) \quad (2.28)$$

$$\Delta x'_i = -\frac{e^2}{\beta^2 E_0} \sum_{j=1}^N W_x^{dip}(z_i - z_j) \Delta x_j \quad (2.29)$$

Applying these formulas to each of the 10^6 macro-particle along the ring and for several thousands of turns would be computationally impossible. Instead, the bunch is sliced longitudinally, as schematized in Fig. 2.11.



Figure 2.11: The figure shows the principle of beam slicing for PyHT. On the left, the bunch is represented as a collection of macro-particles. We have to evaluate the effect of the wakefield generated by all the macro-particles on the red one. In order to decrease the calculation time, the bunch is instead sliced as pictured on the right. In each slice there are several thousands of macro-particles, and it is the effect of all slices on the red one that is computed. Pictures courtesy of M.Schenk [4]

The wake can be considered constant inside the slice for thin enough slices. The energy variation ΔE_i and the wake kick $\Delta x'_i$ generated by all the slices j located upstream (for the causality principle) of slice i are then calculated and summed to obtain the wake kick acting on the selected slice:

$$\Delta E_i = -e^2 N[i] \sum_{j=0}^i N[j] W_{\parallel}[(i-j)\Delta z] \quad (2.30)$$

$$\Delta x'_i = -\frac{e^2}{\beta^2 E_0} \sum_{j=1}^{N_{\text{slices}}} \langle x \rangle_j W_x^{dip}(i-j) \quad (2.31)$$

Where N is the number of macro-particle per slice, Δz is the slice length, and $\langle x \rangle_j$ is the transverse

position average of the $j - th$ slice of bunch. Depending on the beam revolution frequency and on the machine damping time, this whole process is repeated for several thousands of turns. The wake slicing is also crucial since it assumes that the wake is constant within a slice. To understand the sensibility of the simulation to the slices and to check the convergence, we run the same configuration machine by changing the number of slices for each bunch to 500/800/1000, as shown in Fig. 2.12. Modifying the number of slices, consequently changing its thickness. From the results, can conclude that the simulation is not affected by these changes and 500 slices are enough for reliable simulations. The small differences at very high intensities where the bunch is strongly unstable can be neglected since that regime will never be reached in the real machine. Using a wake of 0.4 mm and 500 slices give to us a more stable configuration.

2.4 PyHT simulations: Wake potentials

The coupling impedance and the wakefields due to the resistive wall have been calculated by using the IW2D code, which gives us the wake of a point charge (the so-called Green function) that we can use in our simulations. For the other contributions, we have used other software, such as CST [42] ABCI [43] and ECHO3D [44]. However, they provide not the Green function, that is a wake of a point charge, but a wake of a beam distribution, which, in principle, cannot be used directly in PyHT simulations. However, we found that the wake of a 0.4 mm Gaussian bunch is able to reproduce wakes of longer distributions, with bunch lengths similar to the ones that we have in FCC–ee. In Fig. 2.13 some results due to the resistive wall are presented. In particular, we show the bunch length and energy spread of a bunch of 0.4 mm, having a factor 8.7 lower than the nominal bunch of 3.5 mm (old parameters value), plus two other cases with factors of about 10 and 11 respectively for shorter bunches of 0.35 mm and 0.31 mm. In the plot, the blue line represents a bunch of 0.31 mm, the green line represents a bunch of 0.35 mm and the red one represents a bunch of 0.4 mm. The curves show a quite good convergence of results, indicating that a wake of a Gaussian distribution having a bunch length of 0.4 mm can be used as pseudo-Green function for PyHT simulations.

Furthermore, we checked this method using the wake of other devices. Since CST and other electromagnetic CADs cannot provide the wake of a point charge, we have first obtained directly the wake of a 0.4 mm, 3.5 mm and 12.1 mm Gaussian bunch. These two last quantities correspond to the FCC–ee nominal bunch lengths of the CDR without and with beamstrahlung. Then we have convoluted the wake of the shortest bunch distribution, as if it was a Green function, with 3.5 mm and 12.1 mm Gaussian bunches and have compared the results with the direct wake given by CST.

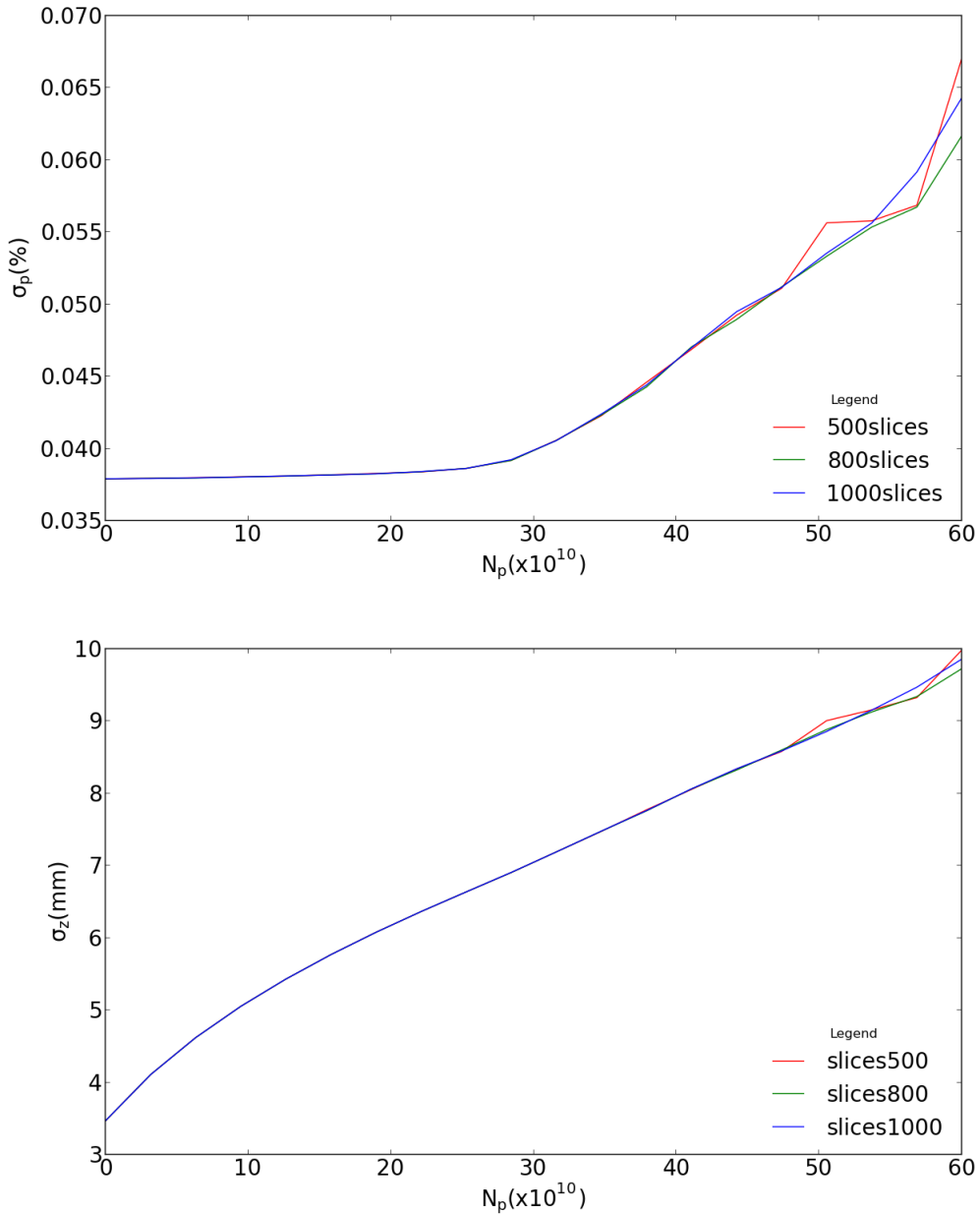


Figure 2.12: Energy spread (top) and bunch length (bottom) for different values of slices with a nominal bunch length of 3.5 mm and using the same number of macro-particles.

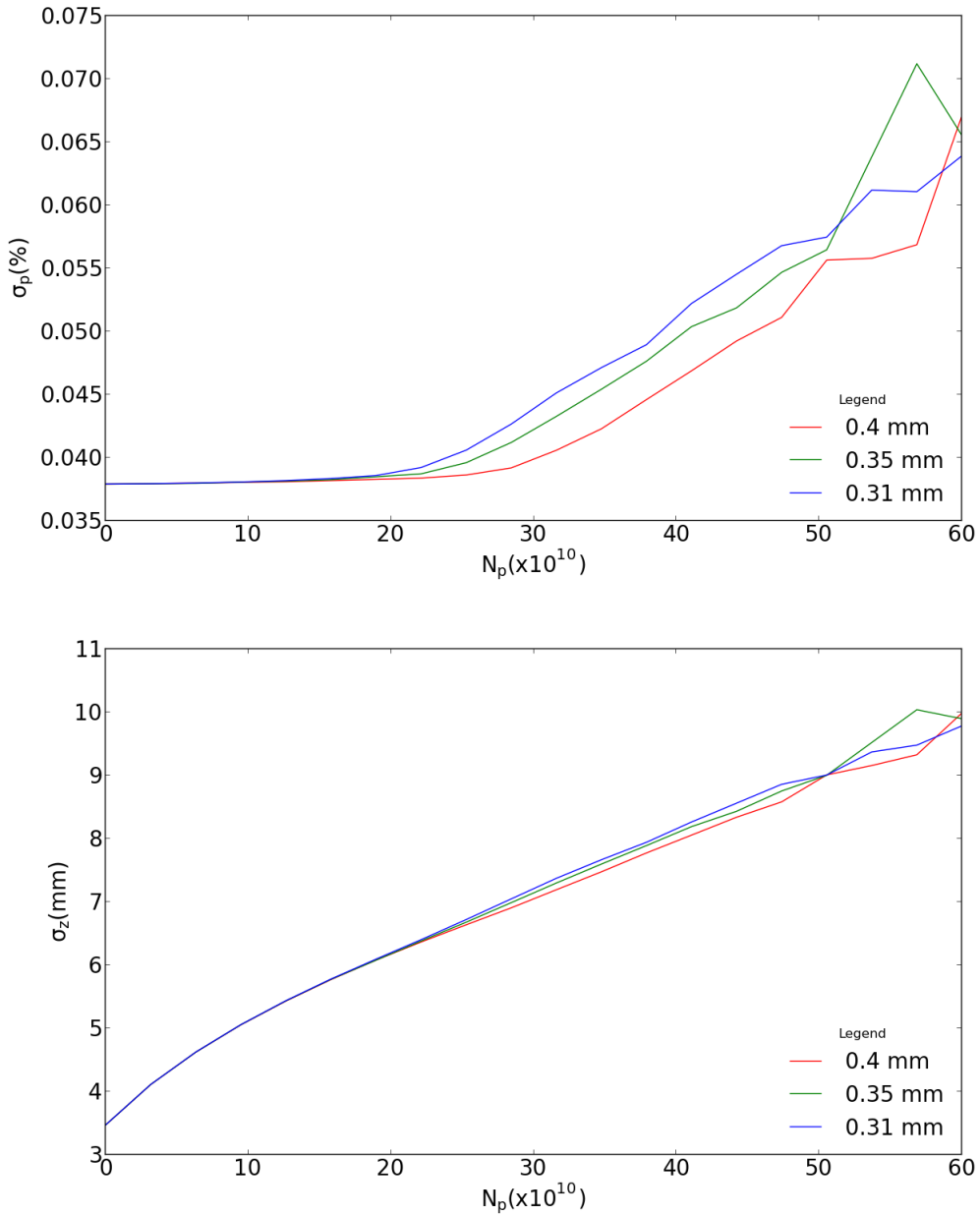


Figure 2.13: Energy spread (on the top) and bunch length (on the bottom) as a function of bunch population using, as pseudo Green function, the wake of different short bunches, 0.4 mm, 0.35 mm and 0.31 mm.

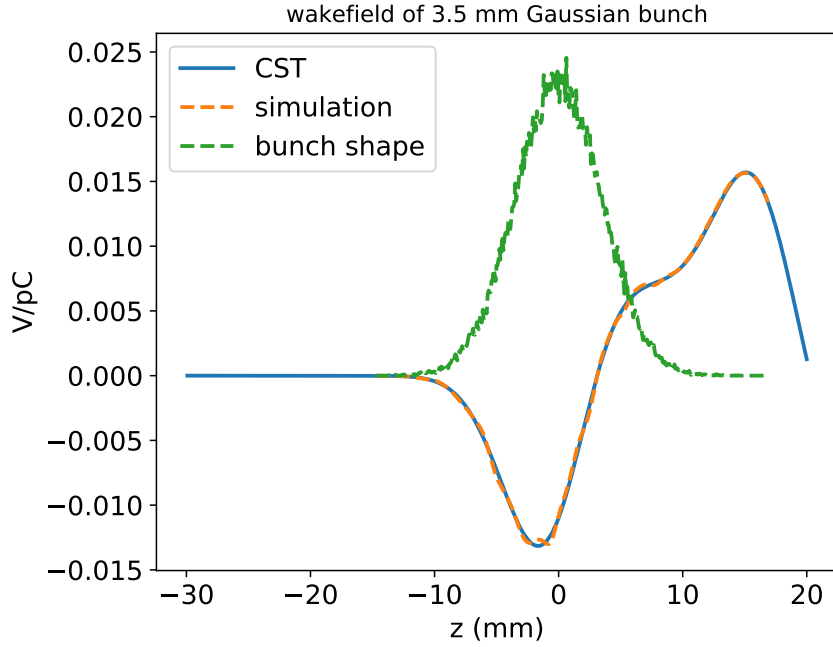


Figure 2.14: Wake potential for a Bellow of a 3.5 mm Gaussian bunch obtained directly by CST (blue curve) and with the convolution by using the wake potential of 0.4 mm Gaussian bunch (orange dots), the "pseudo Green-function".

In Fig. 2.14 we can see this comparison applied to the bellows for a wakefield of 3.5 mm and in Fig. 2.15 for a wakefield of 12.1 mm. In the figures, the "simulation" curves have been obtained by PyHT using, as Green function, the wake of the 0.4 mm Gaussian bunch. These plots show excellent agreement. In Fig. 2.16 we represented the results for the RF cavity, in Fig. 2.17 for the

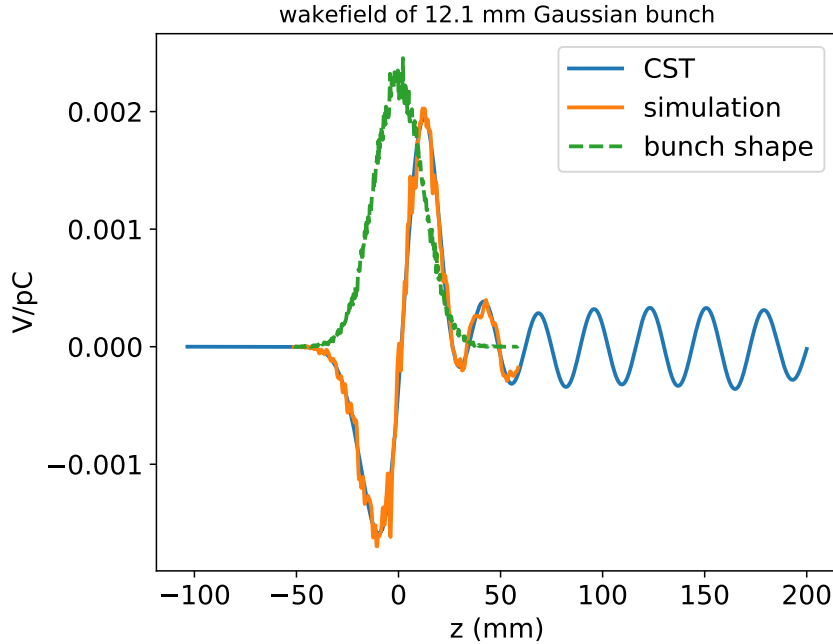


Figure 2.15: Wake potential for a Bellow of a 12.1 mm Gaussian bunch obtained directly by CST (blue curve) and with the convolution by using the wake potential of 0.4 mm Gaussian bunch (orange curve), the "pseudo Green-function".

BPM and in Fig. 2.18 for the RF Taper.

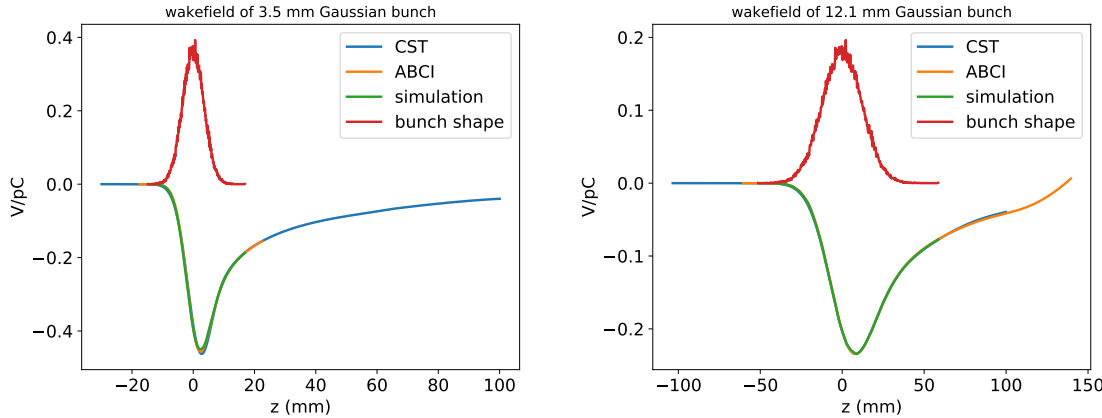


Figure 2.16: Wake potential for an RF cavity of a 3.5 (left) and 12.1 mm Gaussian bunch (right) obtained directly by CST (blue line), with convolution by using the wake potential of 0.4 mm Gaussian bunch (green line) and with the result obtained directly by ABCI (orange line), the "pseudo Green-function".

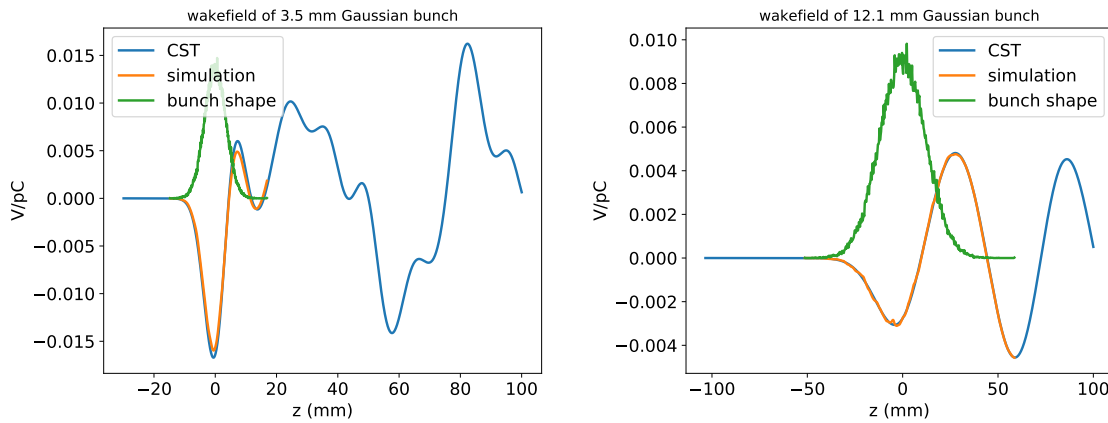


Figure 2.17: Wake potential for a BPM 3.5 and 12.1 mm Gaussian bunch obtained directly by CST (blue line) and with the convolution using the wake potential of 0.4 mm Gaussian bunch (orange line), the "pseudo Green-function".

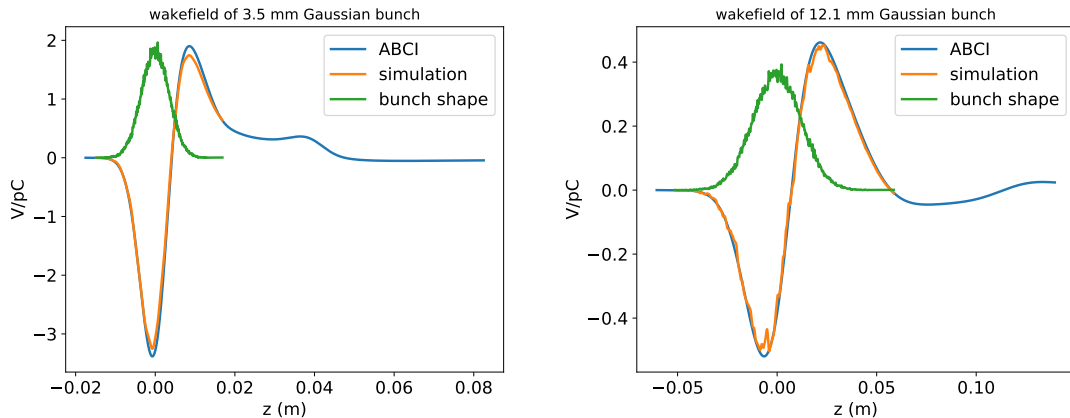


Figure 2.18: Wake potential for Taper of 3.5 and 12.1 mm Gaussian bunch obtained directly by ABCI (blue line) and with the convolution using the wake potential of 0.4 mm Gaussian bunch (orange line), the "pseudo Green-function".

All of these plots show a very good agreement, indicating that we are able to reconstruct the wake potential of longer bunches, by using the wake of 0.4 mm Gaussian bunch as a pseudo Green

function.

For the RW contribution instead, IW2D gives, as the result, the wakefield of a point charge. Nevertheless, for self-consistency with the other contributions, also in this case we have obtained the wake potential of a 0.4 mm Gaussian bunch as Green function to be used in simulations and, in Fig. 2.19 we show the comparison as for the previous cases.

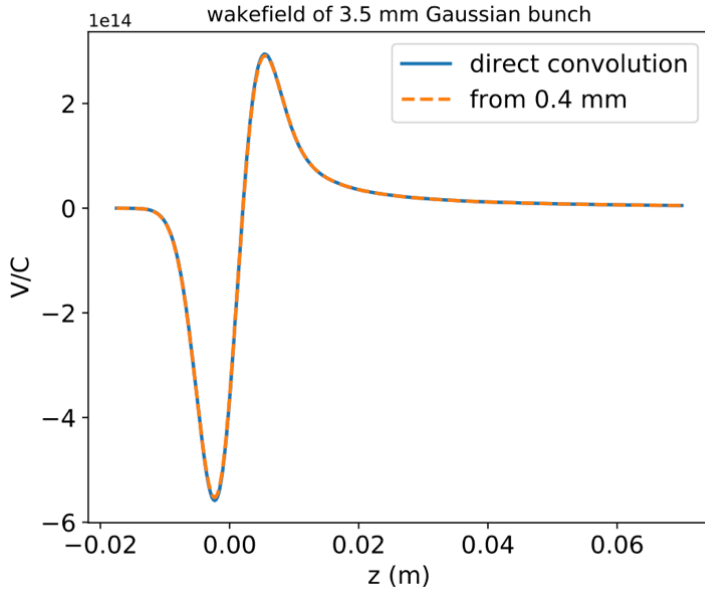


Figure 2.19: Resistive wall wake potential of a 3.5 mm Gaussian bunch (blue line) and the wake potential obtained as convolution by using the wakefield (orange curve).

2.5 Machine Devices

In this section we will have look more in detail in some machine devices, such as bellows, BPMs and collimators.

2.5.1 Wake potential and loss factor

In recent years, machine parameters have changed several times. For example, in the table 2.1 we show the ones of the CDR used for initial simulations.

The most interesting configuration for collective effects regards the lower energy configuration machine. The circumference was almost 98 km, and only two IPs were considered. The major differences with respect to the latest parameters are in the values of bunch length, energy spread, momentum compaction and the four IPs. The contribution of several machine components to the impedance budget was first obtained with the initial nominal bunch length of $\sigma_z = 3.5\text{mm}$. Figure 2.20 shows the first results of the longitudinal wake potentials of each component. The figure clearly shows the relevant RW contribution of a 100 nm NEG coating, which dominates with respect to the other impedance sources.

Table 2.2 summarizes the corresponding loss factors. The major contribution, as expected, is given by the RW with a total loss factor, at nominal intensity and bunch length, of 210 V/pC. The total dissipated power at nominal intensity is 13.7 MW, about a factor 3.7 smaller than the total SR power dissipated by the beam of 50 MW [1].

Table 2.1: Old FCC–ee key parameters.

	Z	W	H	tt	
Beam energy [GeV]	45.6	80	120	175	182.5
Circumference C [km]			97.75		
RF frequency f_{RF} [MHz]			400		
Arc cell	60°/60°	60°/60°	90°/90°	90°/90°	90°/90°
RF voltage V_{RF} [GV]	0.1	0.75	2.0	8.8	10.3
Momentum compaction α_c [10 ⁻⁵]	1.48	1.48	0.73	0.73	0.73
Horizontal tune Q_x	269.14	389.124	389.13	389.108	389.108
Vertical tune Q_y	267.22	391.20	391.20	391.18	391.18
Synchrotron tune Q_s	0.025	0.0506	0.0358	0.0598	0.0622
SR energy loss/turn U_0 [GeV]	0.036	0.34	1.72	7.8	9.2
Longitudinal damping time τ_l [ms]	415	77	23	7.5	6.6
Beam current I [mA]	1390	147	29	6.4	5.4
Number of bunches/ring	16640	1300	328	40	33
Bunch population N [10 ¹¹]	1.7	2.3	1.8	3.2	3.35
Horizontal emittance ε_x [nm]	0.27	0.84	0.63	1.34	1.46
Vertical emittance ε_y [pm]	1	1.7	1.3	2.7	2.9
Energy spread					
$-\delta_{dp,SR}$ [%]	0.038	0.066	0.099	0.144	0.150
$-\delta_{dp,BS}$ [%]	0.132	0.165	0.165	0.196	0.2
Bunch length					
$-\sigma_{z,SR}$ [mm]	3.5	3.0	3.15	2.75	2.76
$-\sigma_{z,BS}$ [mm]	12.1	7.5	5.3	3.82	3.78

Table 2.2: Power loss contribution of the main FCC–ee components at nominal intensity and bunch length of $\sigma_z = 3.5\text{mm}$ and 12.1 mm (old configuration machine), in the lowest energy case of 45.6 GeV.

Component	Number	K_{loss} (3.5 mm) [V/pC]	K_{loss} (12.1 mm) [V/pC]	P_{loss} [MW]
Resistive wall	97.75 km	33.1	210	7.95
RF cavities	56	18.5	9.44	0.7
BPMs	4000	40.1	4.81	1.5
Bellows	8000	49.0	$4.7e^{-5}$	1.8
RF double tapers	14	26.6	2.5116	1.0
Total		362.9	226.76	13.7

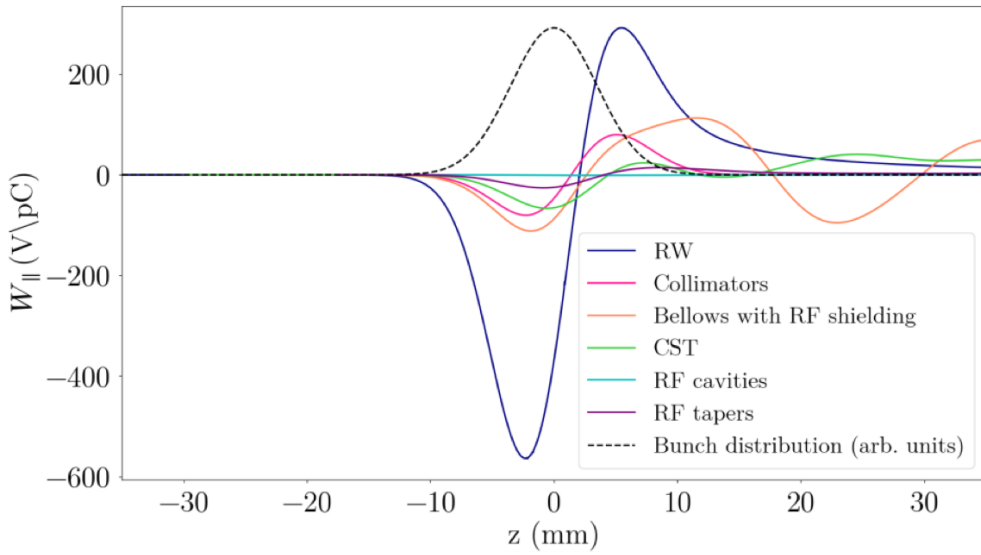


Figure 2.20: Longitudinal wake potentials for a Gaussian bunch with nominal bunch length $\sigma_z = 3.5\text{mm}$ due to the main FCC-ee components, considering an old configuration machine.

In the same table, we also show the loss factors when we consider additional effect of beamstrahlung (BS).

After the first evaluation of impedance and collective effects, some changes have been made to the parameter list. Firstly, Fig. 2.21 shows an updated study of the bellows. It has been performed in three different steps: the first one is a simplified CST model, in the second one we have added the lateral winglets and the last one is a more realistic model designed by a mechanical CAD. Since the realistic model required heavy computational resources, preliminary simulations, carried out using more simplified CST models, helped in the interpretation and the correctness of the results.

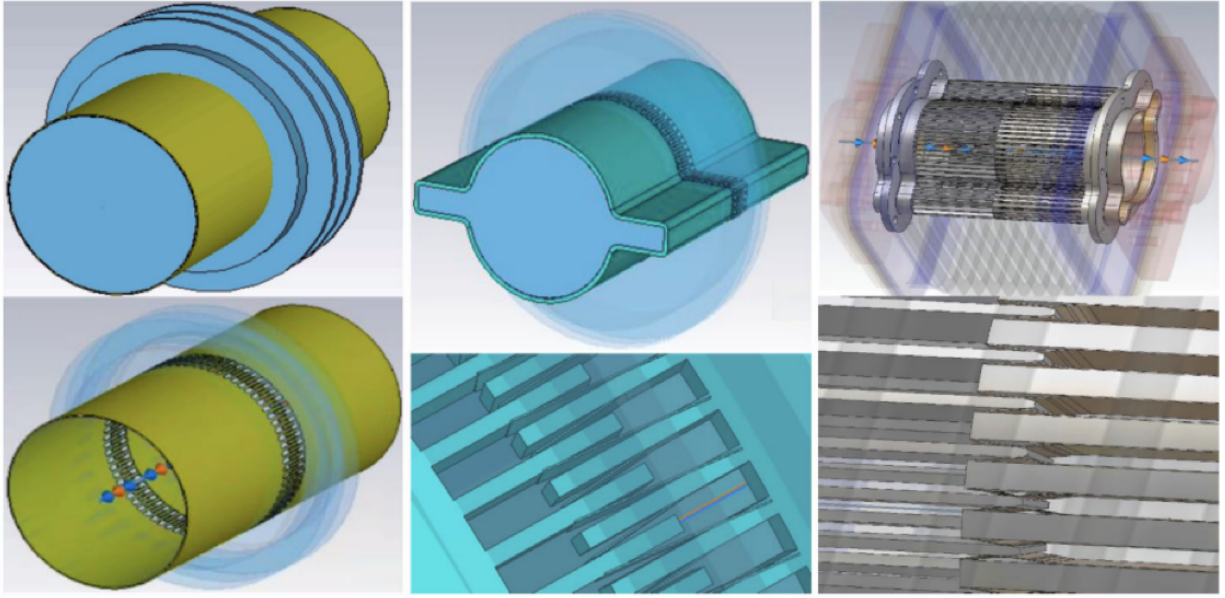


Figure 2.21: Simulated models of FCC–ee beam vacuum chamber including bellows. On the left there is a simplified model with circular geometry (Circular, green line in the Fig. 2.22), in the centre a simplified model with winglets (Winglets, orange line in the Fig. 2.22), on the right the realistic model of the bellow including RF fingers (Realistic, blue line in the Fig. 2.22).

For all the considered models, longitudinal and transverse simulations have been performed with the wakefield solver of CST. In Fig. 2.22 we show the result of the longitudinal wake potential, and corresponding impedance with a 3.5 mm Gaussian bunch by considering a single bellow.

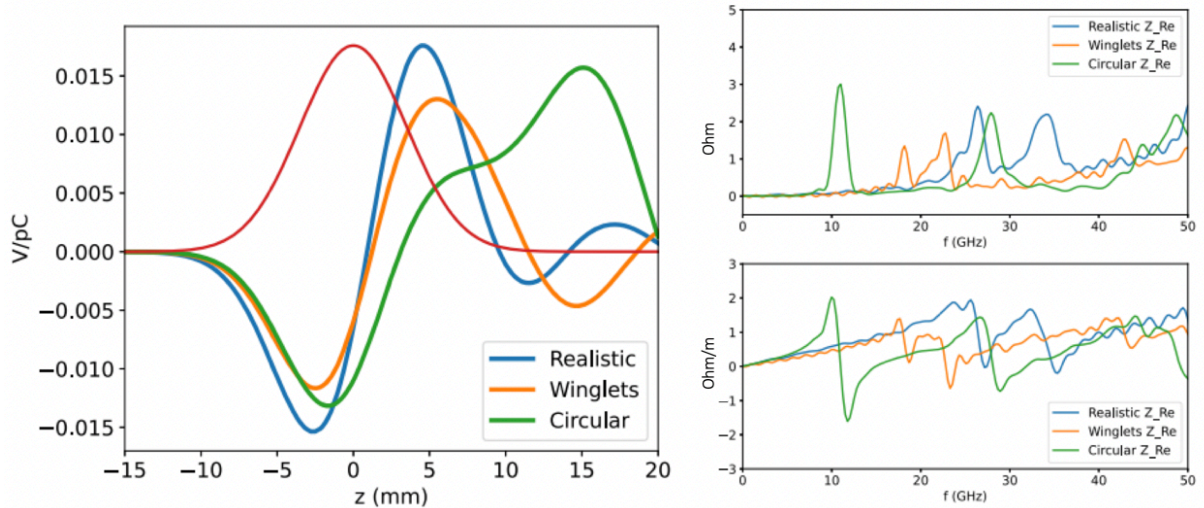


Figure 2.22: Longitudinal wake potential and impedance for the three studied models of the bellow.

It is noticeable that the first resonance of the circular model, around 11 GHz, is missing in both the other two models with the winglets. A deeper investigation of this behaviour showed that this first resonance is related to the coupling between the beam vacuum chamber and the cavity of the bellow [3]. For what concerns the transverse plane in the realistic model the dipolar impedance is negligible at the low frequency, and the first resonance appears above 20 GHz Fig.

2.22. Even if the impedance contribution of a single device is negligible in the whole machine, we have a very large number of them. Indeed, even if the exact number is still unknown, we considered 2900 dipole arcs 24 m long with bellows every 8 m (Kersevan, private communication), plus 2900 quadrupoles/ sextupoles arcs in the CDR [22], we have a total of 11600 bellows. Additionally, we need to take into account the bellows for the RF system, injection system, collimation, etc. Overall, to be conservative, we have overestimated them by considering a total number of 20000 bellows. All the beam dynamics results updated with respect to the CDR and taking into account collective effects presented in this thesis have been performed with this number of bellows. Very recently we obtained a first table of the collimation system (presented in section 2.8) and started to evaluate the impedance contribution due to the collimators so that it is possible to reduce the number of the bellows to a more realistic value. Additionally, the vacuum group [38] is now planning to place a bellow in the dipole arcs every 12 m instead of 8 m. This further reduces them to about 9000, which is the number that will be used in future simulations when the collimation system, which is supposed to be another very important source of impedance contribution, could be included in the machine impedance model.

Figures 2.23 and 2.24 show the difference between having 20000 bellows and 8000 in the longitudinal plane, both in terms of wake potential and of effects on beam dynamics, in particular for bunch length and energy spread, which suggest a reduction of the microwave instability threshold.

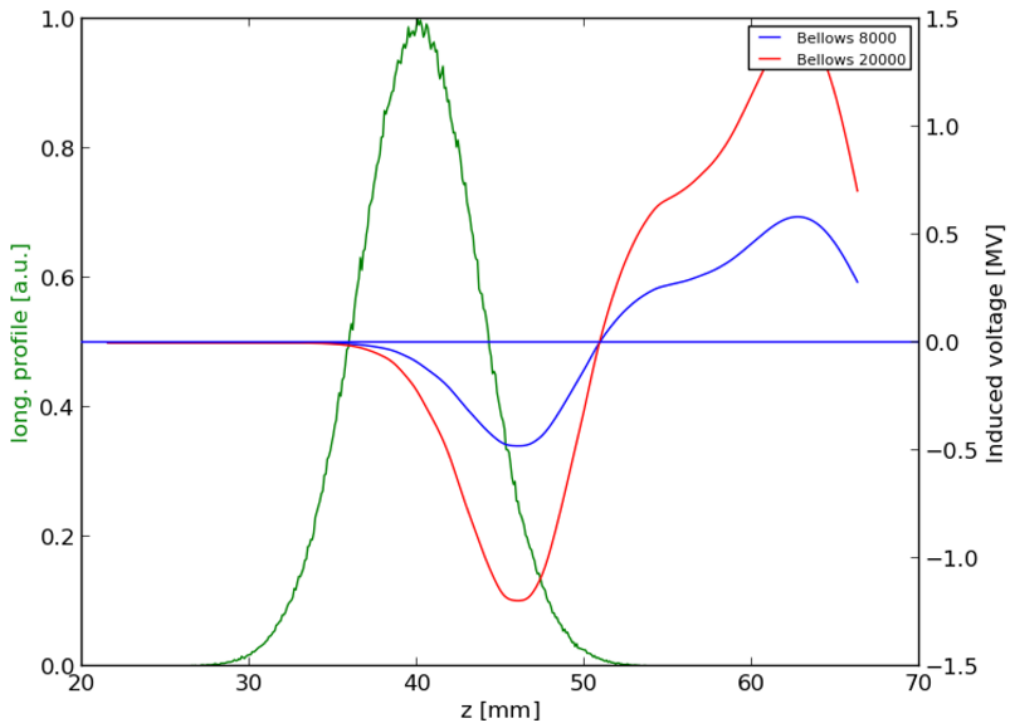


Figure 2.23: Comparison between the induced voltage (total wake multiplied by the bunch charge) produced by 8000 bellows (blue line) and, 20000 bellows (red line) for the same machine configuration, bunch length of 3.5 mm.

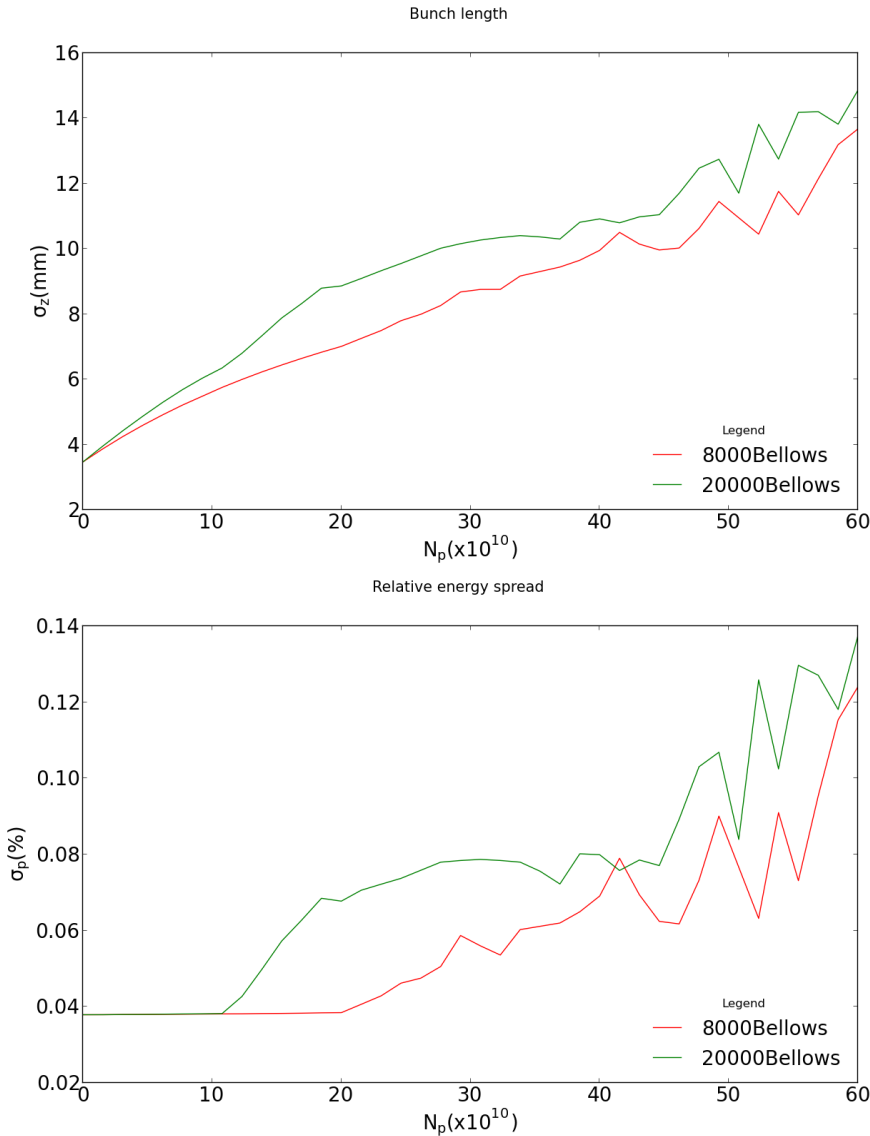


Figure 2.24: Microwave instability analysis considering a number of 8000 bellows and a number of 20000 bellows. Shown are the rms bunch length in mm (top) and the rms energy spread in % (bottom) as a function of the bunch population in units of 10^{10} . The microwave threshold is reached where the energy spread starts to increase.

Other changes of the devices from the CDR have been: a reduction of the number of RF tapers from 14 to 13 and a reduction in the number of RF cavities from 56 to 52. Table 2.3 shows the relative loss factor and power loss for the updated machine configuration when we consider a bunch length of 12.1 mm, the old parameter, to include the BS effect.

Of course, when the number of components is changed, the impedance budget changes. In relation to the updated impedance model with respect to the CDR, in Figure 2.25 and 2.26 the longitudinal and transverse wake potential of a 0.4 mm Gaussian bunch is shown. For the RW, we also used as NEG film thin 150 nm instead of 100 nm, because this number can guarantee a more uniform thickness all over the machine. It is important to observe that the RW and Bellows still represent the main responsible for the machine impedance budget. Moreover, for the transverse contribution, we also specified the dipolar and quadrupolar parts for the bellows, even if so far the quadrupolar contribution can be neglected since it is much lower with respect to the dipolar one.

Table 2.3: $\sigma_z = 12.1\text{mm}$, for the new configuration machine but with the old machine parameters, at nominal intensity and in the lowest energy case of 45.6 GeV.

Component	Number	$K_{\text{loss}} (12.1 \text{ mm}) [\text{V/pC}]$	$P_{\text{loss}} [\text{MW}]$
Resistive Wall	97.75 km	33.1	1.21
RF cavities	52	8.76	0.334
BPMs	4000	4.81	0.180
Bellows	20000	23.95	0.880
RF double tapers	13	2.33	0.088

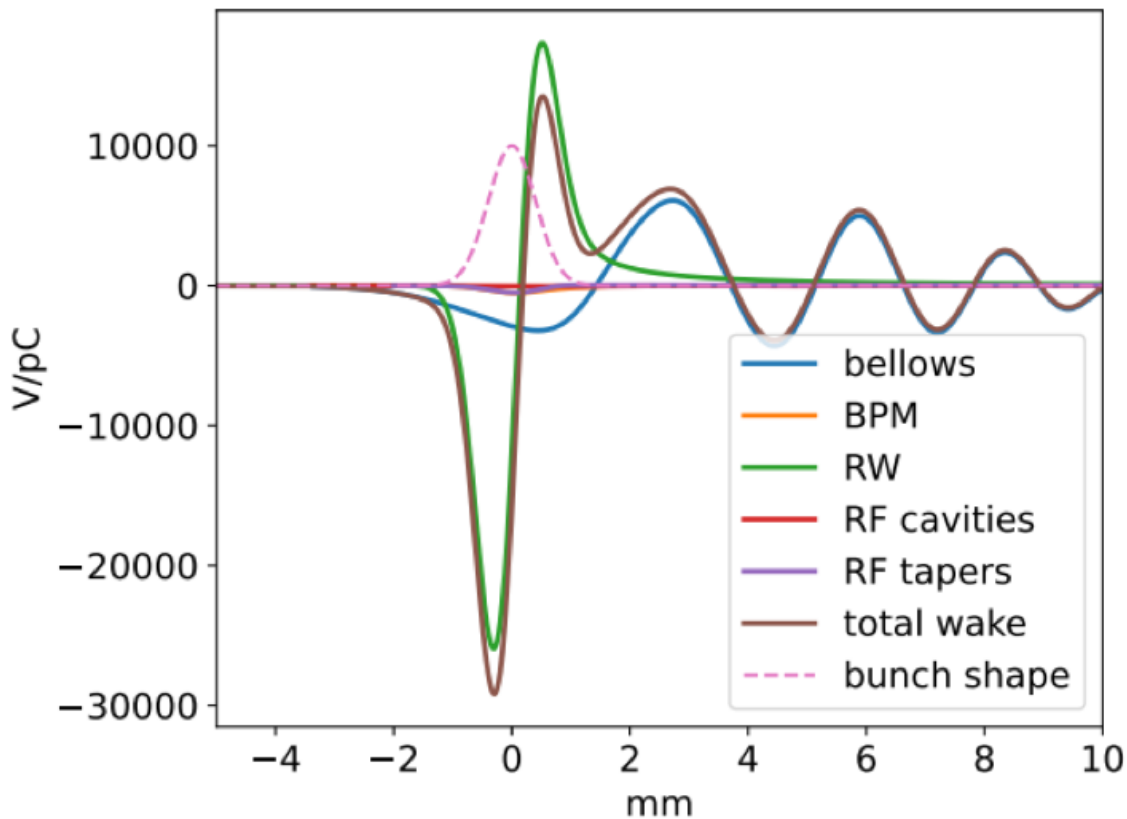


Figure 2.25: Longitudinal wake potential for a 0.4 mm Gaussian bunch due to different devices using the new machine parameters and used as input for beam dynamics simulations

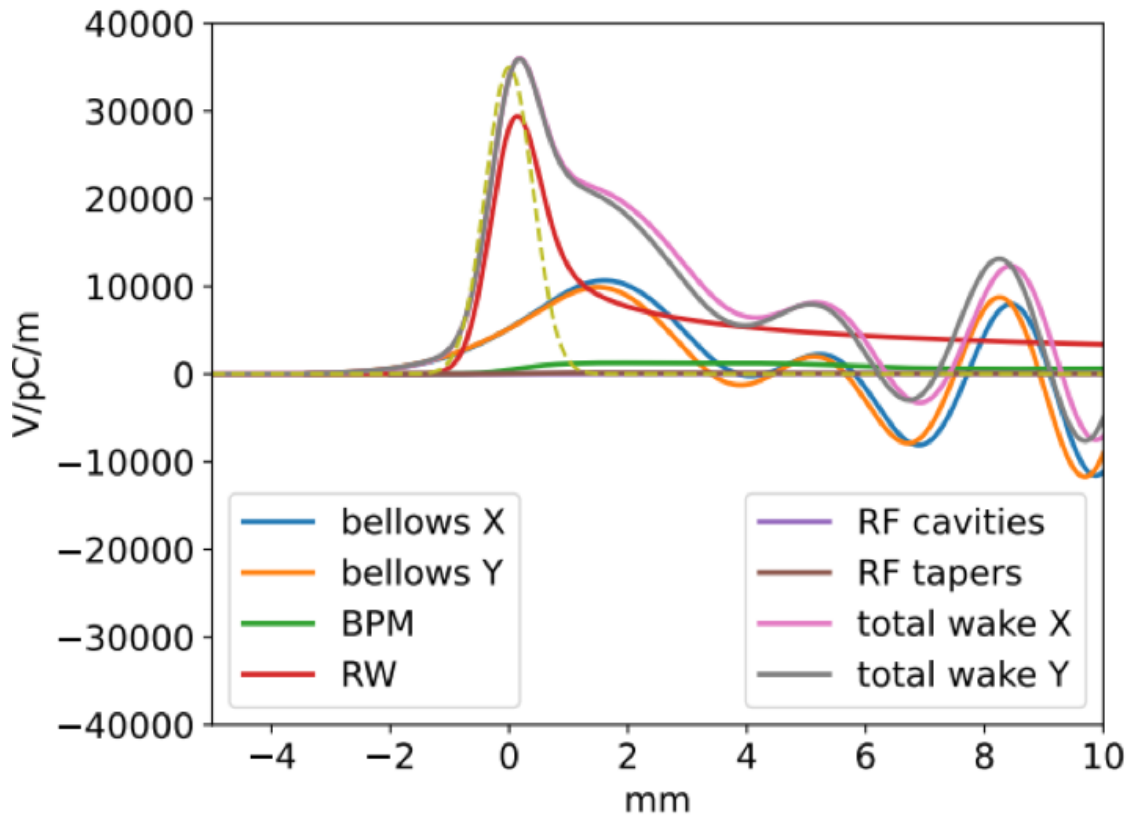


Figure 2.26: Transverse dipolar wake potential for a 0.4 mm Gaussian bunch due to different devices using the new machine parameters.

For the BPMs contribution to the machine impedance, Fig.2.27 shows the model that has been used.

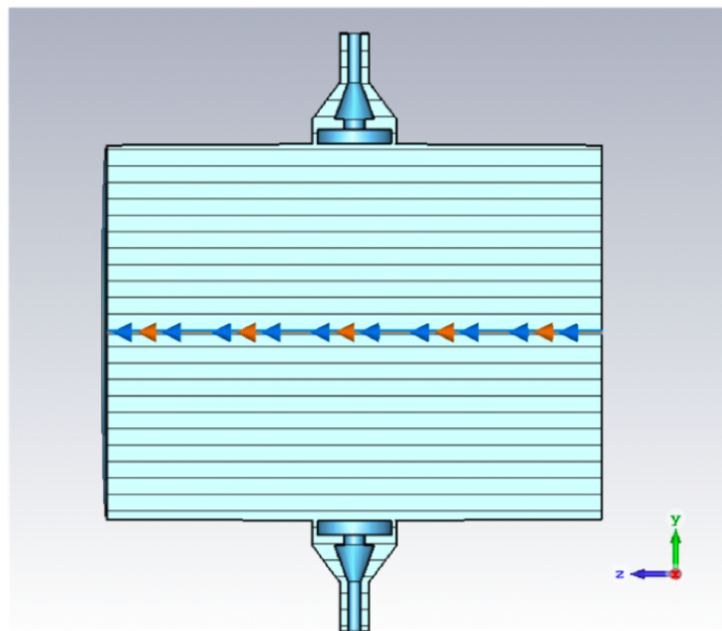


Figure 2.27: CST perspective view of the four-button BPM.

The BPM is designed with a conical button, similar to the one used in SIRIUS, in order to push

the higher order modes trapped in the BPM structure to higher frequencies. Moreover, it will be installed directly on the beam pipe with a rotation angle of 45 degree, eliminating the present of the tapers.

2.5.2 Collimator system

Collimators are one of the main impedance source of the circular lepton collider. Being close to the beam orbit, they may introduce large impedance. In particular, they result very critical in the transverse plane. The collimators are used to remove high amplitude particles from the transverse profile of the beam, to reduce the risk of the uncontrolled beam loss, and they act as shielding for the remainder of the accelerator structures by minimizing the production and leakage of secondary radiation. In order to suppress the background and to cut off the beam halo, FCC-ee will have two type of collimators, beam halo collimators where robustness is one of the key criteria, and SR collimators and masks to intercept photons upstream of the IPs. In order to compensate the loss of the cleaning collimator performance, we use in the FCC-ee long collimators and secondary collimation stages. In particular, the closest ones to the beam will be the primary collimators, which represent the highest contribution to the impedance. The design of the collimators for the FCC-ee is going to be similar to the one used for the SuperKEKB [45] as shown Fig. 2.28 where we show the original SuperKEKB model (left-hand side) and a first adaptation for FCC-ee (right-hand side).

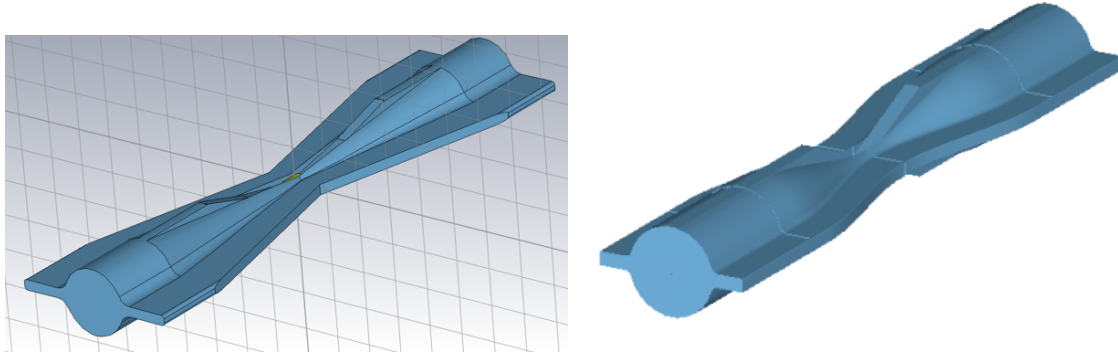


Figure 2.28: CST collimator models for the SuperKEKB (thanks to Takuya Ishibashi), on the left, and for the FCC-ee, on the right.

Fig. 2.29 shows the possible dimensions of the FCC collimator model. It is easy to understand how this model results very complex, and it makes the computation very complicate. On the other hand, in this model the length is much longer than the one of SuperKEKB model. In fact we pass from few mm to 0.3/0.4 m, and this has complicated more the analysis considering that we need to obtain the pseudo-Green function of 0.4 mm Gaussian bunch. The collimation setting is shown in table 2.4. It has been provided by [46]. In the table, both betatron and off-momentum collimators are included, but not the collimators for the synchrotron radiation. An important point emerging from this table is the gap. In particular, we observe that all the vertical collimators have a half gap of about 2 mm. Therefore, the vertical contribution results very important, more than the horizontal one. Moreover, the primary vertical collimators, made by Molidium Grafite, have

a low conductivity and high local β function. All these characteristics make the primary vertical collimators one of the most important impedance source.

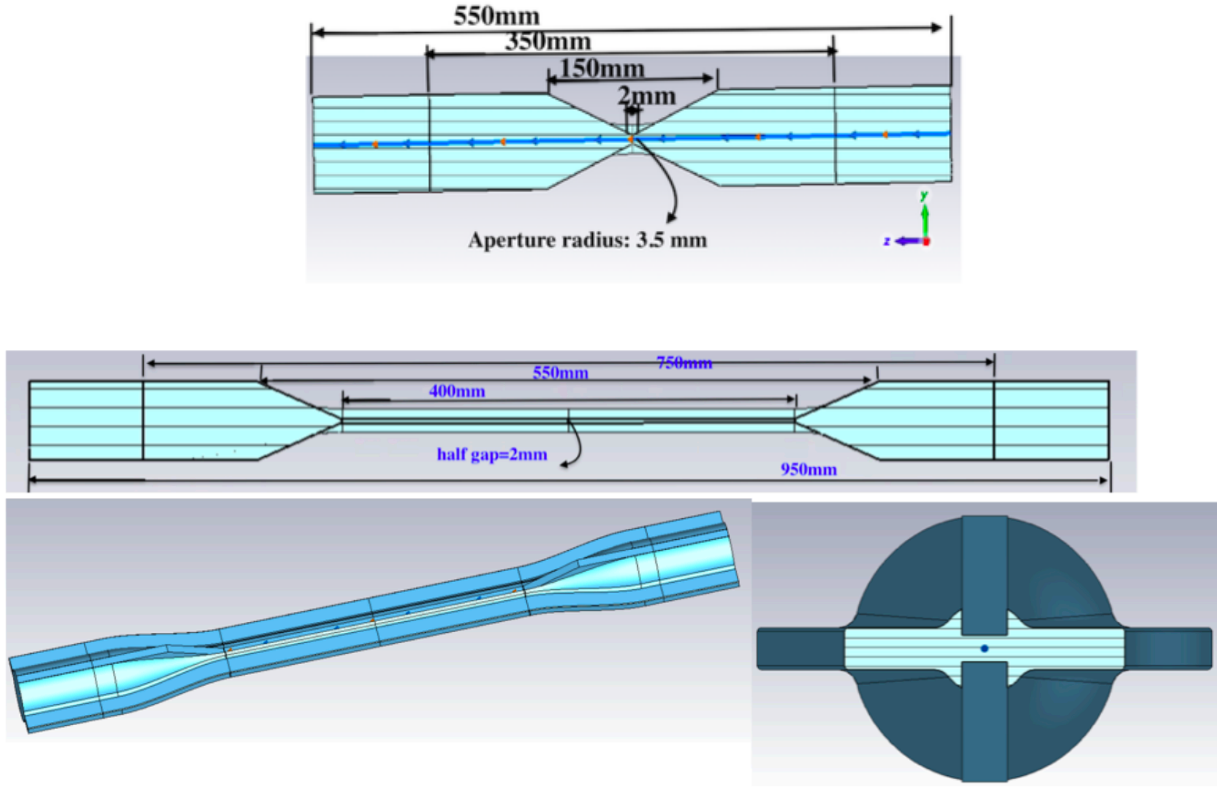


Figure 2.29: Schemes for the collimator models. On the top the scheme of the SuperKEKB model and on the bottom the FCC one.

name	type	length[m]	nsigma	half-gap[m]	material	plane	angle[deg]	offset _x [m]	offset _y [m]	beta _x [m]	beta _y [m]
tcp.h.b1	primary	0.4	11.0	0.005504	MoGR	H	0.0	0.0	0.0	352.578471	113.054110
tcp.v.b1	primary	0.4	65.0	0.002332	MoGR	V	90.0	0.0	0.0	147.026106	906.282898
tcs.h1.b1	secondary	0.3	13.0	0.004162	Mo	H	0.0	0.0	0.0	144.372060	936.118623
tcs.v1.b1	secondary	0.3	75.5	0.00203	Mo	V	90.0	0.0	0.0	353.434125	509.320452
tcs.h2.b1	secondary	0.3	13.0	0.005956	Mo	H	0.0	0.0	0.0	295.623450	1419.375106
tcs.v2.b1	secondary	0.3	75.5	0.002116	Mo	V	90.0	0.0	0.0	494.235759	554.055888
tcp.hp.b1	primary	0.4	29.0	0.005755	MoGR	H	0.0	0.0	0.0	55.469637	995.306256
tcs.hp1.b1	secondary	0.3	32.0	0.01649	Mo	H	0.0	0.0	0.0	373.994993	377.277726
tcs.hp2.b1	secondary	0.3	32.0	0.011597	Mo	H	0.0	0.0	0.0	184.970621	953.229862

Table 2.4: Summary of the collimator settings for the Z mode and for the 4 IP layout. The table includes both betatron and off-momentum collimators. The synchrotron collimators and masks upstream the IP are not included in the table.

For evaluating of the RW part of the collimator impedance, we considered a parallel plate model shown in Fig. 2.30, with infinite thickness and used IW2D. We calculated the impedance for the Molybdenum Graphite and Molybdenum materials with $\sigma_{MoGr} = 10^6 S/m$ and $\sigma_{Mo} = 18.7 \times 10^6 S/m$.



Figure 2.30: For the resistive wall contribution we suppose parallel plates with infinite thickness and use IW2D for the impedance and wakefield evaluation.

In Fig. 2.31 the vertical and horizontal dipolar impedance contribution of all the collimators is shown. It is important to note that the plots have different scales, because the vertical contribution results more critical with respect to the horizontal one. Another important point to highlight is that the plots show the impedance weighted by the β function :

$$Z(\omega) \frac{\beta_{x,y}}{\langle \beta_{x,y} \rangle} \quad (2.32)$$

with $\beta_{x,y}$, local β function and the average of β given by :

$$\langle \beta_{x,y} \rangle = \frac{1}{C} \oint \beta_{x,y} ds = 144.1, 241.5 m \quad (2.33)$$

The last equation is given by [46]. If we used the approximated expression, $\langle \beta_{x,y} \rangle = \frac{C}{2\pi Q_{x,y}}$ we would have obtained 68 m, a factor of 3 lower with respect the previous value. As a consequence, using the formula 5.20 we obtain a contribution of the impedance reduced by this factor.

In Fig. 2.31, the light blue line represents the sum of the collimator contribution, and the tcp_v (primary vertical collimator), the orange line, represents the main collimator impedance source. In the plot the tcs represents the secondary collimator.

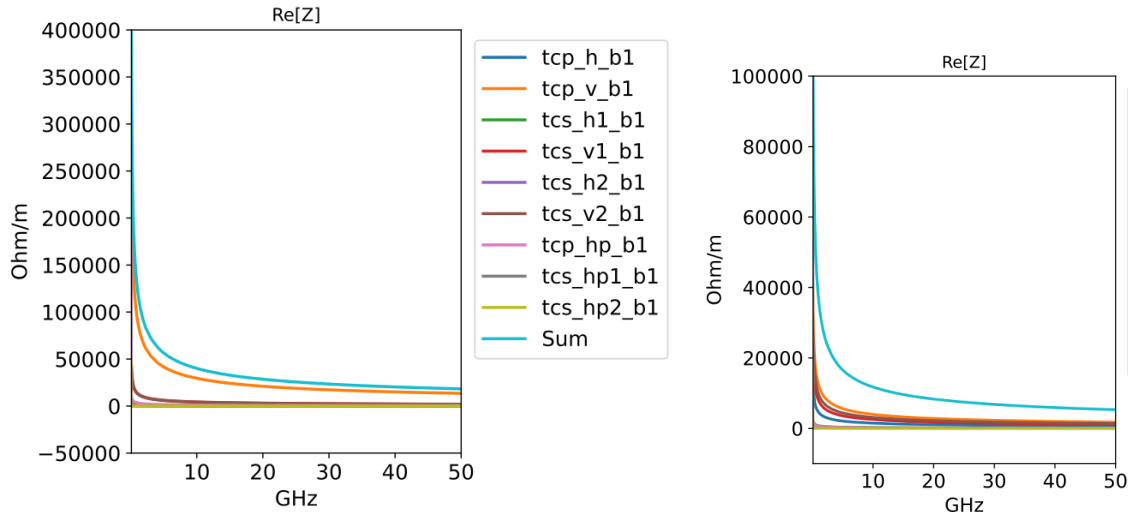


Figure 2.31: Dipolar vertical (left) and horizontal impedance (right) of the collimator system.

The contribution of RW part of the collimators is compared with the other impedance sources. In Fig. 2.32 we show the real and imaginary of the total longitudinal impedance. As expected, the

collimators in this plane give a negligible effect.

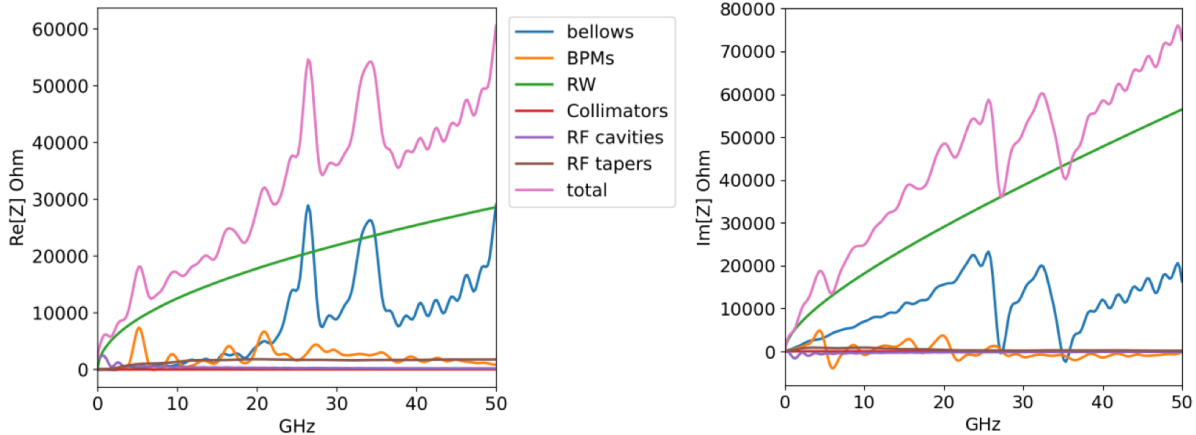


Figure 2.32: Real and imaginary part of the total longitudinal impedance.

In Fig. 2.33 and Fig. 2.34 the dipolar and quadrupolar impedance we show, respectively. We observed that in this case the collimation system represents an important source of impedance.

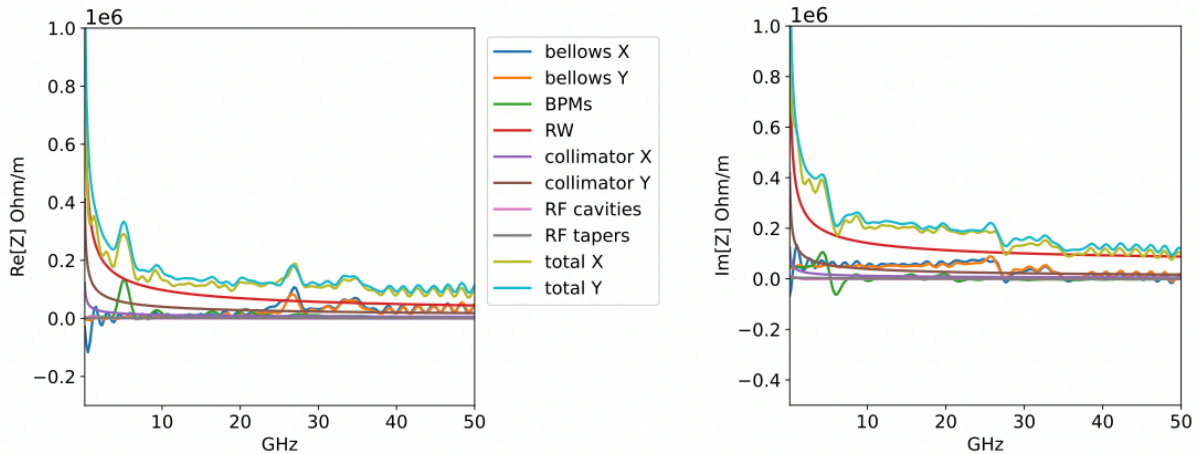


Figure 2.33: Real and imaginary part of the total dipolar transverse impedance.

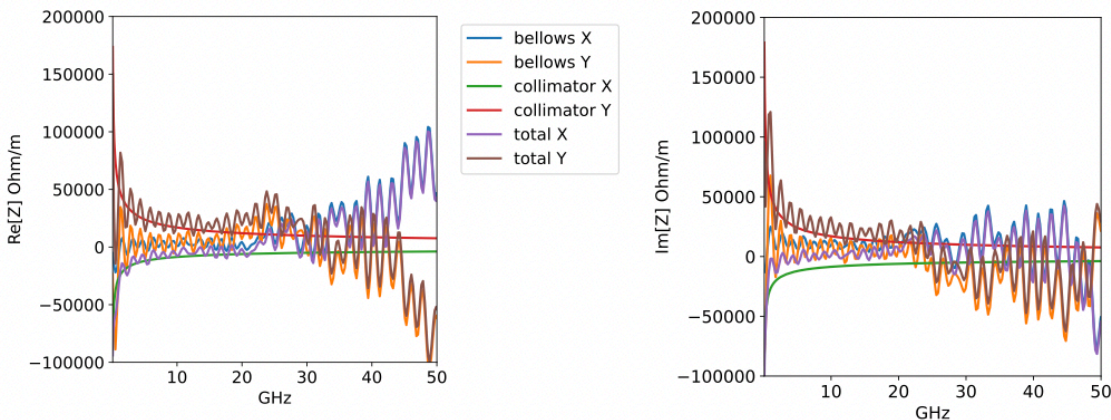


Figure 2.34: Real and imaginary part of the total quadrupolar transverse impedance.

As a first check, we have evaluated the wake potential of a 5 mm Gaussian bunch for a example model. Such a long bunch allows to use CST, even if we cannot use it as a pseudo–Green function. For what concerns, the geometrical impedance of the collimators has not yet been evaluated. In fact, because the beam is very short compared to the model, the number of mesh cells becomes too high, and the computation of the simulation is very difficult to perform. Therefore, we need to find a possible way to overcome the problem. For example, a possible solution could be the use of ECHO3D instead of CST. In this way, it is possible to drastically reduce the number of mesh cells. In Fig. 2.35 shows how the simulation results obtained by ECHO3D and CST are in good agreement.

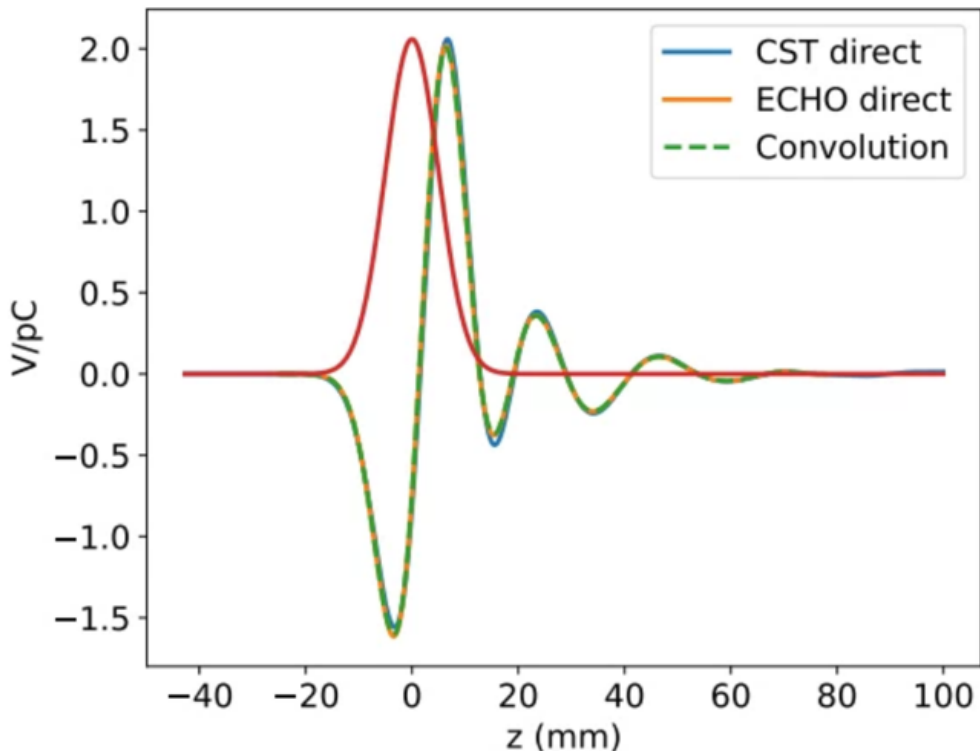


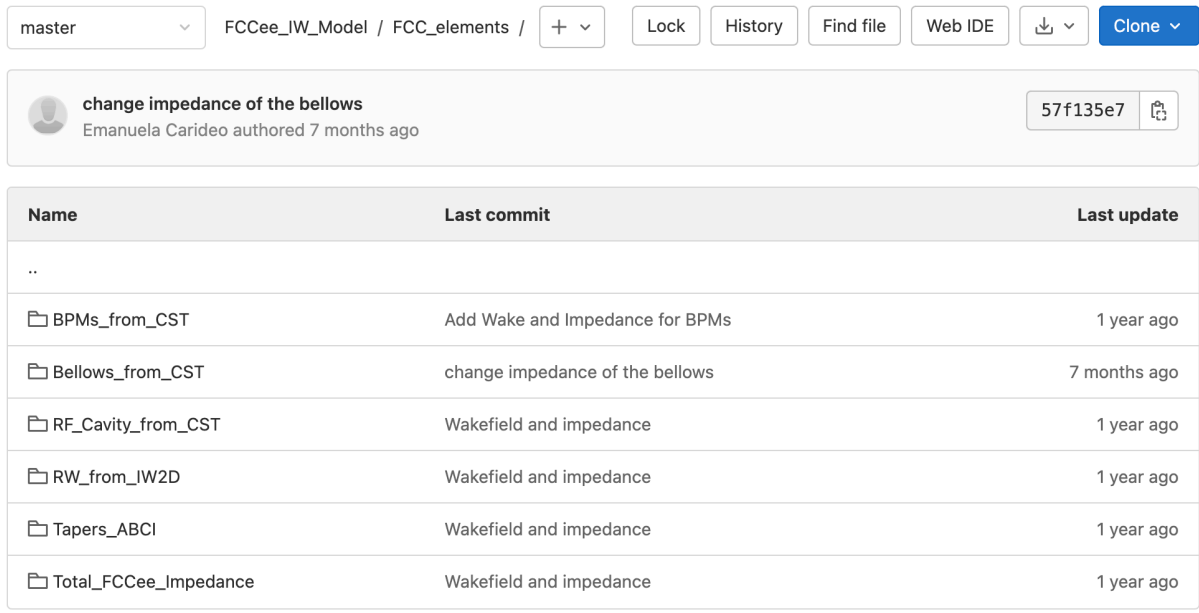
Figure 2.35: Geometric longitudinal wake potential of a 5 mm Gaussian bunch from ECHO3D and CST [5].

The code ECHO3D, which seems a good alternative so far, calculates in the time domain the electromagnetic fields generated by an electron bunch passing through an arbitrary three-dimensional chamber. The bunch form is a Gaussian bunch, and the interesting aspect of this code is that the code works with the moving mesh window in order to speed up the simulations.

2.6 FCC Impedance Repository

In order to keep track of all the updates related to the impedance model and to the parameter list, a repository has been created. The repository is a collection of files and folders related to a definite project. It is also a good way to exchange information within a team and can improve collaboration to achieve the final product. A Git repository is incredibly useful because it allows developers to maintain a single view of a project’s code base, backup the entire history of a project, easily view older versions of the entire codebase or individual files, debug code, search for a particular change

author, and much more. In [47] it is explained how to create and use a repository. Fig. 2.36 is an example of what it is possible to find on the impedance repository page for the FCC-ee. All the folders contain impedance and wake that we have found and the models used for our analysis. The folder with the total impedance combines all the impedances and wakes that we have evaluated so far. In the last column, changes are tracked with version control. It is possible to find the online page in [6].



The screenshot shows a GitHub-style interface for a repository. At the top, there is a dropdown menu set to 'master', a path 'FCCee_IW_Model / FCC_elements /', and various buttons for 'Lock', 'History', 'Find file', 'Web IDE', and 'Clone'. Below this is a commit history box containing one entry: 'change impedance of the bellows' by Emanuela Carideo, authored 7 months ago, with a commit hash '57f135e7' and a copy icon. The main table lists files and their details:

Name	Last commit	Last update
..		
└ BPMs_from_CST	Add Wake and Impedance for BPMs	1 year ago
└ Bellows_from_CST	change impedance of the bellows	7 months ago
└ RF_Cavity_from_CST	Wakefield and impedance	1 year ago
└ RW_from_IW2D	Wakefield and impedance	1 year ago
└ Tapers_ABCI	Wakefield and impedance	1 year ago
└ Total_FCCee_Impedance	Wakefield and impedance	1 year ago

Figure 2.36: Online FCC-ee repository page [6].

Chapter 3

Collective effects: Longitudinal plane

This chapter will be dedicated to the analysis of the effects on the longitudinal dynamics, such as microwave instabilities. They will be examined under different conditions and with the new machine upgrade. At the end of the chapter, the interplay between beam-beam and longitudinal impedance will be introduced and studied.

3.1 Microwave instability

Above a given intensity threshold, the spread of energy starts to increase in what is known as the microwave instability regime, characterized by a turbulent behavior of the longitudinal phase space, as shown in Fig. 3.1, where the distribution has been obtained at different phases of the synchrotron oscillations with the machine parameters of Table 2.1, a bunch intensity of 22×10^{10} , and the wake discussed in the previous chapter.

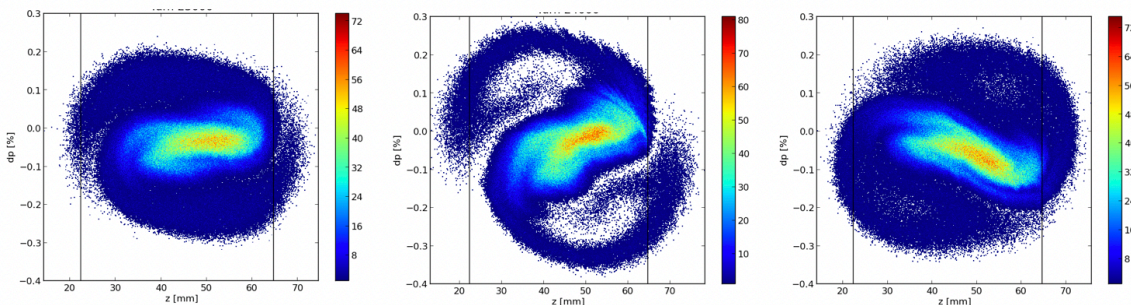


Figure 3.1: Longitudinal phase space at different phases of the synchrotron oscillations with the machine parameters of Table 2.1, a bunch population of 22×10^{10} .

The microwave instability does not produce a bunch loss, but can increase the longitudinal emittance and generate possible bunch internal oscillations that could not be compensated by a feedback system. For the evaluations of the microwave instability threshold, some scaling criteria can be used; however, we have performed a series of simulations by using PyHEADTAIL.

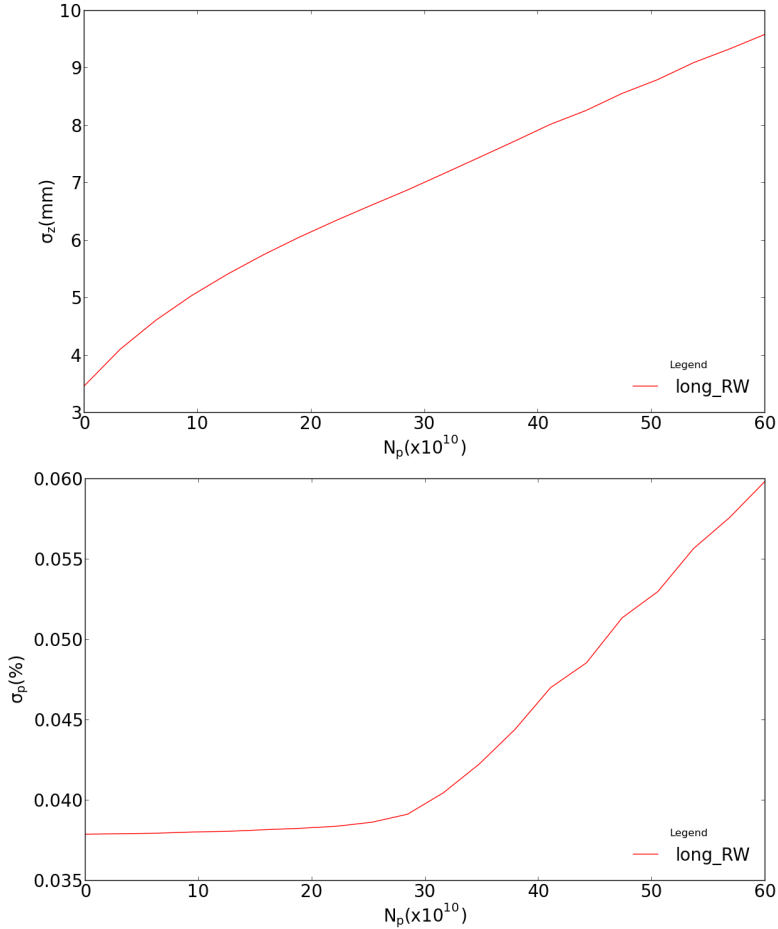


Figure 3.2: RMS bunch length in units of mm (left) and RMS energy spread in % (right), as a function of bunch population in units of 10^{10} , considering only the longitudinal RW and for the parameters of Table 2.1.

Fig. 3.2 shows the obtained bunch length and energy spread that includes only the RW contribution; instead, Fig. 3.3 shows the bunch length and energy spread for the components evaluated so far, with the parameters of Table 2.1. In this case, without collision and with a nominal bunch length of 3.5 mm, we have an energy spread of 0.038%. With a bunch length of 12.1 due to beamstrahlung in collision, the energy spread is 0.132%. Since the nominal intensity is 17×10^{10} , without collision we are in the MW instability regime, the bunch length increases by a factor of about 2.4 with respect to the nominal one, and the energy spread increases by a factor of about 1.6. Moreover, we have an increase of bunch length but also a strong bunch distortion from the original Gaussian one, as shown in Fig. 3.4. On the other hand, we can also see that the effect of the wakefield is much weaker with the inclusion of beamstrahlung.

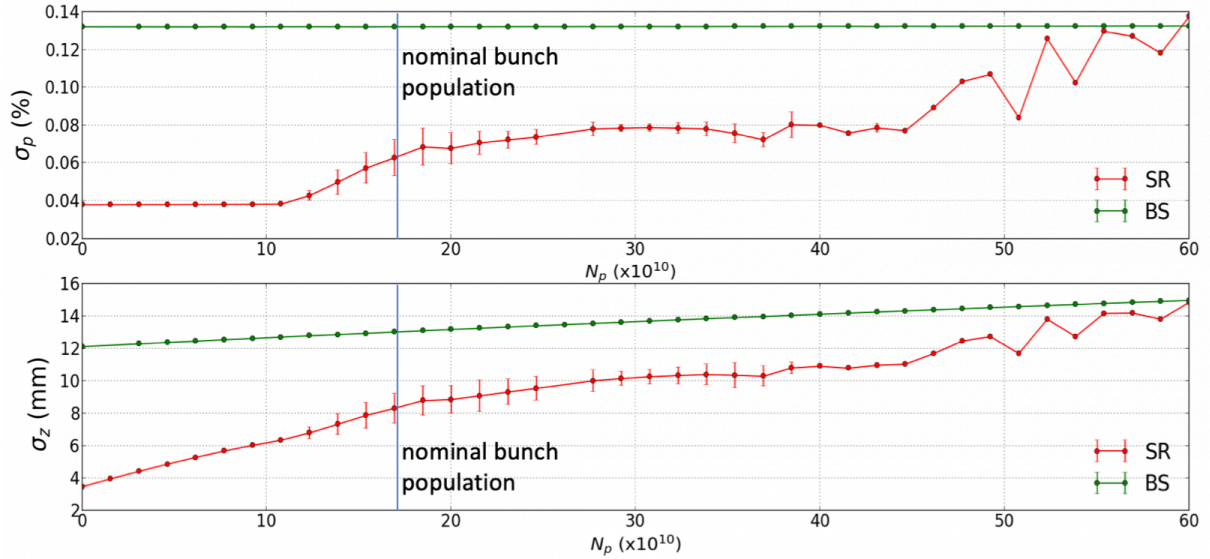


Figure 3.3: Microwave instabilities analysis, RMS bunch length (bottom) and RMS energy spread (top), for the parameters of table 2.1, as a function of bunch population in the case without (red curve) and with (green curve) beamstrahlung effect, which is considered here independent of beam intensity.

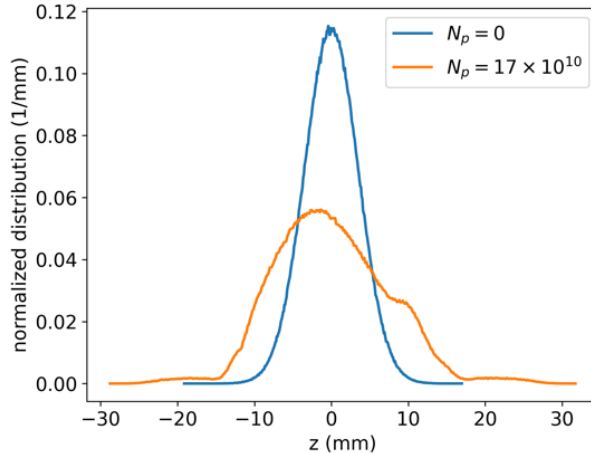


Figure 3.4: Bunch shape distortion at nominal intensity in the single operational mode.

3.1.1 New parameters for the longitudinal dynamics analysis

The same analysis has been performed considering the updated parameter list in addition to the investigated devices, and the results are shown in Fig.3.5. With this updated list, the nominal intensity has been increased from 17×10^{10} to 25×10^{10} particles per bunch.

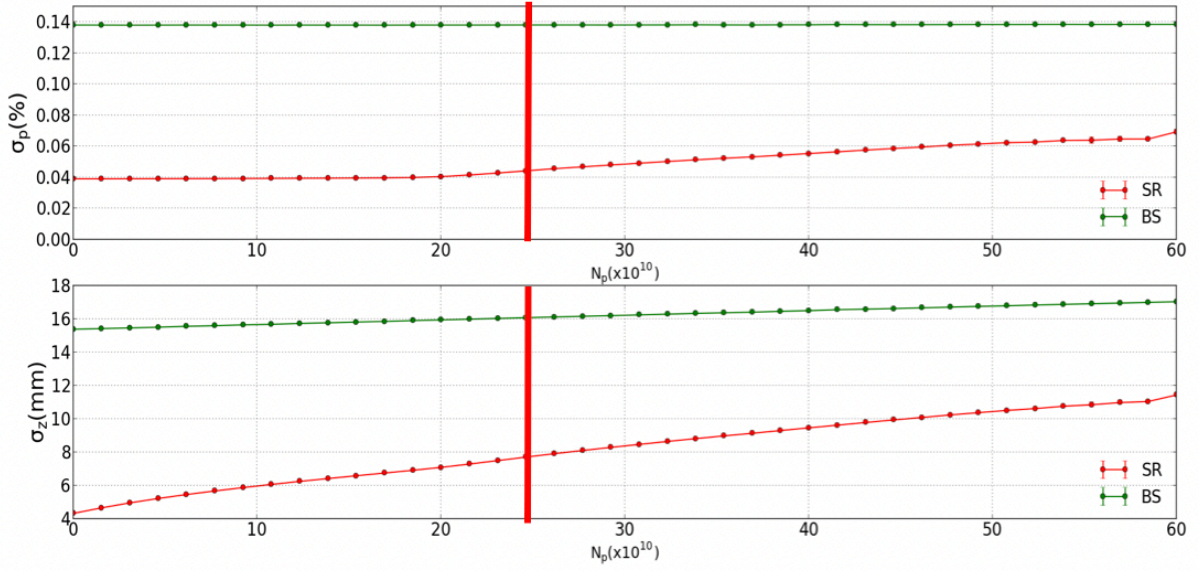


Figure 3.5: RMS bunch length (bottom) and RMS energy spread (top) for the new parameters of Table 1.2, as a function of the bunch population in the case with (BS) and without (SR) beamstrahlung, which is considered here independent of beam intensity.

In both plots we can observe an increase of bunch length and a very weak MW instability for the single beam operation, instead in collision the energy spread remains constant, and the beam length is slightly modified. At first sight, we can say that beamstrahlung helps to mitigate the MW instability, but beamstrahlung also depends on the bunch intensity. Moreover, by studying the beam-beam, we have obtained that the longitudinal impedance has a strong influence on beamstrahlung. In fact, in this analysis, we considered the beamstrahlung and the collective effects due to the wakefields independently of each other. This aspect has to be investigated with the study of beam-beam interactions. The additional contribution of the transverse impedance to the bunch length and energy spread is shown in Fig.3.6. In the plots, we can distinguish 3 different cases: the red line considers only the transverse impedance, the green line is the case if we are considering just the longitudinal impedance, and the blue line takes into account both the transverse and longitudinal RW impedances. As we can see from these plots, the transverse impedance does not give significant changes in this analysis for the longitudinal dynamics, in contrast to what we will see about the longitudinal impedance for the transverse dynamics.

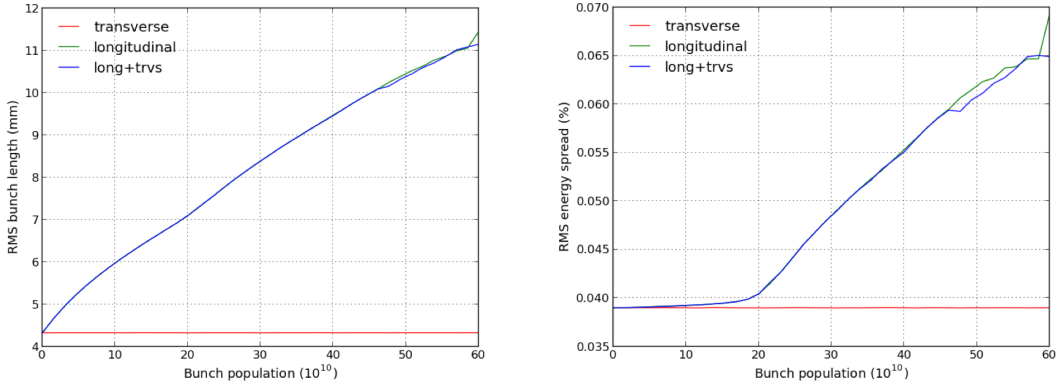


Figure 3.6: Bunch length (left) and RMS energy spread (right) as a function of bunch population in the 3 different cases to understand the influence of the transverse impedance on the longitudinal dynamics.

3.2 Interplay between beam-beam and longitudinal impedance

In storage rings, the beam-beam interaction has been studied since 1960. In particular, these studies were focused in order to improve the collider performance, increasing the luminosity. In order to increase the luminosity, the future machines in collision should have high intensity bunches with very small transverse dimensions. On the other hand, in future electron-positron supercolliders, such as FCC-ee, high luminosity will be achieved with a collision of intense multibunch beams and by exploiting the crab waist collision scheme with a large Piwinski angle [48]. The large Piwinski angle, shown in Fig. 3.7, allows squeezing the vertical beta function β_y at the interaction point and also helps to suppress the vertical synchro-betatron resonances [49].

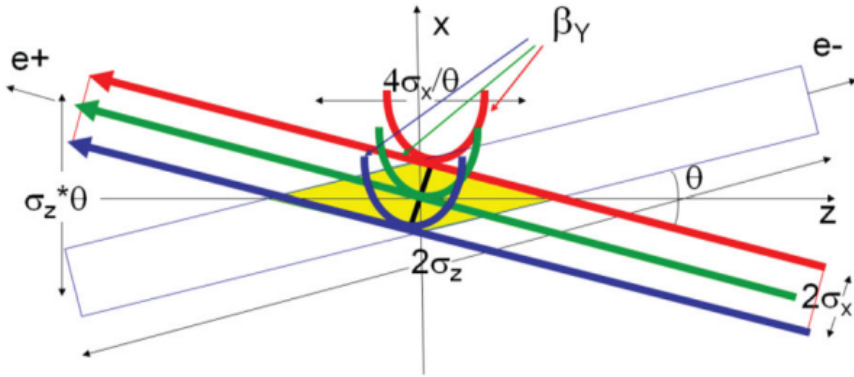


Figure 3.7: Collision with large Piwinski angle [7].

The Piwinski angle, which relates the geometric collision angle and the ratio of the longitudinal and transverse beam sizes, is defined as:

$$\Phi = \frac{\sigma_z}{\sigma_x} \tan\left(\frac{\theta}{2}\right) \quad (3.1)$$

where σ_x is the horizontal rms size at the interaction point, σ_z is the rms bunch length and θ is the crossing angle. Unlike the past generation of colliders, both luminosity and beam-beam tune shift depend on the bunch length, and these characteristic parameter appears in the luminosity

formula. Fig. 3.7 shows that the collision area becomes small for a large Piwinski angle, and the beams can be focused on that small area without incurring the hourglass effect [50]. After this consideration, β_y , the vertical beta function, can be made much smaller than the bunch length σ_z . At the end, the dedicated sextupoles help to eliminate the beam-beam resonances resulting for the vertical motion modulation due to the horizontal betatron oscillations. Since the beam sizes get so small, the beamstrahlung becomes important for the collider performance. Indeed, during the collision for the FCC-ee several new effects become important, such as beamstrahlung [51], coherent X-Z instability [52, 53], and 3D flip-flop [54]. For all of these effects, the longitudinal beam dynamics plays an essential role, and in particular, in this section, we will concentrate on the X-Z instability. It is characterized by coherent horizontal bunch oscillations along the bunch length and respective horizontal emittance growth. In [49] the interplay between beam-beam interaction, beamstrahlung and longitudinal beam coupling impedance has been discussed. Their combination may affect both the X-Z instability and the beam parameters in the stable betatron tune areas. Due to the synchrotron frequency spread induced by the impedance, the horizontal beam blow-up becomes somewhat weaker. It has also been observed that the longitudinal microwave instability is suppressed in collisions [7]. Moreover, in the stable tune areas, free of the coherent resonances, the bunch becomes longer and the energy spread reduces. Additionally, the luminosity and the beam-beam tune shifts strongly depend on the longitudinal bunch length according to:

$$L \propto \frac{N\xi_y}{\beta_y^*}, \quad \xi_y \propto \frac{N\sqrt{\beta_y^*/\epsilon_y}}{\sigma_z\theta}, \quad \xi_x \propto \frac{N}{(\sigma_z\theta)^2}, \quad (3.2)$$

where L is the luminosity, N is the bunch population, $\xi_{x/y}$ the betatron tune shifts due to the beam-beam effect, β^* the beta function at the interaction point, and ϵ_y the vertical beam emittance. So in order to increase the luminosity, future machines should collide high intensity bunches with very small transverse dimensions. In collision, the coherent horizontal-longitudinal (X-Z) instability emerges as the most critical phenomenon to achieve the design collider performance. It is induced by a beam-beam interaction with a large Piwinski angle and, different from the normal impedance induced by collective instability, it is excited by a very local "wake-force" (horizontal beam-beam force). This kind of instability is different from the usual incoherent synchro-betatron resonances. The problem of this instability is that it limits the available tuning areas where the design luminosity can be achieved. On the other hand, the coherent synchro-betatron resonances are separated by the synchrotron tune while the strength of the resonances is proportional to the horizontal tunes shift. Since both values depend on the bunch length, one can expect that the longitudinal impedance can play an important role in the developing of the instability.

With the simulation code IBB [49], the study of the interplay between beam-beam interaction, beamstrahlung, and longitudinal collective effects has been performed. Unlike the tracking codes discussed in the previous chapter, IBB uses as input the longitudinal coupling impedance shown in Fig.2.32. The wake potential is evaluated by the inverse Fourier transform of the product of the impedance and the bunch spectrum. The bunch is represented by macro-particles and sliced in the longitudinal direction, in order to take in account the hourglass effect, the geometric luminosity reduction and the transverse beam-beam blow-up that depends on the finite bunch length. In Fig. 3.8 we have also verified that the collective effects of FCC-ee are simulated correctly by comparing

bunch length and energy spread versus the bunch population between IBB and PyHEADTAIL. The agreement between the two codes is excellent.

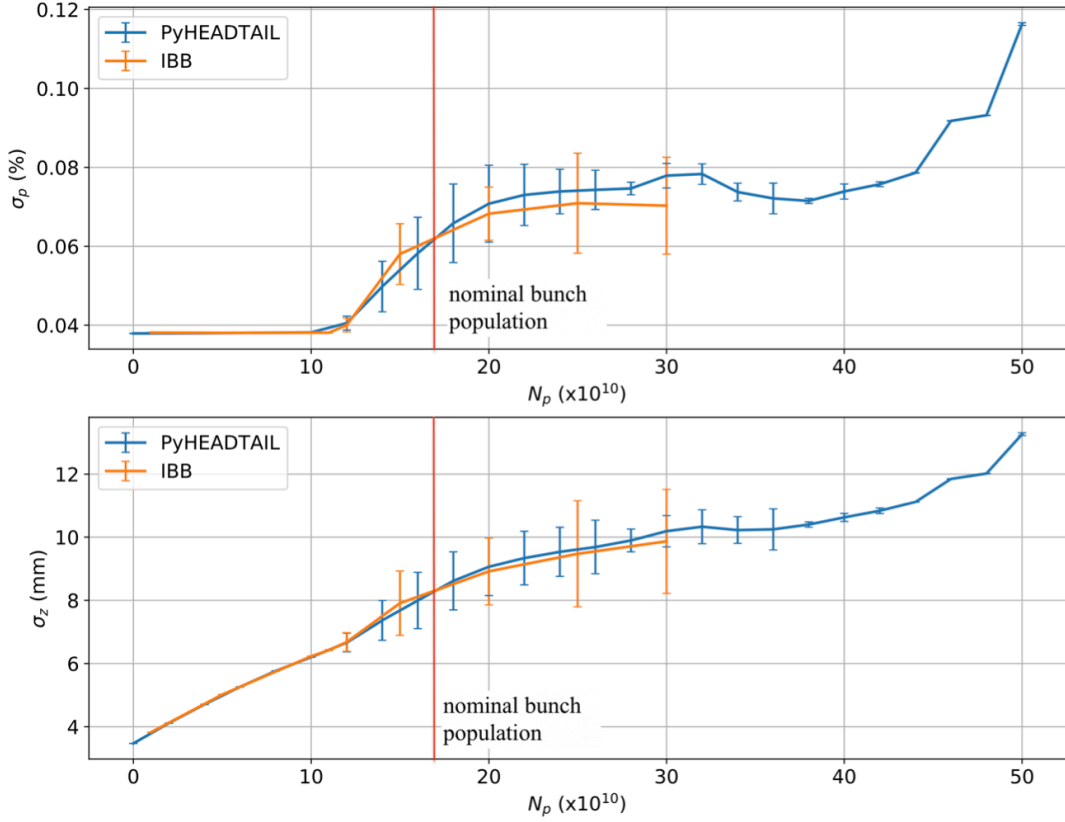


Figure 3.8: Comparison between IBB, orange line, and PyHEADTAIL, blue line, of energy spread σ_p (top) and bunch length σ_z (bottom) as a function of the bunch population without collision[3].

During this analysis the FCC-ee had still two interaction points, so in the IBB code only half of the machine is simulated, being symmetric in the other half. The study of the X-Z instability is performed by evaluating the horizontal beam dimension at different intensities and horizontal tunes. A blow-up of the horizontal beam size is a manifestation of this instability, and the value of beam size is related to its strength.

Fig.3.9 shows the results of the beam-beam simulations without the longitudinal coupling impedance at different horizontal tunes and bunch intensities. The stable area is represented by the white region, and the colour map close to the figure represents the increase of the horizontal beam size σ_x with respect to the nominal value. Through the figure, it is possible to see that without the collective effects there is a stable area in the middle at any simulated intensity up to a bunch population of 18×10^{10} with half horizontal betatron tune $v_x/2$ between 0.566 and 0.571.

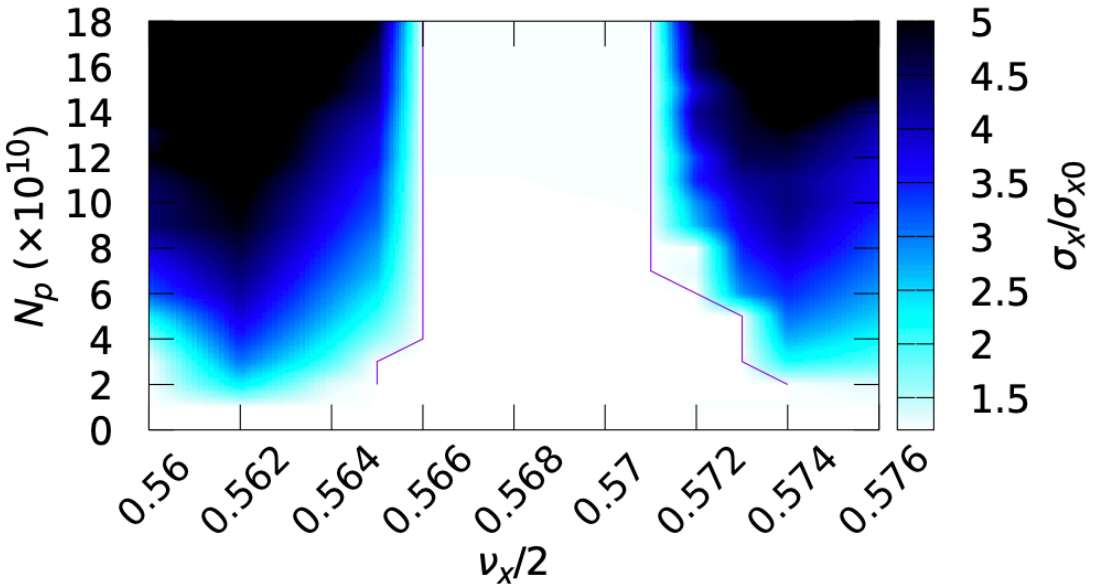


Figure 3.9: Blow-up of the horizontal beam size σ_x/σ_{x0} as a function of the bunch population and of the horizontal tune scan without impedance [3].

When we include the impedance model, Fig.3.10 shows how this stable region is reduced. In fact, we have a narrower stable region at the nominal intensity.

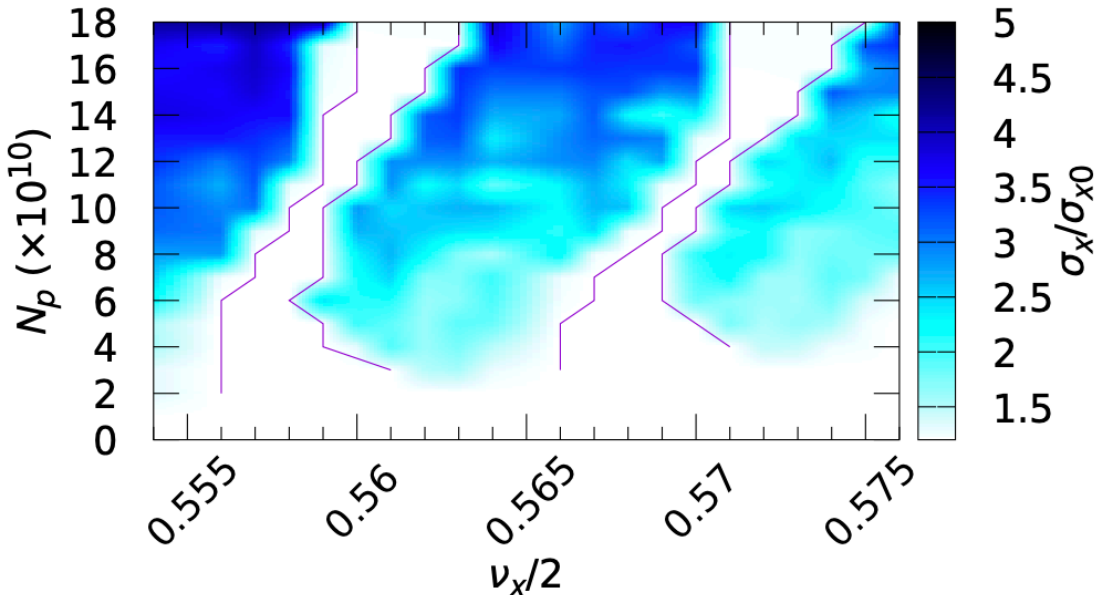


Figure 3.10: Blow-up of the horizontal beam size σ_x/σ_{x0} as a function of the bunch population and of the horizontal tune scan, if including the impedance [3].

Moreover, during the beam filling from scratch we cannot use a fixed betatron tune, but the quadrupole magnets should be foreseen as a function of the bunch population in order to change the betatron tune, which, at any intensity, guarantees a stability of the horizontal beam size, represented by white regions.

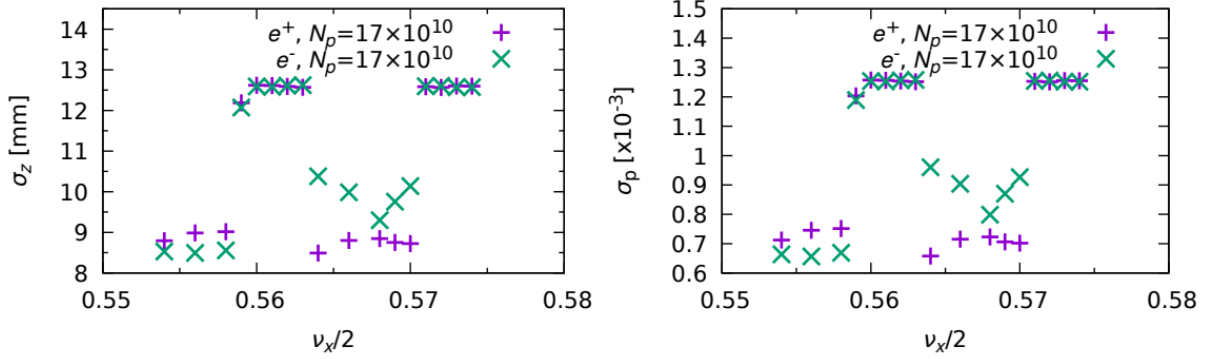


Figure 3.11: Bunch length (left) and energy spread (right) at the nominal bunch population as a function of the horizontal betatron tune [3].

Interesting is the analysis Fig.3.11 which demonstrates that in the stable region, the method of including the beamstrahlung as an independent effect is valid, and the microwave instability is suppressed. On the other hands, at the nominal bunch intensity of 17×10^{11} if we are in the small stable region with $v_x/2$ in the range of 0.56 and 0.563, the bunch length and energy spread are very close to the parameters of Table 2.1 with the inclusion of the beamstrahlung (12.6 mm and 0.126%, respectively as shown Fig.3.11). We can definitely conclude that there is a strong interplay of the longitudinal coupling impedance with the beam-beam effect that reduces the stable regions free from the X-Z instability. In fact, at the nominal bunch intensity the beamstrahlung increases the longitudinal emittance in order to suppress the MW, if there is no blow-up of the horizontal size. Since the FCC–ee design is still in progress, of course the machine impedance evaluated so far will increase due to the contribution of other devices and the already small stable regions could become even narrower or disappear[39]. Moreover, we have the difficulty, during the beam filling, to reach the nominal bunch intensity due to the necessary variation of the horizontal tune. For this reason, mitigation methods for the X-Z instability have been investigated. In the last chapter of this thesis, we will consider five different possibilities.

Chapter 4

Collective effects: Transverse plane

This is the chapter dedicated to the study of the transverse dynamics and the TMCI threshold. A comparison between Delphi and PyHT will be showed and will be introduced the longitudinal impedance in the analysis of the transverse dynamics, and we will see how it can influence the TMCI threshold. At the end of the chapter, the new simulations considering a machine upgrade will be presented.

4.1 PyHEADTAIL and Delphi

In the transverse plane, when increasing the bunch intensity, due to the wakefield, there is a shift of the coherent betatron frequencies of the intra–bunch modes. The Transverse Mode Coupling Instability (TMCI) occurs when the frequencies of two neighbouring coherent oscillation modes, also called head-tail modes, merge together [1]. The transverse mode coupling instability can affect high intensity single bunches in circular accelerators, and it is used together with the general properties of coupling impedances to show how single bunches become unstable when head-tail modes couple together. It is also named strong head-tail instability, as during the first half of the synchrotron period, the electromagnetic field induced by the particles at the head of the bunch perturbs the particles at the tail of the bunch. During the second half of the synchrotron period, the same happens, but the particles have swapped their positions. If we are below a certain bunch intensity, the disturbance is not strong enough and the perturbations do not accumulate. However, above a certain intensity threshold, the perturbations accumulate and the particle’s motion grows exponentially. Unlike the microwave instability, above the TMCI threshold the bunch is lost and this makes the TMCI very dangerous for the beam. The analytic transverse mode coupling instability threshold is given by the well known Sacherer formula [55, 56]:

$$N_{th} = \frac{4\pi \frac{E_0}{e} \tau_b Q_s}{e \beta_{av} \text{Im} [Z_m^{\text{eff}}]} \quad (4.1)$$

where the azimuthal mode number $m=0$ is considered, $\tau_b = \frac{4\sigma_z}{c}$ is the full bunch length in s, $\beta_{av} = \frac{C}{2\pi Q_\beta}$ is the average beta function of the machine. The equation gives the maximum allowed effective transverse impedance to avoid the instability. In general, Z_m^{eff} is the effective transverse impedance[57]:

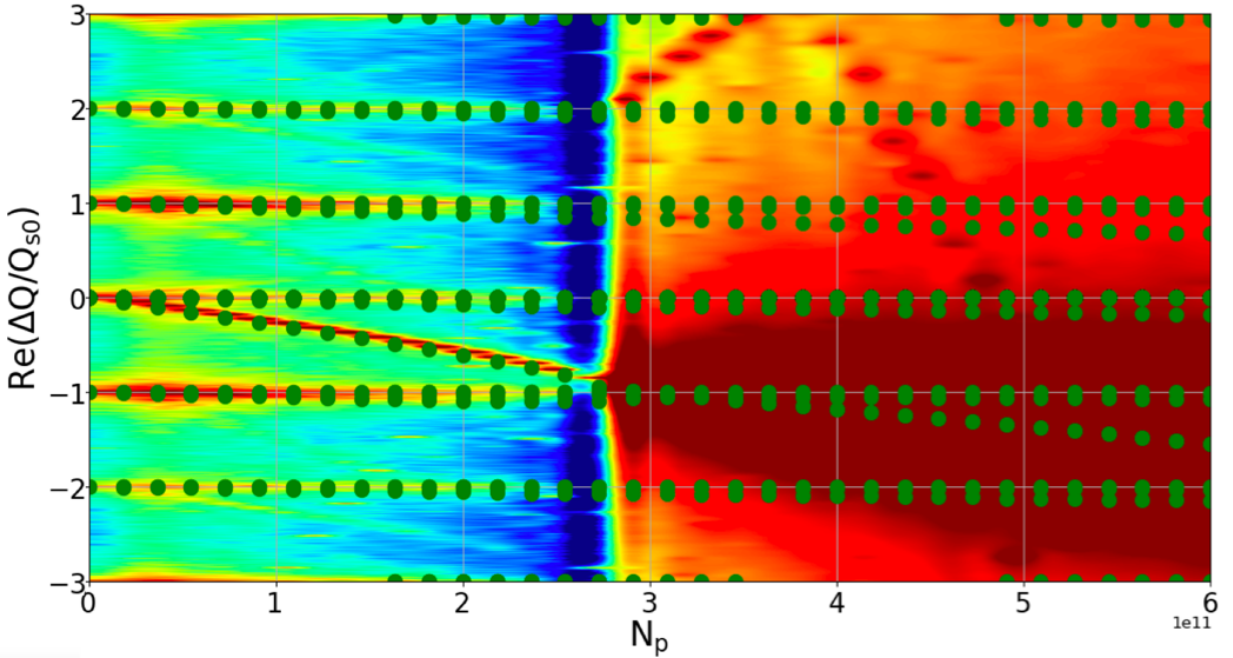


Figure 4.1: The real part of the frequency shift of the first coherent oscillation modes as a function of the bunch population corresponds to non-colliding bunches, without beamstrahlung, by considering only the RW impedance produced by a NEG film with 150 nm thickness given by IW2D. The green dots represent the Delphi results, instead the colours come from PyHEADTAIL simulations which are proportional to the amplitude of the frequency spectrum of the various moments of the distribution: red corresponds to the largest amplitude, blue to the lack of signal.

$$Z_m^{\text{eff}} = \frac{\sum_{p=-\infty}^{+\infty} Z_{\perp}(\omega_p) h_m(\omega_p - \omega_{\xi})}{\sum_{p=-\infty}^{+\infty} h_m(\omega_p - \omega_{\xi})} \quad (4.2)$$

Z_{\perp} is the transverse impedance, evaluated at the frequency ω_p and $h_m(\omega)$ is the bunch power spectrum of the azimuthal mode m , that, for a Gaussian bunch, is

$$h_m(\omega) = \left(\frac{\omega \sigma_z}{c}\right)^{2|m|} e^{-\frac{\omega^2 \sigma_z^2}{c^2}} \quad (4.3)$$

and the bunch spectrum is discrete evaluated at lines $\omega_p - \omega_{\xi}$ where

$$\omega_{\xi} = \omega_0 \frac{\xi}{\eta}. \quad (4.4)$$

is the chromatic angular frequency which depends on the revolution frequency ω_0 , the chromaticity ξ and the slippage factor η , and

$$\omega_p = (p + \Delta Q)\omega_0 + m\omega_s \quad (4.5)$$

where p is an integer, ΔQ is the fractional part of the betatron tune and ω_s is the synchrotron frequency.

The TMCI can clearly be observed in electron machines because of the short length of the bunches [58]. In order to study the transverse coherent frequency shift and the TMCI, we used PyHT by evaluating the Fourier transformation of some momenta of the bunch distribution [59]. Addition-

ally, we checked the results of the tracking code simulations with the analytic Vlasov solver Delphi [60], which solves the Sacherer integral equation [31] by using a decomposition of the longitudinal distribution in coherent oscillation modes, and it finds the frequency of these modes at different bunch intensities. Following the same idea of the longitudinal plane, also in this case, for PyHEADTAIL, we have used the RW wakefield of a short bunch with a length of 0.4 mm as Green function. Delphi, on the other hand, uses the impedance in frequency domain given directly by IW2D. Both approaches are important for estimating the coherent beam stability limits, and their results are shown, as comparison, in Fig. 4.1, where we reported the real part of the coherent tune shift ΔQ with respect to the betatron tune of the first azimuthal modes, divided by the unperturbed synchrotron tune Q_{s0} , as a function of the bunch population N_p . At low intensity, we observe the coherent frequencies at multiples of the unperturbed synchrotron frequency. When the intensity increases, there is a shift, in particular of the frequency of the 0 mode down to -1. No instability is observed in this case up to a bunch population of $N_p = 2.8 \times 10^{11}$. The green dots represent the Delphi results, which well fit with the PyHEADTAIL simulations, for which the colours are proportional to the amplitude of the frequency spectrum of the various moments of the distribution [59]. Red corresponds to the largest amplitude, blue to the lack of signal. We can conclude that there is an excellent agreement between the two methods up to the instability threshold. For doing this comparison, we used the CDR parameters, but of course the validity of the method is not questioned. These results have been obtained by considering only the transverse RW wakefield.

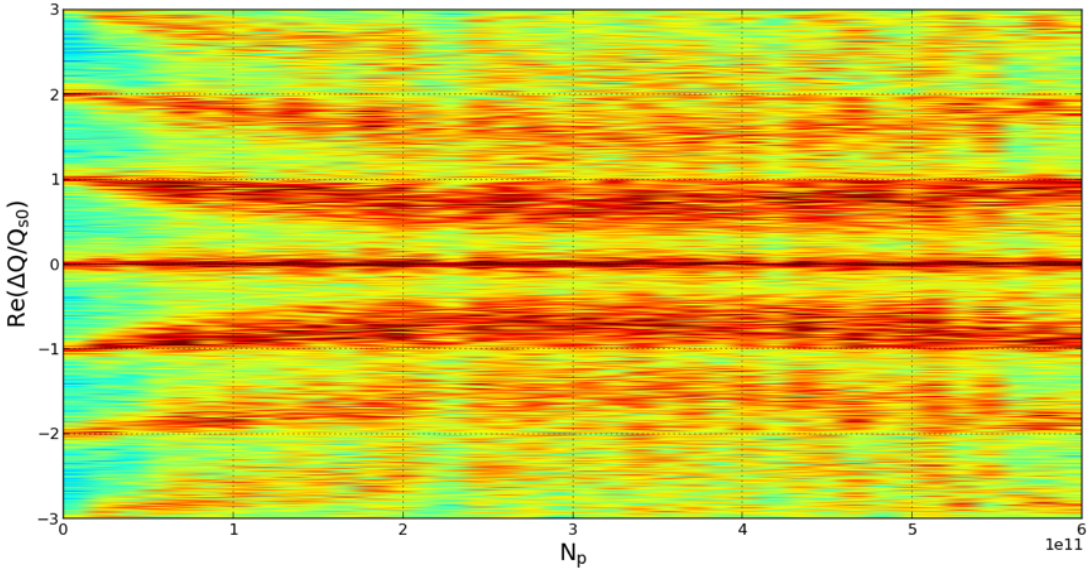


Figure 4.2: Real part of the coherent tune shift as a function of intensity considering the longitudinal resistive wall wakefield and non-colliding bunches, by using PyHEADTAIL.

4.1.1 Longitudinal wakefield in the transverse dynamics

Since the TMCI threshold strongly depends on the bunch length, which, in turn, is affected by the longitudinal dynamics, we have also performed simulations with PyHEADTAIL by taking into account, at the same time, both the longitudinal and transverse RW wakefield. Fig. 4.2 shows the transverse coherent mode analysis considering just the longitudinal RW wakefield. This figure is important because it shows the effect of the longitudinal wakefield which produces a spread in the

transverse coherent oscillation frequencies. In particular, we note that the mode -1 approaches the mode 0. In this case, of course, there is no shift of the mode 0 toward -1 because the transverse wakefield is missing, however, a small shift could decrease the TMCI threshold with respect to Fig. 4.1 which includes only the transverse wake. On the other hand, the longitudinal wake increases the bunch length, thus increasing the TMCI threshold. The combination of these two opposite tendencies has been studied with PyHT by using both the longitudinal and transverse wakefields. We have started by considering first only the updated RW impedance with a NEG coating of 150 nm. The results are shown in Fig.4.3, where we can see that even at low intensities, several frequency lines start to appear for each azimuthal mode. These can be interpreted as the product of different radial modes of the same azimuthal family, and the TMCI threshold is reduced to about $N_p = 1.7 \times 10^{11}$. This reduction of the TMCI threshold is supposed to be produced by the lower coherent synchrotron frequency and by its spread due to the longitudinal wakefield. So we can conclude that the longitudinal wakefield has an important effect not only on the MW instability but also related to the reduction of the TMCI threshold.

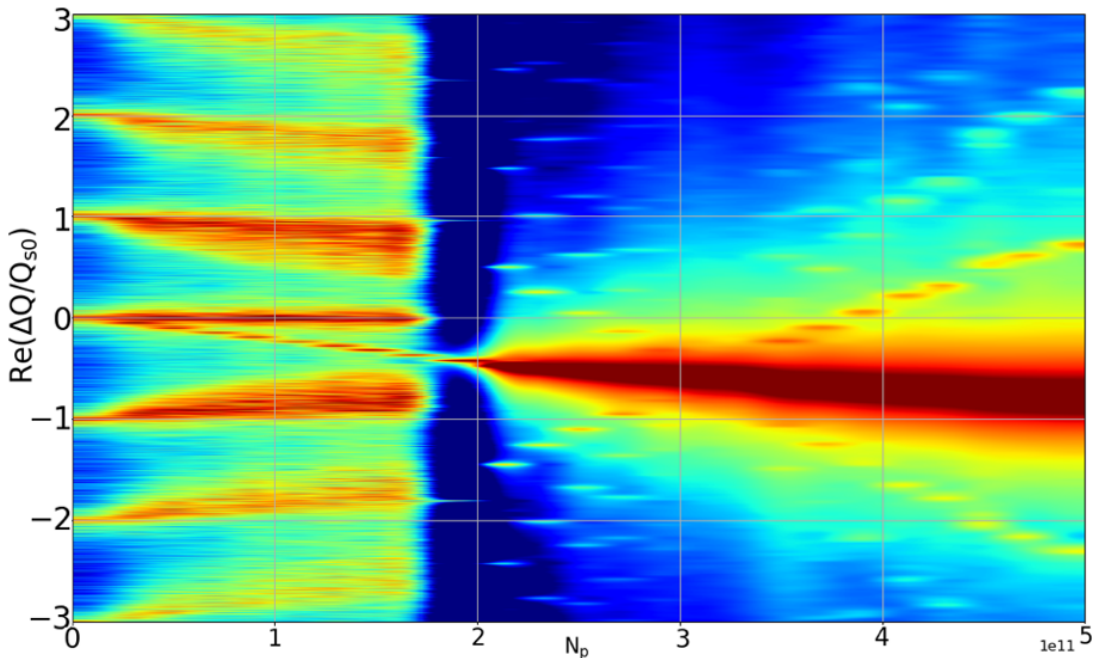


Figure 4.3: Real part of the frequency shift of the first coherent oscillation modes as a function of the bunch population for a non-colliding bunches and by considering both the longitudinal and transverse RW impedance produced by a NEG film with 150 nm thickness, given by IW2D.

If we use, in the analysis, the nominal bunch length of 12.1 mm that includes the beamstrahlung effect, we obtain the result shown in Fig 4.4 and 4.5, without and with the inclusion of the longitudinal wakefield. We observe a TMCI threshold much higher due to the longer bunch length. These results show that the beamstrahlung has a strong interplay with the collective effects produced by wakefields. However, the increase of bunch length and energy spread produced by the beamstrahlung depends on the bunch intensity, while we have considered this quantity constant. Self-consistent simulations cannot be performed with PyHT, which can take into account only single beam effects, and beam-beam simulations including longitudinal and transverse impedances have to be performed [59]. Indeed, another important effect related to TMCI is due to the beam beam

collision of two counterrotating beams that can produce coherent dipole oscillation modes, modifying the stability conditions. In this situation, coherent beam-beam effects and impedance are not independent and their interplay should be taken into account [95]. This subject, deserves future investigations, as well as the mitigation effect due to BS also based on colliding beams. Fig. 4.4 and 4.5 show the TMCI analysis taking into account just the transverse RW under the BS effect and with both longitudinal and transverse wakefield, respectively. Certainly, this is just a preliminary analysis which doesn't include the study of the beam-beam, yet.

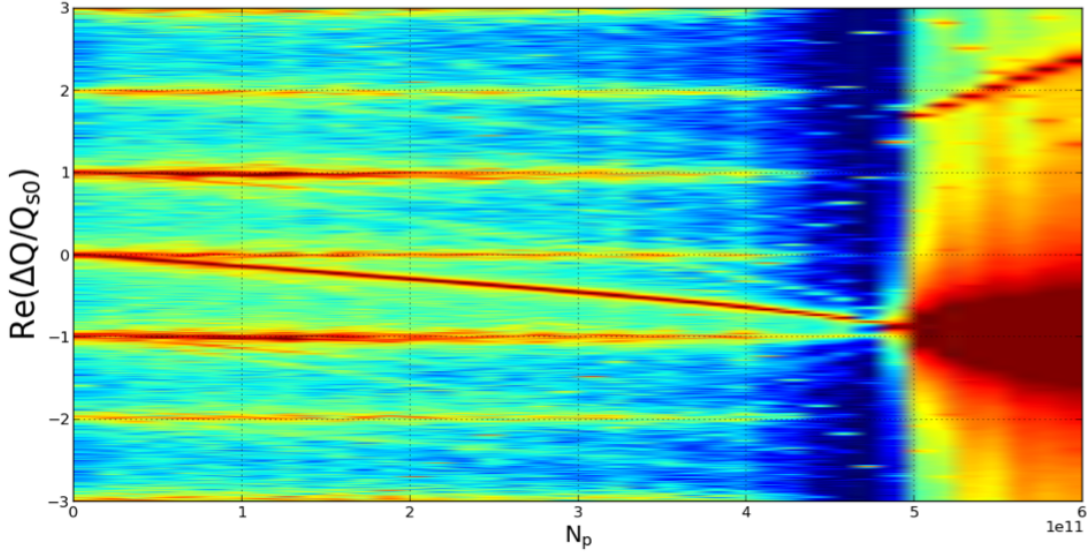


Figure 4.4: Real part of the frequency shift of the first coherent oscillation modes as a function of the bunch population by considering transverse RW and colliding bunches, so with a bunch length of 12.1 mm.

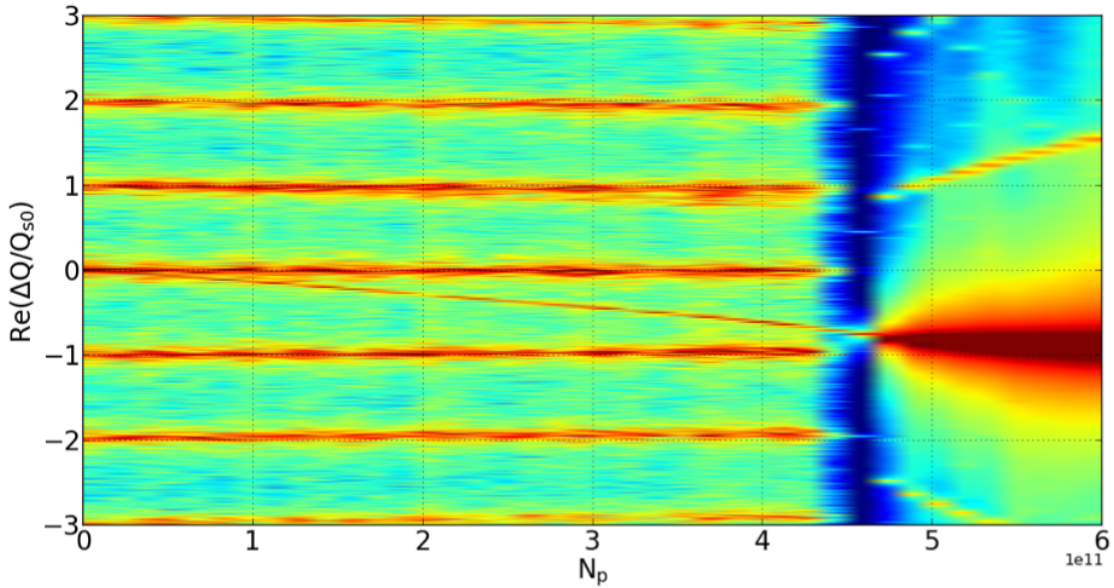


Figure 4.5: Real part of the frequency shift of the first coherent oscillation modes as a function of the bunch population by considering both longitudinal and transverse RW impedance produced by a NEG film with 150 nm thickness and colliding bunches, so with a bunch length of 12.1 mm.

4.1.2 PyHEADTAIL simulations: new devices and parameters

Since the machine parameters have been changed, since the CDR, in Fig.4.6 we show the TMCI threshold with the updated impedance model and the beam parameters of table 1.2. The instability produced by the coupling between the mode -1 and 0 is around 22×10^{10} with a new nominal intensity of 25×10^{10} with respect to the previous one of the 17×10^{10} [1]. The updated optics with a larger momentum compaction factor helps to mitigate collective effects.

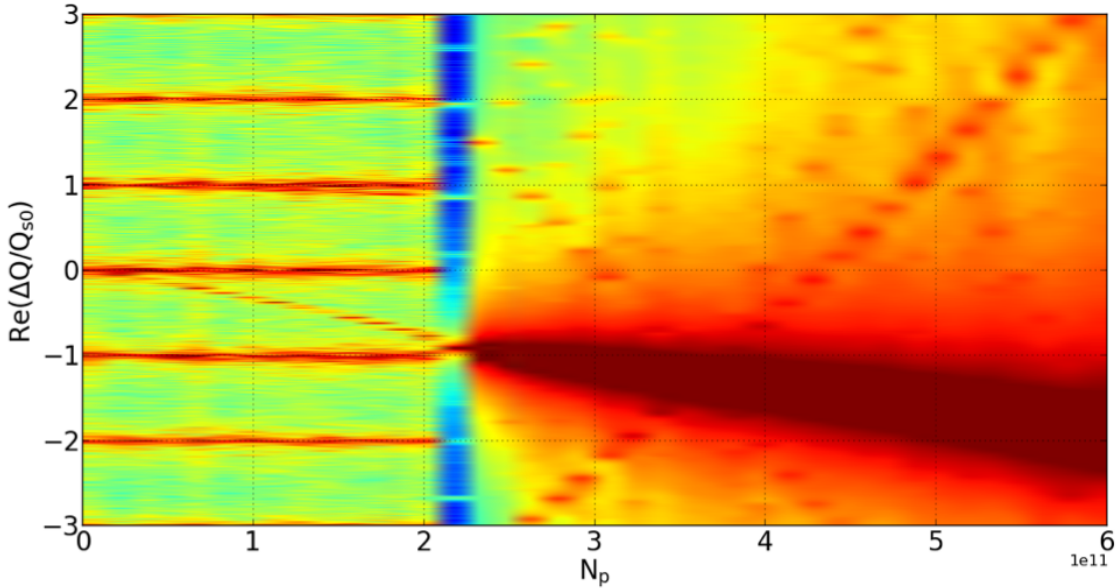


Figure 4.6: Real part of the frequency shift of the first coherent oscillation modes as a function of the bunch population with a nominal bunch length of 4.37 mm, by considering only the transverse wakefield and non-colliding bunches.

If we also include the longitudinal wake, we obtain the result of Fig. 4.7. We can get the same comments as in the previous case; in fact, also in this case we obtained a lower threshold due to the longitudinal wake.

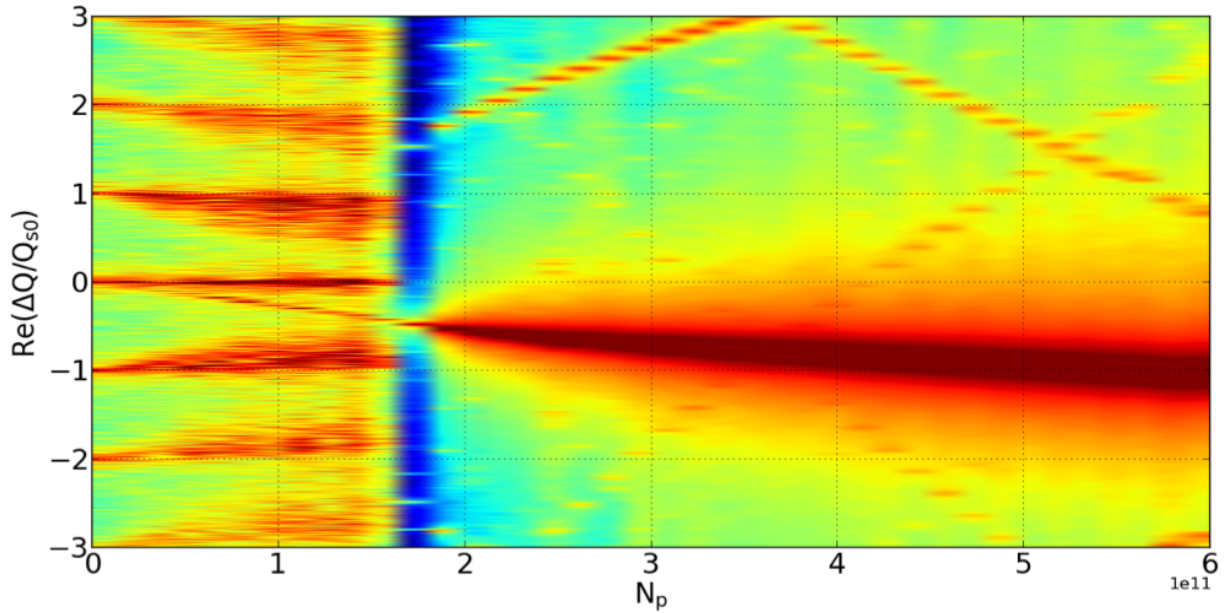


Figure 4.7: Real part of the frequency shift of the first coherent oscillation modes as a function of the bunch population by considering both the transverse and longitudinal wakefields and non-colliding bunches.

Finally, if we consider the nominal bunch length given by the beamstrahlung at nominal intensity, we obtain the results shown in Fig. 4.8.

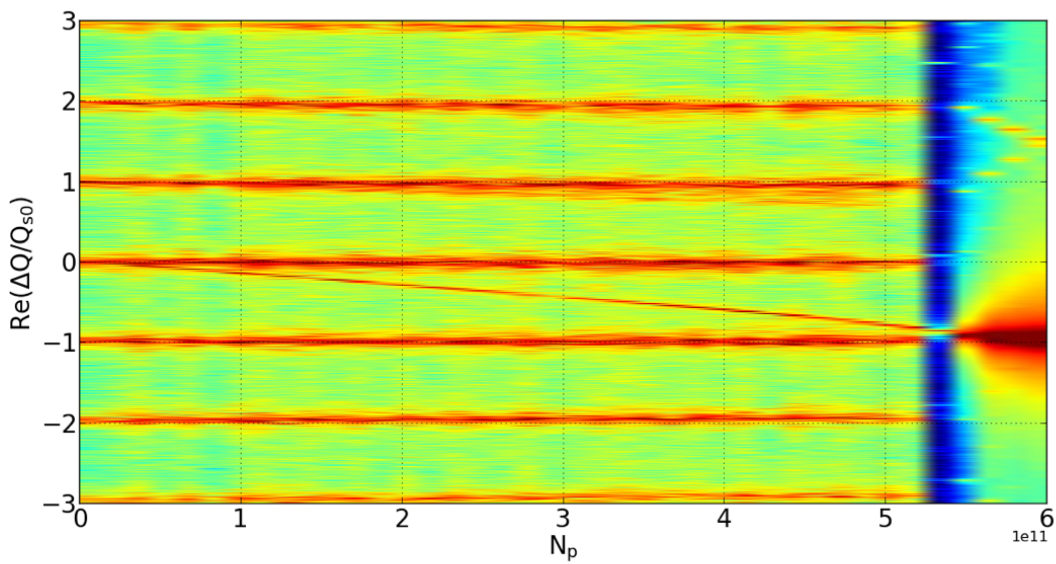


Figure 4.8: TMCI: Longitudinal and transverse wake by considering colliding bunches, so with a nominal bunch length of 14.5 mm (BS)

Chapter 5

Mitigation

The impedance evaluated so far demonstrates how this machine can become critical due to collective effects. In previous chapters, we evaluated longitudinal and transverse instabilities based on the new impedance contributions that gradually have been added, and they suggest that we need to look for diversified mitigation solutions.

5.1 Chromaticity

Until now, simulations have been performed considering zero chromaticity. Numerous studies have demonstrated that increasing the chromaticity helps to increase some instability thresholds [61]. Chromatocity ξ describes the variation of the betatron tune with respect to the particle momentum offset, according to:

$$\frac{\Delta Q_{x0}}{Q_{x0}} = \xi \delta \quad (5.1)$$

where Q_x , the particle tune, is written as $Q_x = Q_{x0} + \xi Q_{x0} \delta$ and the momentum deviation is $\delta = \frac{p-p_0}{p_0}$. The transverse tune Q_{x0} is defined as the number of oscillations per turn and derived from the phase advance:

$$Q_{x0} = \frac{1}{2\pi} \oint \frac{1}{\beta_x(s)} ds \quad (5.2)$$

The spread in betatron tune, introduced by the chromaticity, is expected to help to suppress some transverse instabilities. The head-tail instability, for example, is a chromaticity dependent instability. Another instability which can be harmful for the machine and can be mitigated thanks to the chromaticity is the TMCI. In Fig. 4.7 we showed the TMCI threshold with zero chromaticity.

If we use a value of chromaticity of +5, the threshold is just slightly increased, as shown in Fig.5.1. This confirms the mitigation effect of positive chromaticity. In fact, if we use, just to have an idea about this effect, the unrealistic value of +50, it is possible to completely suppress the TMCI as shown in Fig.5.2. This indicates that large values of chromaticity can be an efficient way to stabilize the instability. On the other hand, a negative value of chromaticity, for example -5 as shown in Fig.5.3, excites the instability of the 0 mode. In this case, we need a feedback system to take the instability under control. However, the feedback is also necessary to suppress the transverse coupled bunch instability due to the real part of the RW impedance at low frequency, and this instability could be very challenging to take under control. This regime needs further investigation.

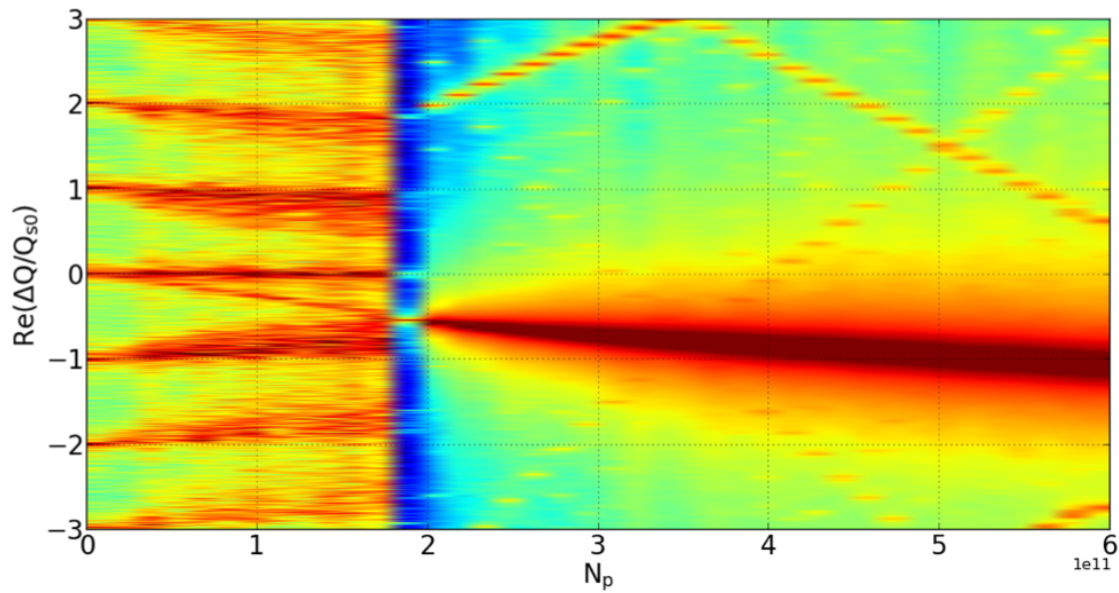


Figure 5.1: Real part of the frequency shift of the first coherent oscillation modes as a function of the bunch population without beamstrahlung, with a value of chromaticity of +5.

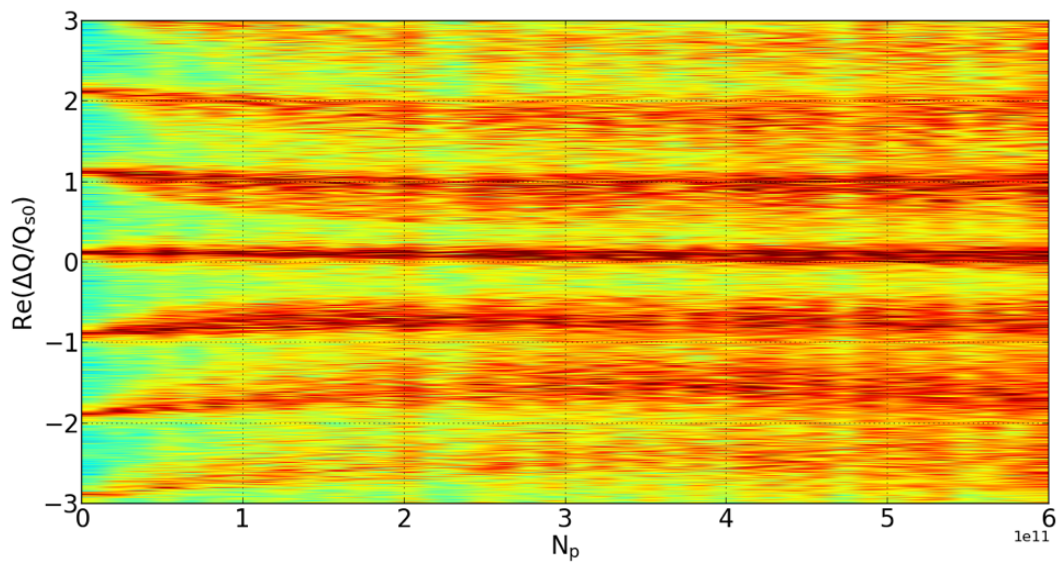


Figure 5.2: Real part of the frequency shift of the first coherent oscillation modes as a function of the bunch population, with a value of Chromaticity of +50.

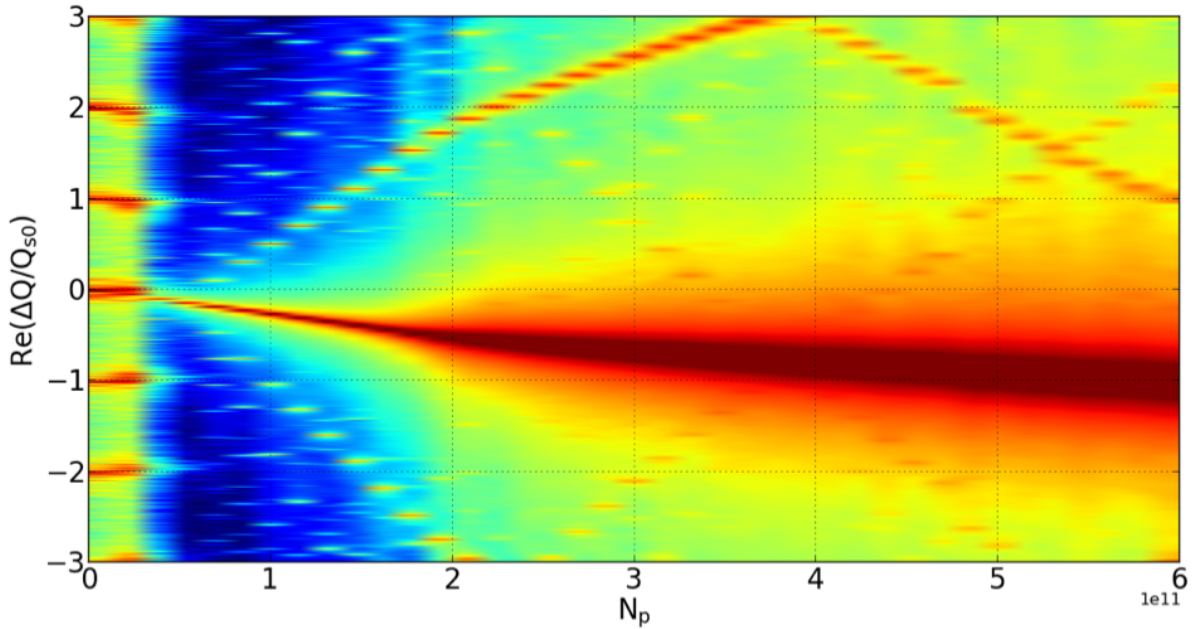


Figure 5.3: Real part of the frequency shift of the first coherent oscillation modes as a function of the bunch population without beamstrahlung, with a value of Chromaticity of -5 .

5.2 Higher momentum compaction

The momentum compaction factor of a storage ring can be obtained by measuring how the beam energy changes with the RF frequency. It is an optics parameter in particular is a ratio between the relative variation in orbit length and the relative momentum deviation with respect to the reference particle. In fact, we can write the momentum compaction factor, α_c , as:

$$\alpha_c = \frac{\Delta L}{L} \times \frac{p}{\Delta p} \quad (5.3)$$

ΔL is the variation of path length with momentum p . Considering ultra-relativistic particles with $v \approx c$, where c is the speed of light, ΔL is directly related to the RF frequency variation, Δf_{RF} :

$$\frac{\Delta L}{L} = -\frac{\Delta f_{RF}}{f_{RF}} \quad (5.4)$$

On the other hand, the momentum p can be approximated to the beam energy E/c :

$$\frac{\Delta p}{p} \simeq \frac{\Delta E}{E} \quad (5.5)$$

so we can obtain:

$$\frac{\Delta E}{E} = -\alpha_c \frac{\Delta f_{RF}}{f_{RF}} \quad (5.6)$$

In order to find a larger stable tune area, as in Fig. 3.10, a possible way is to increase the synchrotron tune v_s keeping the horizontal beam-beam tune shift unchanged. For that goal, in [62] a larger momentum compaction factor has been proposed by reducing the FODO cell lattice from the original $60/60^\circ$ to $45/45^\circ$.

Using a higher momentum compaction factor, we have to operate at higher intensity, but the microwave instability is weaker. Moreover, another advantage is the larger synchrotron tune, which has a beneficial effect on the transverse mode coupling instability threshold and on the energy calibration. Increasing the nominal bunch population, we can reduce the number of bunches per beam, in this way a larger bunch separation will help mitigate the e–cloud effect [63] and ion trapping [64].

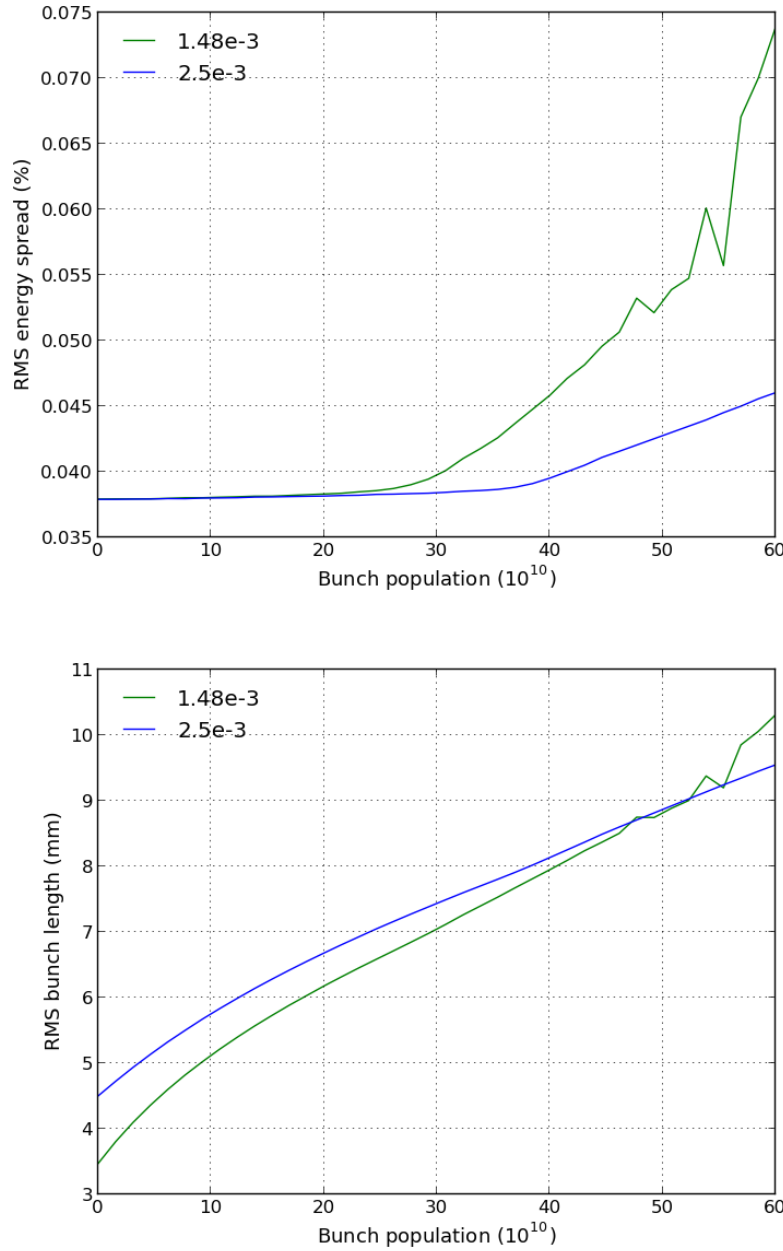


Figure 5.4: RMS Energy spread and bunch length of the longitudinal RW with the parameters of Table 2.1 and considering a NEG of 100 nm, with two different momentum compaction factors: 1.48×10^{-3} and 2.5×10^{-3} .

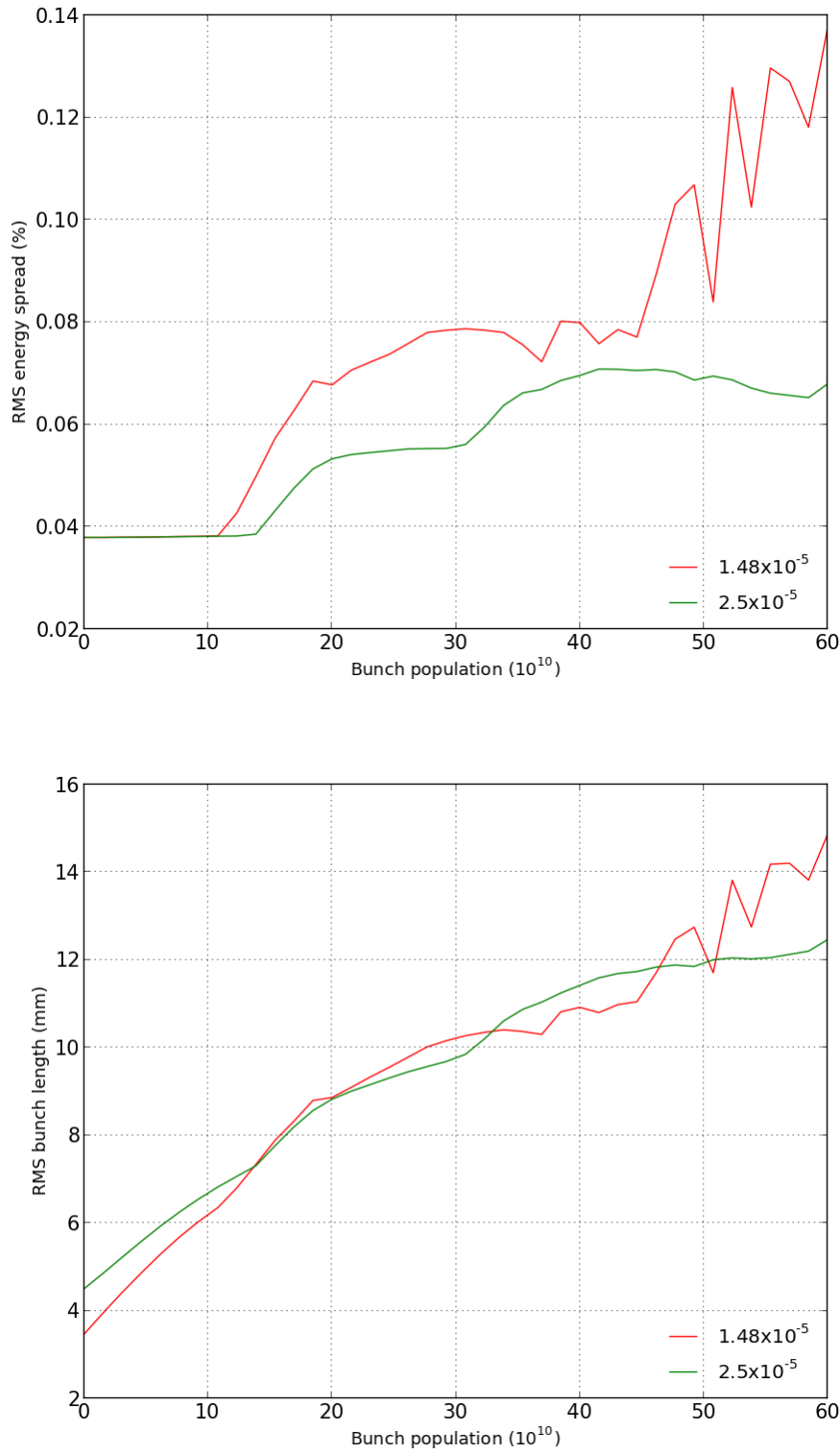


Figure 5.5: Energy spread and bunch length with the updated impedance model and the parameters of 2.1, with two different momentum compaction factors: 1.48×10^{-3} and 2.5×10^{-3} .

In Figs. 5.4 and 5.5 we show the energy spread and bunch length, without the beamstrahlung, due to collective effects for two different momentum compaction values: 1.48×10^{-3} and 2.5×10^{-3} . Fig 5.4 considered only the longitudinal RW contribution, and Fig 5.5 considered the longitudinal

wakefield of the machine components that we have obtained so far. From both figures, we can observe that the microwave instability threshold, with higher momentum compaction factor, is just slightly changed to a bit higher intensity. Additionally, we need a higher bunch population in order to reach the nominal luminosity, so we can conclude that for the microwave point of view we do not obtain big advantages in increasing the momentum compaction factor. On the other hand, a higher momentum compaction factor gives, as we already said, a larger synchrotron tune which could have some beneficial effects on the transverse mode coupling instability, as well as on the energy calibration [39]. Fig.5.6 shows, first, the results in this condition obtained with PyHT and Delphi, and how these are in good agreement. In Fig.5.7 we observe, in particular, an increase of the TMCI threshold. Fig. 5.8 shows the TMCI analysis using a nominal bunch length of 15.2 mm, which also includes the beamstrahlung effect. In [39] we discussed what happens if we take into account beamstrahlung and collective effects in collision. In fact, we see the blow-up of the horizontal beam size σ_x/σ_{x0} as a function of the bunch population.

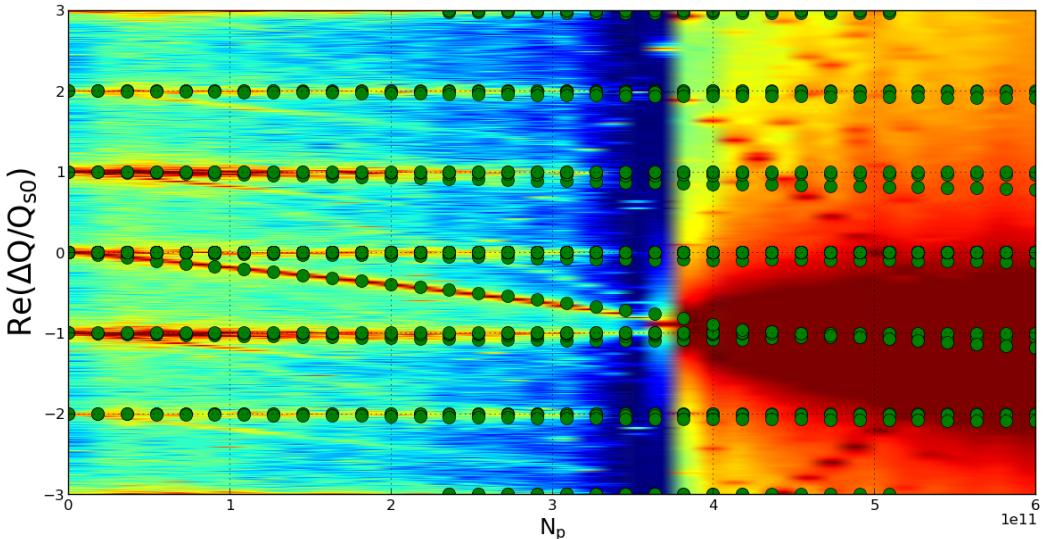


Figure 5.6: Transverse dynamics analysis considering the transverse RW with a higher momentum compaction and bunch length of 4.5 mm, non-colliding bunches. We compared the result obtained by using PyHT with the results obtained by using Delphi code.

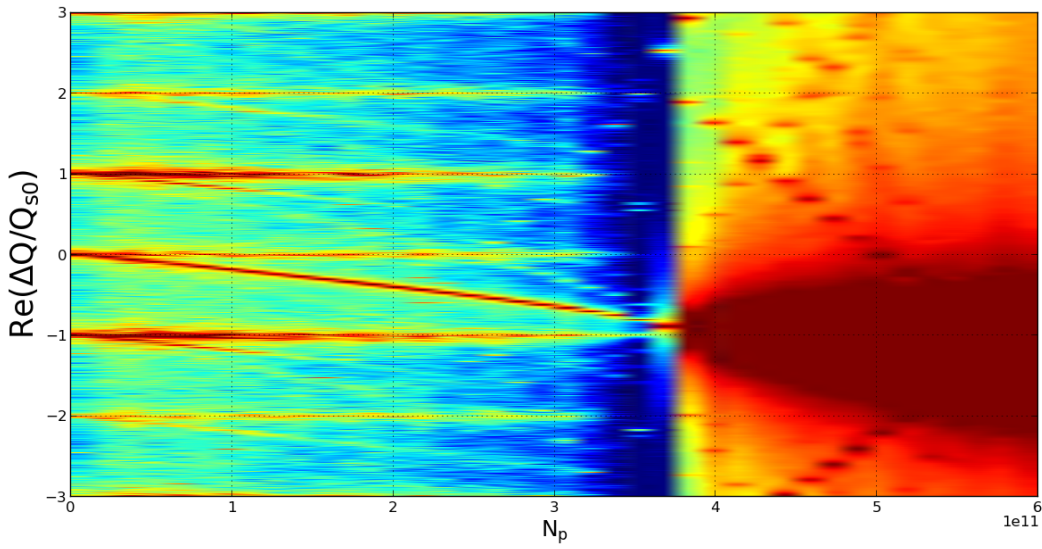


Figure 5.7: Removing Delphi simulation results from Fig. 5.6: Transverse dynamics analysis considering the transverse RW with a higher momentum compaction and bunch length of 4.5 mm, non-colliding bunches.

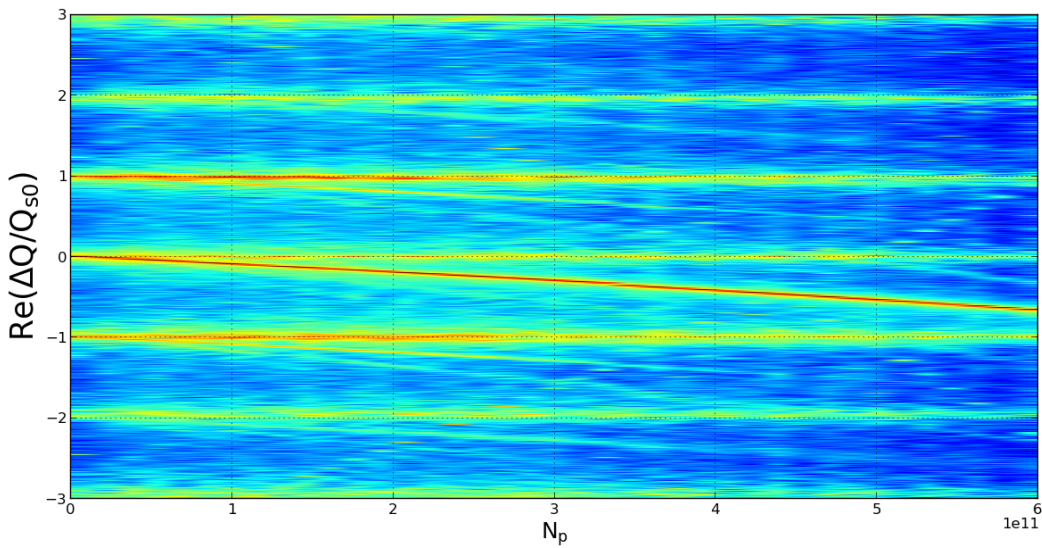
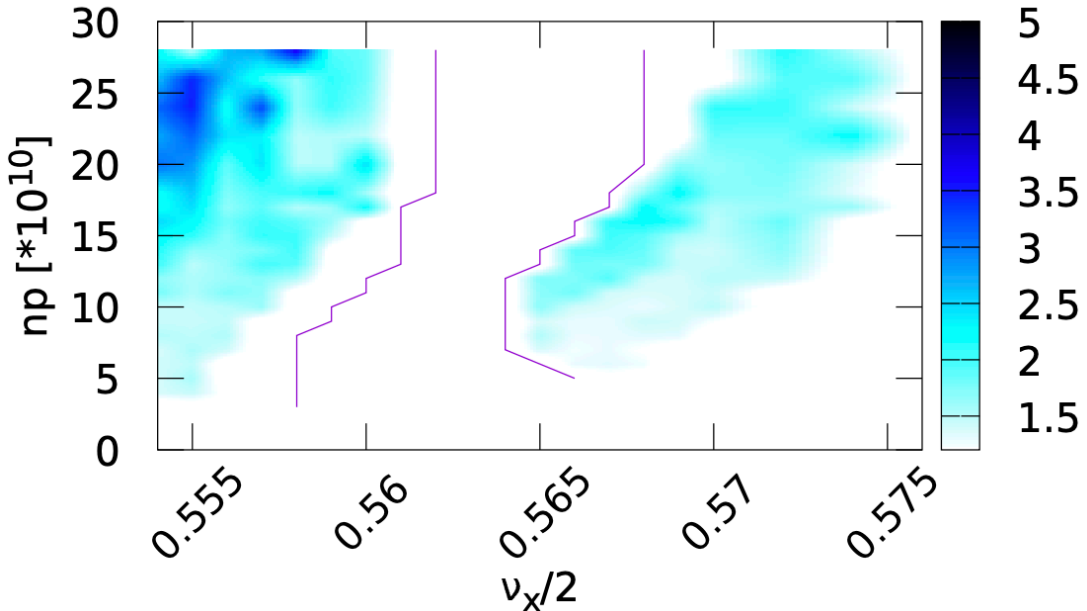


Figure 5.8: Transverse dynamics analysis considering the transverse RW with a higher momentum compaction and bunch length of 15.2 mm, considering colliding bunches, so the beamstrahlung effect.

Finally, if we take into account the beamstrahlung and collective effects in collision, we obtain Fig5.9 which shows the horizontal beam size blow-up.

RF frequency	Voltage	Phase
400MHz	100MV	156.1°
1200MHz	23.4MV	-11.1°

Table 5.1: Harmonic cavity parameters**Figure 5.9:** Blow-up of the horizontal beam size σ_x/σ_{x_0} as a function of the bunch population and of the horizontal tune scan for arc cell of $45^\circ/45^\circ$.

Comparing this figure with the Fig. 3.10, in the chapter 3, we can observe that the safe tune areas are much larger and less current dependent, and the horizontal size blow-up is much lower for the tunes affected by the X–Z instability. For example, if we have a bunch population up to $N_p = 28 \times 10^{10}$ we can find a stable area, so the X–Z instability is suppressed in a horizontal tune region with a width of about 0.004–0.005. Also, even if the region is not so large, it is anyway a good condition from the machine operation point of view. Moreover, for the higher bunch population, the number of bunches is reduced to 10102 with respect to the original of CDR Table 2.1 of 16640.

5.3 Higher harmonic cavity

Another possible solution to suppress the X–Z instability and at the same time the MW instability is increasing the nominal bunch length using a higher harmonic cavity system. On the other hand, since the quantity of the horizontal beam-beam tune shift scales inversely to the second power of the bunch length, this means that longer bunches reduce this quantity and that this helps for the suppression of the X–Z instability. Moreover, the increasing of the bunch length decreases the wake potential due to the coupling impedance, so longer bunches produce less strong collective effects [39]. By using a higher harmonic cavity, we have some additional advantages: for example, longer bunches can be achieved without momentum acceptance reduction or, a reduction of synchrotron tune and longer bunches in collision result in a smaller energy spread due to beamstrahlung. In table 5.1 a possible harmonic cavity configuration is shown. The comparison of bunch length and

energy spread as a function of the bunch population with and without a harmonic cavity is shown in Fig. 5.10. The results are obtained by using the SBSC [65] code without collision. These codes use macro-particles, and they slice the bunch distribution in order to evaluate the convolution integral for the determination of the collective effects.

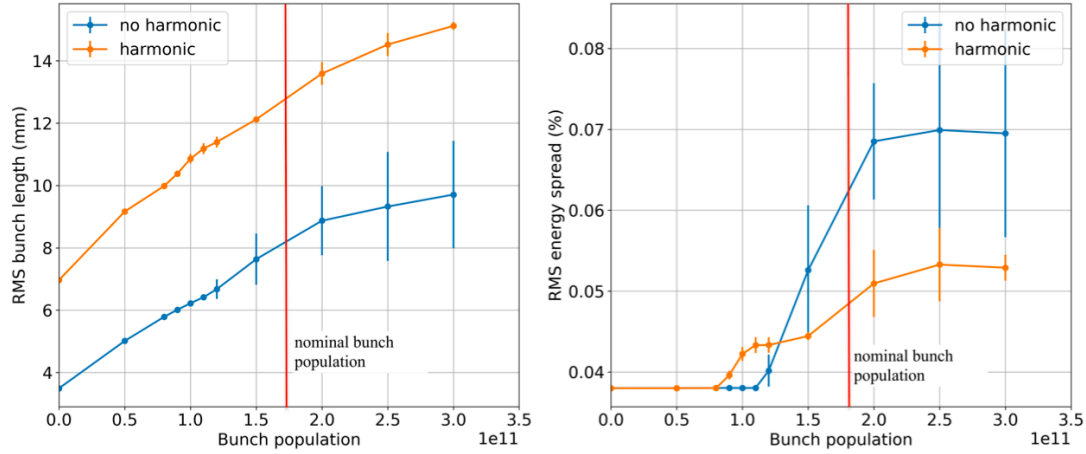


Figure 5.10: Bunch length, on the left, and energy spread, on the right, as a function of bunch population with and without the higher harmonic cavity system.

From the comparison, we observe that we have an increase of the bunch length by almost a factor of 2 and that the MW instability threshold becomes lower. However, the energy spread results quite lower at nominal bunch population, so the instability is less strong with respect to the case without the harmonic cavity system. The harmonic cavity lowers the threshold of the microwave instability, as it reduces the effective synchrotron tune.

Of course there are some issues in using a higher harmonic system, as, for example, the transient beam loading in the multi-bunch regime, an additional impedance due to the harmonic cavity, and the energy calibration due to the lower synchrotron frequency. These points require careful investigation. On the other hand, we can assert that there is no X-Z instability with harmonic cavity by considering, of course, the impedances evaluated so far in contrast to the case without harmonic cavity. The reason why the collective effects are mitigated is due to the combined change of some important beam parameters, with respect to Table 2.1, of the CDR configuration. In fact, we can observe a lower horizontal tune shift $\xi_x = 0.002$, a large Piwinski angle $\phi = 39$, a lower half-synchrotron tune $v_S/2 = 0.005$, and a different bunch shape.

5.4 Feedback system and transverse coupled beam instability.

In chapter 4 we analyzed the transverse dynamics, and we saw how the TMCI is a very strong instability. In addition to this single bunch instability, the transverse RW impedance also has an important effect on the multi-bunch case. Indeed, the transverse long range RW wakefield, or, correspondent, in frequency domain, the low frequency behaviour of the real part of the impedance, can excite the transverse coupled bunch instability. In this case, we can consider the motion of the entire beam as the sum of coherent coupled bunch modes. The growth rate of $m = 0$, the lowest

azimuthal mode, for a Gaussian bunch is given by [66]:

$$\alpha_{\mu,\perp} = -\frac{cI}{4\pi\frac{E_0}{e}Q_\beta} \sum_{q=-\infty}^{\infty} \operatorname{Re}[Z_\perp(\omega_q)] G_\perp(\sigma_\tau \omega'_q); \quad (5.7)$$

where I is the total beam current, E_0 the machine energy, Q_β the betatron tune, σ_τ the RMS bunch length in time, G_\perp a form factor due to the bunch shape that for FCC-ee can be assumed to be equal to 1.

$$\operatorname{Re}[Z_\perp(\omega_q)] = \operatorname{sgn}(\omega) \frac{C}{2\pi b^3} \sqrt{\frac{2Z_0 c}{\sigma_c |\omega|}} \quad (5.8)$$

with:

$$\omega_q = (qN_b + \mu + Q_\beta)\omega_0 \quad (5.9)$$

and:

$$\omega'_q = \omega_q + \xi \frac{\omega_\beta}{\eta} \quad (5.10)$$

The number of bunches is N_b , the chromaticity is ξ , ω_0 is the revolution frequency and μ is an integer number from 0 to $N_b - 1$ representing a coupled bunch mode. The instability occurs when σ_μ is positive, for example, when we evaluate, with negative frequency, the real part of the transverse RW impedance. Positive frequencies give rise instead to damped oscillations. Additionally, the transverse impedance is inversely proportional to the square root of the frequency. Therefore, the most dangerous coupled bunch mode is the one with a coherent frequency ω_q closest to zero and negative. Figure 5.11 shows the beam spectrum of some of the most dangerous coupled bunch modes and the transverse impedance of a 35 mm copper pipe without low-frequency coating.

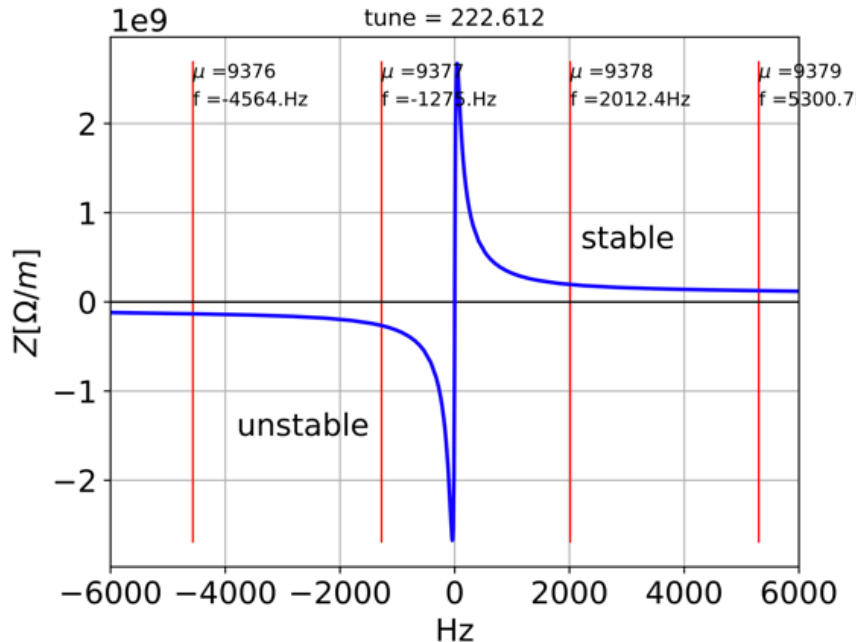


Figure 5.11: Transverse wakefield as a function of frequency.

Fig. 5.12 shows the $m = 0$ growth rate as a function of the fractional part of the tune. The rise

times are in the range of few milliseconds, and, they can be cured by transverse bunch by bunch feedback systems. However, due to the large circumference of the machine for the case of FCC-ee, these rise times correspond to few turns, about 6 revolution periods, and for that a new challenging and robust feedback system is required. In [67] some schemes to cope with this fast instability have been proposed. A feedback system, on the other hand, can have a destabilizing effect on the transverse single bunch instability. This is called ITSR (Imaginary Tune Split and Repulsion) instability [68]. It is not due to the mode coupling, but it is an instability of the -1 azimuthal single bunch mode. A similar instability has been observed at SuperKEKB [69].

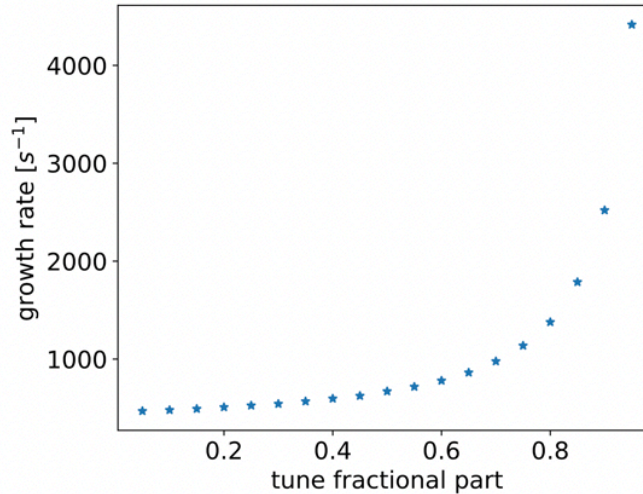


Figure 5.12: Growth rate of the coupled bunch as function of the tune fractional part.

Figure 5.13 shows an example of ITSR instability for FCC-ee obtained with PyHEADTAIL considering only the transverse wakefield. We can see that the shift of the "0" mode towards "-1" is suppressed by the feedback (we used here a pure resistive transverse damper) but, at a quite low threshold, an instability of the mode "-1" appears. This instability has been produced by the same wake which produced the TMCI. The feedback, that in this case has a damping time of 10 revolution periods, acts on the mode 0 avoiding the coupling, but it produces this new instability of the mode -1 at about 17×10^{10} particles per bunch. In Fig. 5.14 we show the turn by turn intra-bunch motion below the instability threshold showing no coherent motion, while in Fig. 5.15 we observe a typical instability of mode -1 at a bunch population of 18×10^{10} .

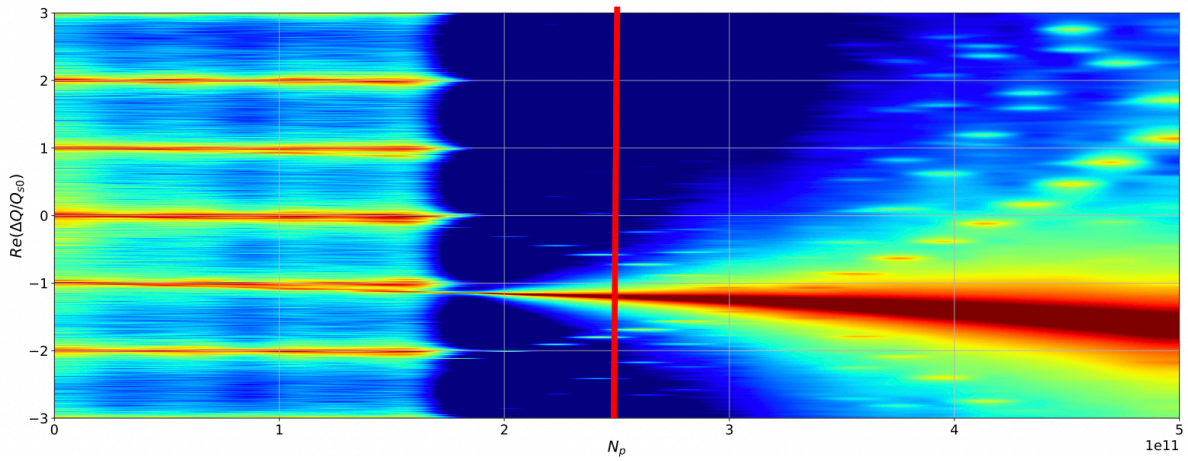


Figure 5.13: Transverse mode coupling instabilities analysis considering only the transverse wakefield and using resistive feedback after 10 turns damping time.

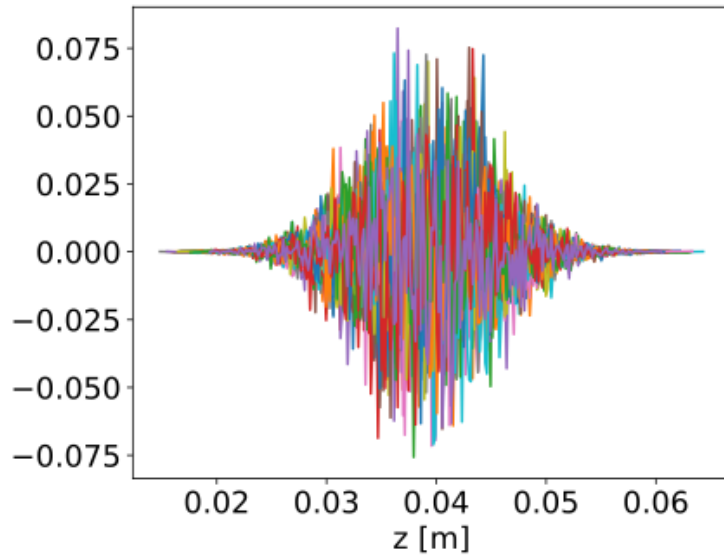


Figure 5.14: Turn by turn intra-bunch motion at a bunch population of 16×10^{10}

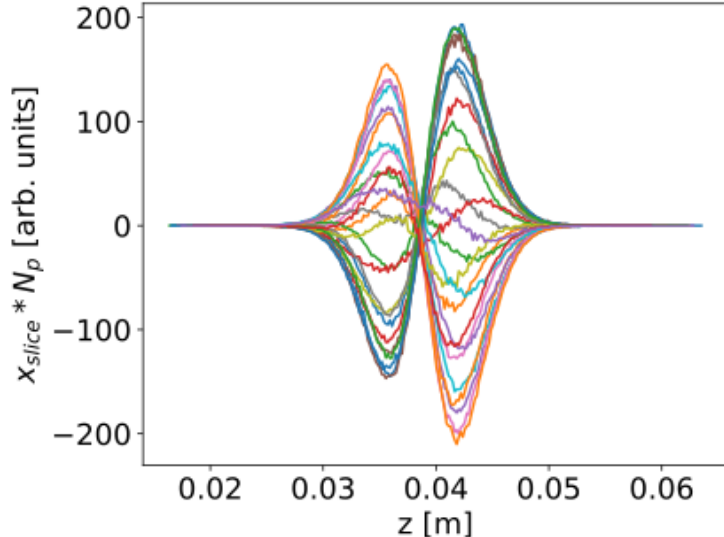


Figure 5.15: Turn by turn, intra-bunch motion at a bunch population of 18×10^{10}

The longitudinal wakefield in this condition, contrary to the TMCI case, can be useful for the instability suppression because the spread in the synchrotron tune due to the longitudinal wakefield helps to mitigate the ITSR instability due to the Landau damping. In fact, the effect of the longitudinal wake helps to increase the instability threshold, as shown in Fig. 5.16. In this case, the instability threshold increases to 34×10^{10} particles per bunch. Additionally, as we can see from Fig. 5.17, the -1 instability is much weaker.

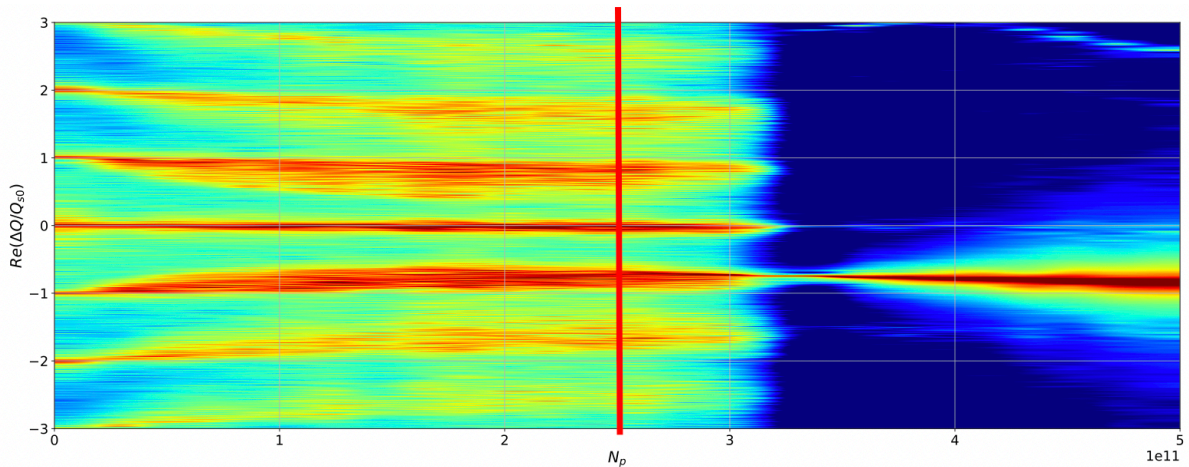


Figure 5.16: TMCI analysis considering both the longitudinal and transverse wakefield using a resistive feedback with 10 turns damping time.

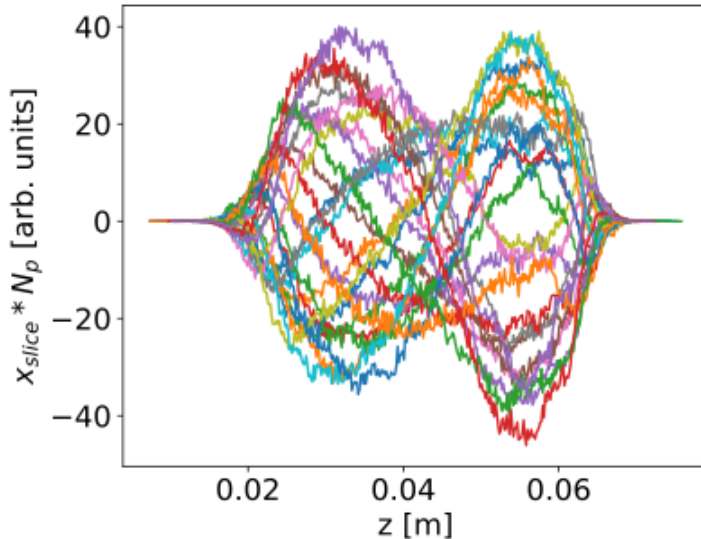


Figure 5.17: Turn by turn intra-bunch motion at intensity of 34×10^{10} considering both the longitudinal and transverse wakefield.

On the other hand, applying a stronger resistive feedback, with 4 turns damping time, which should be what we need to suppress the coupled bunch instability, we can increase the instability threshold, Fig. 5.18. Precisely, in Fig. 5.19 we can see an instability close to an intensity of 46×10^{10} .

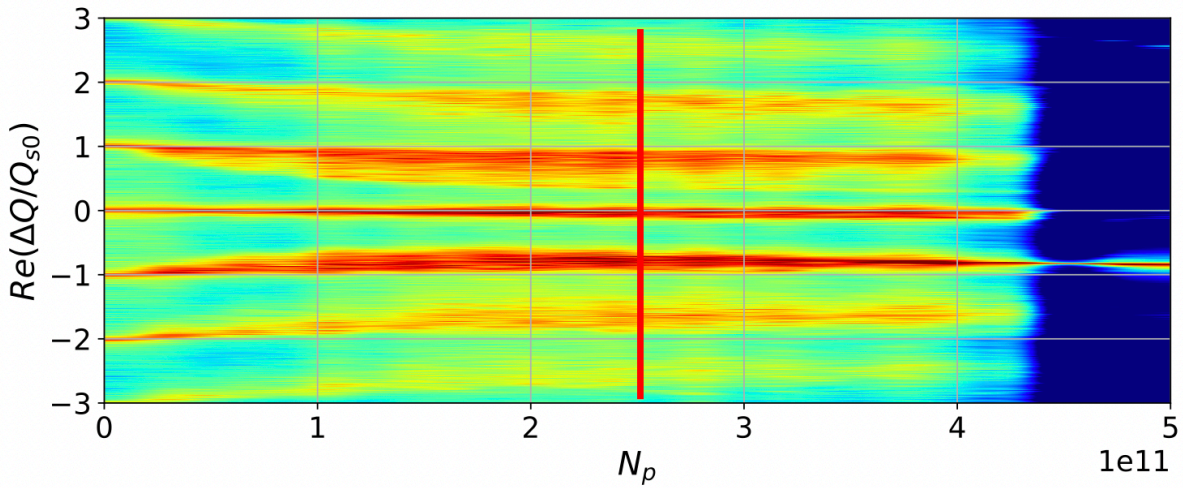


Figure 5.18: TMCI analysis considering both the longitudinal and transverse wakefield using a stronger resistive feedback, with 4 turns damping time.

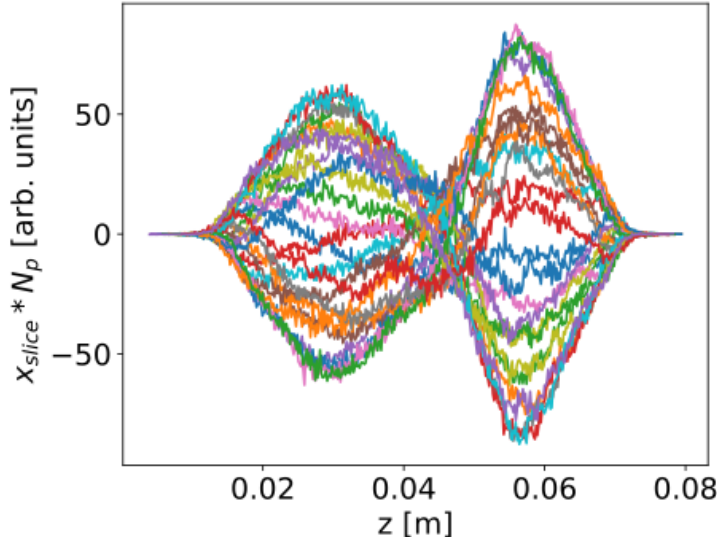


Figure 5.19: Turn by turn intra-bunch motion at a bunch population of 46×10^{10} considering both the longitudinal and transverse wakefield.

In these cases, we are considering just the single bunch at nominal bunch length, without introducing the beamstrahlung effect. Future studies will investigate the effect of beamstrahlung, which makes the beam longer and reduces the longitudinal wakefield effect. In addition, we also need to better understand what happens if we use reactive feedback.

5.5 Reduction of β function at the interaction point

Another possible option to mitigate the X-Z coherent instability is related to the reduction of betatron function at the interaction point β_x^* . In fact, the X-Z instability threshold is inversely proportional to the horizontal betatron function at the interaction point from the equation:

$$N_{th} \propto \frac{\alpha_c \sigma_p \sigma_z}{\beta_x^*} \propto \frac{v_s}{\xi_x} \quad (5.11)$$

Certainly, this method has its downsides. In fact, it generates a reduction of the dynamic aperture and of the momentum acceptance and for that reason a careful design of the machine optics is necessary. A good compromise for having an acceptable dynamic aperture is $\beta_x^* = 10\text{cm}$. It has been proposed in [70]. The parameter list with this new lattice has a lower single bunch intensity and a horizontal beam-beam parameters ξ_x almost a factor of two lower than that foreseen in the CDR [3], Table 2.1. Moreover, the necessary stable area is proportional to ξ_x so we expect an additional stabilizing effect.

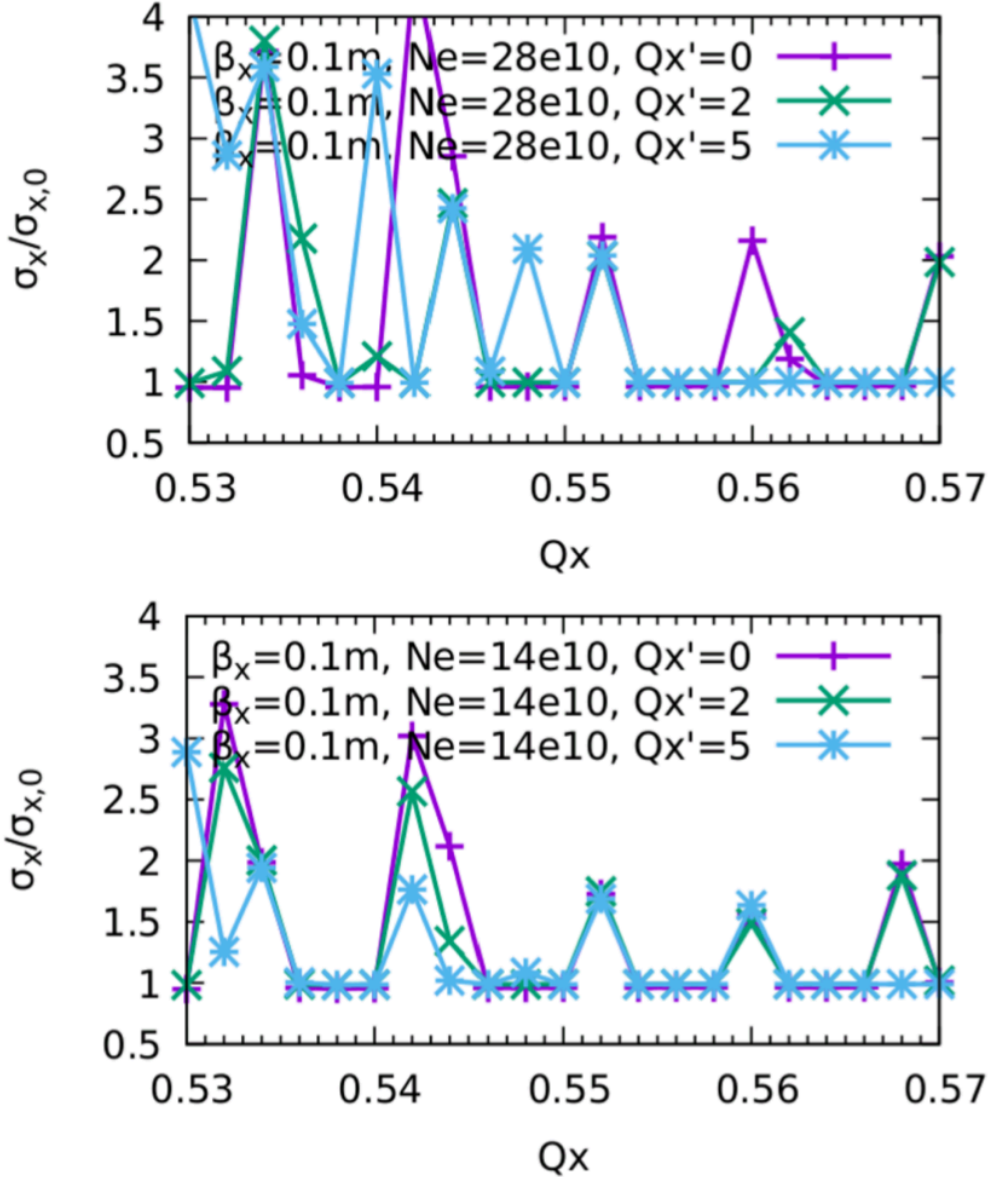


Figure 5.20: Normalized horizontal beam size σ_x / σ_{x0} as a function of horizontal tune for a bunch population of $N_p = 2.8 \times 10^{11}$ (on the top) and $N_p = 1.4 \times 10^{11}$ (on the bottom) at different chromaticities (Q'_x) with $\beta_x^* = 10\text{cm}$ [3].

In Fig. 5.20 the results of beam-beam simulations with a bunch population of $N_p = 2.8 \times 10^{11}$ and 1.4×10^{11} and considering a chromaticity of 0, 2 and 5 are reported. These figures can be compared with Fig.3.10 with $\beta^* = 10\text{cm}$. From the figures, we can assert that the situation is better than the one that has $\beta_x^* = 15\text{cm}$. In fact, we have, around a horizontal tune of 0.56, two regions of stabilities at both intensities. It is important to understand how much luminosity we would lose operating the machine with a reduced β_x^* . Fig. 5.21 shows that at high intensity $N_p = 2.8 \times 10^{11}$ and a chromaticity of 5, we lose about 15% of luminosity per IP, but this parameter still remains in a good range, above $180 < 10^{34}/(\text{cm}^2\text{s})$.

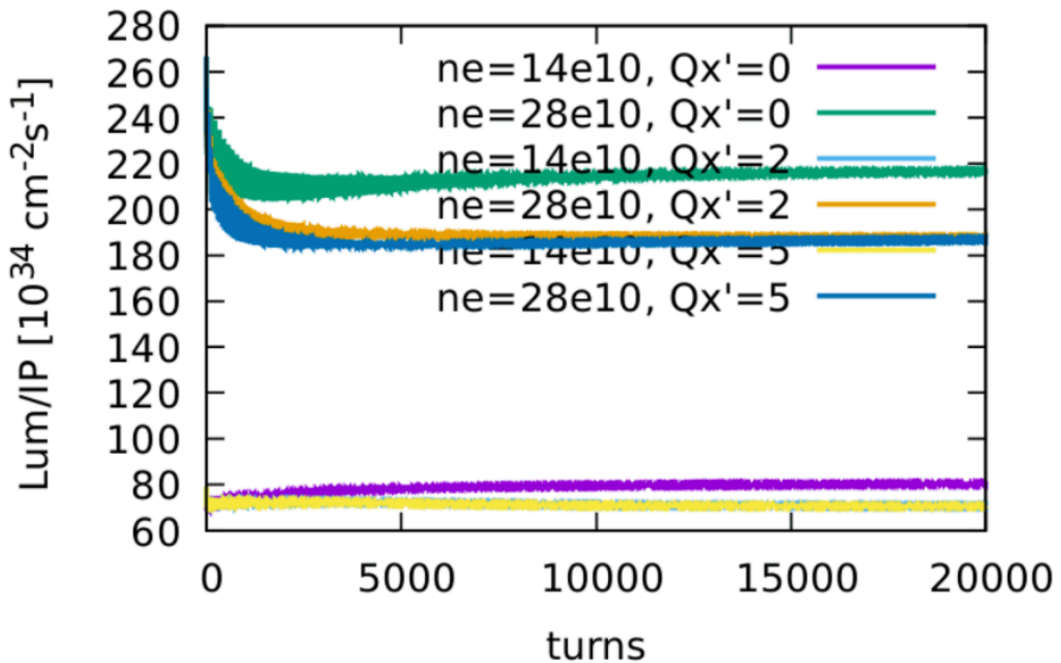


Figure 5.21: Luminosity per IP at different chromaticities with $Np = 2.8 \times 10^{11}$ and $Np = 1.4 \times 10^{11}$ and with $\beta_x^* = 10\text{cm}$ [3].

Chapter 6

Conclusion

This Ph.D. thesis is focused on the collective effects and impedance induced beam instabilities for FCC–ee. The study results presented here reveal the importance of collective effects for the operation of this first stage of the Future Circular Collider (FCC), an ambitious post-LHC accelerator project, a study of whose feasibility has been requested by the European Strategy for Particle Physics.

The collective effects are particularly important at the Z resonance due to the low energy and the high beam current. Simulations have been performed for the main elements of the collider rings to characterize and optimize the impedance of important machine components.

Collective effects were studied for a new parameter list and an updated impedance model. The further developed impedance model was crucial for a better understanding of single bunch and multi bunch instabilities, thus allowing the identification of adequate mitigation techniques for ensuring beam stability during operation.

In addition, in order to validate the predicted effects of the impedance on the beam dynamics, two collective-effect codes have been compared, namely PyHEADTAIL, a tracking simulations code, and the Vlasov solver Delphi. The results of the comparison demonstrate a good agreement between the two codes. Besides the resistive wall (RW) of the large ring, the geometric impedance of other important machine components has been evaluated. In general, the contribution of these other elements is smaller than that of the RW; so far, only the bellows and the collimators have been identified as other important sources of impedance.

Our study of collective effects, without beam-beam interaction, but with both longitudinal and transverse wakefields simultaneously present, reveals a lower threshold for the transverse mode coupling instability (TMCI) than the one generally estimated by considering only the transverse plane. The strong effect of the longitudinal wake fields on the TMCI threshold arises from its effect on the particles' synchrotron tunes. As a result of this interplay, it would not be possible to reach the nominal single bunch intensity in single-beam operation without collision.

The longitudinal beam coupling impedance is also responsible for bunch lengthening, and, further, it can also increase the energy spread if the microwave instability threshold is exceeded. As for this microwave instability, the nominal bunch intensity is only slightly above the simulated instability threshold, but the instability is expected to be greatly suppressed in collision, thanks to the strong beamstrahlung. Due to the small size of the intense colliding beams at FCC–ee, the beamstrahlung effect leads to a substantial bunch lengthening and concomitant energy spread

increase, thereby moving the beam parameters away from the threshold condition.

In addition, an analysis of the interplay between beam-beam interaction and the longitudinal beam coupling impedance for the FCC–ee collider, indicates that this combined effect can drastically affect the machine performance.

Moreover, since the impedance is expected to increase with the addition of more components during the vacuum chamber design, the situation could degrade further. That is why we have undertaken studies of eventual mitigation techniques.

In particular, we have shown that the use of harmonic cavities can help to suppress the x - z instability. The simulations have demonstrated that with harmonic cavities, no instability is encountered over the entire tune range of interest for all the considered bunch intensities. However, the harmonic cavities can have an impact on other beam dynamics aspects, such as on the transient beam loading in the multi-bunch regime and on the beam energy calibration. Also, the cavities themselves represent an additional source of coupling impedance. So, these aspects have to be further investigated.

We have also analysed the consequences of a higher momentum compaction factor, which appears to be an even better solution. In fact, the simulations demonstrate that, with the larger value of α_C , the microwave instability becomes weaker and, in collision, the good tune area remains comfortably wide, even at higher bunch intensity. More specifically, with a momentum compaction factor of $\alpha_C = 2.5 \times 10^{-5}$, the design luminosity can be achieved with a reduced number of 10102 bunches, instead of 16640, by increasing the bunch intensity up to 2.8×10^{11} particles per bunch.

However, our simulations indicate that there are not sufficiently large horizontal tune areas to operate the machine without incurring the x - z coherent instability. One possible mitigation could be to reduce the horizontal beta function at the IP. It has been found that with $\beta_x^* = 10\text{cm}$ instead of 15 cm there are enough wide working tune areas even with collisions at 4 IPs, the proposed new configuration.

Moreover, we analysed the impact of the chromaticity on the TMCI and the x - z coherent instability, and we found that a positive chromaticity helps to increase the intensity threshold.

Additionally, we saw that TMCI can also be mitigated by using a resistive transverse damper, which, in combination with the longitudinal wakefield effect, increases the TMCI intensity threshold.

Today, work is still in progress to update the beam impedance model in accordance with the vacuum-chamber design evolution. For example, the impedance model must follow the refinement of the FCC–ee collimation system, which is an important source of impedance, in particular in the transverse plane.

Bibliography

- [1] Eleonora Belli. *Coupling impedance and single beam collective effects for the Future Circular Collider (lepton option)*. PhD thesis, Rome U., 2019.
- [2] I Agapov, M Benedikt, A Blondel, M Boscolo, O Brunner, M Chamizo Llatas, T Charles, D Denisov, W Fischer, E Gianfelice-Wendt, et al. Future circular lepton collider fcc-ee: Overview and status. *arXiv preprint arXiv:2203.08310*, 2022.
- [3] M Migliorati, C Antuono, E Carideo, Y Zhang, and M Zobov. Impedance modelling and collective effects in the future circular e^+e^- collider with 4 ips. *arXiv preprint arXiv:2204.04616*, 2022.
- [4] Vladimir Shiltsev, Yuri Alexahin, Alexey Burov, and Alexander Valishev. Landau damping of beam instabilities by electron lenses. *Physical Review Letters*, 119(13):134802, 2017.
- [5] https://indico.in2p3.fr/event/27968/contributions/115478/attachments/74058/106579/Fcc_Behtouei.pdf.
- [6] https://gitlab.cern.ch/ecarideo/FCCee_IW_Model.
- [7] D Leshenok, S Nikitin, Y Zhang, and M Zobov. Combined influence of beamstrahlung and coupling impedance on beam energy spread and length in future lepton colliders. *Physical Review Accelerators and Beams*, 23(10):101003, 2020.
- [8] David Amorim. *Study of the transverse mode coupling instability in the CERN Large Hadron Collider*. PhD thesis, Université Grenoble Alpes, 2019.
- [9] Georges Aad, Tatevik Abajyan, B Abbott, J Abdallah, S Abdel Khalek, Ahmed Ali Abdelalim, R Aben, B Abi, M Abolins, OS AbouZeid, et al. Observation of a new particle in the search for the standard model higgs boson with the atlas detector at the lhc. *Physics Letters B*, 716(1):1–29, 2012.
- [10] Serguei Chatrchyan, Vardan Khachatryan, AM Sirunyan, A Tumasyan, Wolfgang Adam, T Bergauer, M Dragicevic, J Erö, C Fabjan, M Friedl, et al. Observation of a new boson with mass near 125 gev in pp collisions at $\sqrt{s} = 7$ and 8 TeV. *Journal of High Energy Physics*, 2013, 2013.
- [11] Giorgio Apollinari, O Brüning, Tatsushi Nakamoto, and Lucio Rossi. High luminosity large hadron collider hl-lhc. *arXiv preprint arXiv:1705.08830*, 2017.

[12] European Strategy Group Collaboration et al. 2020 update of the european strategy for particle physics, 2020.

[13] Michael Benedikt and Frank Zimmermann. Towards future circular colliders. *Journal of the Korean Physical Society*, 69(6):893–902, 2016.

[14] Michael Benedikt, Volker Mertens, Francesco Cerutti, Werner Riegler, Thomas Otto, Davide Tommasini, Laurent Jean Tavian, Johannes Guteleber, Frank Zimmermann, Michelangelo Mangano, et al. Fcc-hh: The hadron collider: future circular collider conceptual design report volume 3. *Eur. Phys. J. Spec. Top.*, 228(CERN-ACC-2018-0058):755–1107, 2018.

[15] Asmâa Abada, Marcello Abbrescia, Shehu S AbdusSalam, I Abdyukhanov, Jose Abelleira Fernandez, A Abramov, M Aburaia, AO Acar, PR Adzic, P Agrawal, et al. Fcc-ee: the lepton collider. *The European Physical Journal Special Topics*, 228(2):261–623, 2019.

[16] Frank Zimmermann, Michael Benedikt, Daniel Schulte, Jorg Wenninger, et al. Challenges for highest energy circular colliders. In *5th Int. Particle Accelerator Conf.(IPAC'14), Dresden, Germany, June 15-20, 2014*, pages 1–6. JACOW Publishing, Geneva, Switzerland, 2014.

[17] Ties Behnke, James E Brau, Brian Foster, Juan Fuster, Mike Harrison, James McEwan Patterson, Michael Peskin, Marcel Stanitzki, Nicholas Walker, and Hitoshi Yamamoto. The international linear collider technical design report-volume 1: Executive summary. *arXiv preprint arXiv:1306.6327*, 2013.

[18] Lyn Evans and Shinichiro Michizono. The international linear collider machine staging report 2017. *arXiv preprint arXiv:1711.00568*, 2017.

[19] Markus Aicheler, P Burrows, M Draper, Terence Garvey, P Lebrun, K Peach, N Phinney, H Schmickler, Daniel Schulte, and N Toge. A multi-tev linear collider based on clic technology: Clic conceptual design report. Technical report, SLAC National Accelerator Lab., Menlo Park, CA (United States), 2014.

[20] The CLIC, MJ Boland, U Felzmann, PJ Giansiracusa, TG Lucas, RP Rassool, C Balazs, TK Charles, K Afanaciev, I Emeliantchik, et al. Updated baseline for a staged compact linear collider. *arXiv preprint arXiv:1608.07537*, 2016.

[21] Jie Gao. Cepc-sppc accelerator status towards cdr. *International Journal of Modern Physics A*, 32(34):1746003, 2017.

[22] FCC collaboration et al. Fcc physics opportunities: Future circular collider conceptual design report volume 1. *European Physical Journal C*, 79(6):474, 2019.

[23] Asmaa Abada, Marcello Abbrescia, Shehu S AbdusSalam, I Abdyukhanov, Jose Abelleira Fernandez, A Abramov, M Aburaia, AO Acar, PR Adzic, P Agrawal, et al. Fcc-hh: The hadron collider. *The European Physical Journal Special Topics*, 228(4):755–1107, 2019.

[24] Katsunobu Oide, M Aiba, S Aumon, M Benedikt, A Blondel, A Bogomyagkov, M Boscolo, H Burkhardt, Y Cai, A Doblhammer, et al. Design of beam optics for the future circular collider e+ e- collider rings. *Physical Review Accelerators and Beams*, 19(11):111005, 2016.

[25] Yannis Papaphilippou, F Zimmermann, L Rinolfi, M Aiba, Dmitry Shwartz, and K Oide. Design guidelines for the injector complex of the fcc-ee. Technical report, 2016. <https://accelconf.web.cern.ch/ipac2016/papers/thpmr042.pdf>.

[26] S Ogur, K Oide, Y Papaphilippou, F Zimmermann, and D Shatilov. Bunch schedules for the fcc-ee pre-injector. *energy [GeV]*, 45(80):120, 2018.

[27] Salim Ogur, Pavel Martyshkin, Ozgur Etisken, Robert Chehab, Iryna Chaikovska, Fusashi Miyahara, Danila Nikiforov, Kazuro Furukawa, Yannis Papaphilippou, Bastian Härer, et al. Overall injection strategy for fcc-ee. *JACOW*, 2019.

[28] O Etisken, F Antoniou, Y Papaphilippou, and AK Ciftci. Pre-booster ring considerations for the fcc e+e- injector. In *Proceedings of Int. Particle Accelerator Conf.(IPAC'18), Vancouver, Canada*, 2018.

[29] B Härer, BJ Holzer, Y Papaphilippou, and T Tydecks. Status of the fcc-ee top-up booster synchrotron. In *Proceedings of Int. Particle Accelerator Conf.(IPAC'18), Vancouver, Canada*, 2018.

[30] Nicolò Biancacci. *Improved techniques of impedance calculation and localization in particle accelerators*. PhD thesis, Rome U., 2014.

[31] Alexander Wu Chao. Physics of collective beam instabilities in high energy accelerators. *Wiley series in beam physics and accelerator technology*, 1993.

[32] L Palumbo, Vittorio G Vaccaro, and M Zobov. Wake fields and impedance. *arXiv preprint physics/0309023*, 2003.

[33] Benoit Salvant. Impedance model of the cern sps and aspects of lhc single-bunch stability. Technical report, EPFL, 2010.

[34] Perry B Wilson and James E Griffin. High energy electron linacs; application to storage ring rf systems and linear colliders. In *AIP conference proceedings*, volume 87, pages 450–555. American Institute of Physics, 1982.

[35] <https://gitlab.cern.ch/IRIS/IW2D/-/blob/master/README.md>.

[36] Nicolas Mounet and Elias Métral. Impedances of two dimensional multilayer cylindrical and flat chambers in the non-ultrarelativistic case. Technical report, <http://hb2010.web.psi.ch/proceedings/index.htm>, 2010.

[37] M Migliorati, E Belli, and M Zobov. Impact of the resistive wall impedance on beam dynamics in the future circular e+ e- collider. *Physical Review Accelerators and Beams*, 21(4):041001, 2018.

[38] R. Kersevan. personal communication.

[39] M Migliorati, E Carideo, D De Arcangelis, Y Zhang, and M Zobov. An interplay between beam-beam and beam coupling impedance effects in the future circular ee collider. *The European Physical Journal Plus*, 136(11):1190, 2021.

[40] M Migliorati, L Palumbo, C Zannini, N Biancacci, and VG Vaccaro. Resistive wall impedance in elliptical multilayer vacuum chambers. *Physical Review Accelerators and Beams*, 22(12):121001, 2019.

[41] :<https://github.com/PyCOMPLETE/PyHEADTAIL>.

[42] <https://www.cst.com>.

[43] <http://abci.kek.jp/>.

[44] https://indico.cern.ch/event/459623/contributions/1131172/attachments/1225046/1792916/Zagorodnov_ECHO_APPs.pdf.

[45] T Ishibashi, S Terui, and Y Suetsugu. Low impedance movable collimators for superkek. *Proceedings of the IPAC*, 17:14–19, 2017.

[46] A. Abramov. personal communication.

[47] <https://docs.github.com/en/get-started/quickstart/create-a-repo>.

[48] Pantaleo Raimondi, Dmitry N Shatilov, and Mikhail Zobov. Beam-beam issues for colliding schemes with large piwinski angle and crabbed waist. *arXiv preprint physics/0702033*, 2007.

[49] Yuan Zhang, Na Wang, Chuntao Lin, Dou Wang, Chenghui Yu, Kazuhito Ohmi, and Mikhail Zobov. Self-consistent simulations of beam-beam interaction in future e+ e- circular colliders including beamstrahlung and longitudinal coupling impedance. *Physical Review Accelerators and Beams*, 23(10):104402, 2020.

[50] GE Fisher. A brief note on the effect of bunch length on the luminosity of a storage ring with low beta at the interaction point. *SPEAR-154*, 1972.

[51] VI Telnov. Restriction on the energy and luminosity of e+ e- storage rings due to beamstrahlung. *Physical Review Letters*, 110(11):114801, 2013.

[52] K Ohmi, N Kuroo, K Oide, D Zhou, and F Zimmermann. Coherent beam-beam instability in collisions with a large crossing angle. *Physical review letters*, 119(13):134801, 2017.

[53] Nami Kuroo, Kazuhito Ohmi, Katsunobu Oide, Demin Zhou, and Frank Zimmermann. Cross-wake force and correlated head-tail instability in beam-beam collisions with a large crossing angle. *Physical Review Accelerators and Beams*, 21(3):031002, 2018.

[54] Dmitry Shatilov. submitter: Fcce-e parameter optimization. *ICFA Beam Dyn News*, 72:30–41, 2017.

[55] B Zotter. Transverse instabilities of relativistic particle beams in accelerators and storage rings. i. Technical report, 1977.

[56] R Boni, A Drago, A Gallo, A Ghigo, F Marcellini, M Migliorati, F Sannibale, M Serio, A Stella, G Vignola, et al. Da ϕ ne accumulator ring coupling impedance measurements. *Nuclear Instruments and Methods in Physics Research Section A: Accelerators, Spectrometers, Detectors and Associated Equipment*, 418(2-3):241–248, 1998.

[57] M Zobov, A Gallo, A Ghigo, F Marcellini, M Migliorati, F Sannibale, and M Serio. Transverse mode coupling instability in the da ϕ ne accumulator ring. *DA Φ NE Technical Note: G-50*, 1998.

[58] Jacques Gareyte. Transverse mode coupling instabilities. In *AIP Conference Proceedings*, volume 592, pages 260–278. American Institute of Physics, 2001.

[59] E Métral and M Migliorati. Longitudinal and transverse mode coupling instability: Vlasov solvers and tracking codes. *Physical Review Accelerators and Beams*, 23(7):071001, 2020.

[60] Nicolas Mounet. Presentation, delphi: an analytic vlasov solver for impedance-driven modes. <https://espace.cern.ch/be-dep-workspace/abp/HSC/Meetings/DELPHI-expanded.pdf>.

[61] Elias Métral. Effect of bunch length, chromaticity, and linear coupling on the transverse mode-coupling instability due to the electron cloud. Technical report, CERN, 2002.

[62] D. Shatilov. 133th fcc-ee optics design meeting & 4th fccis wp2.2 meeting, 'larger momentum compaction at z, as another possible option', march 2021. <https://indico.cern.ch/event/1014189>.

[63] Fatih Yaman, Giovanni Iadarola, Roberto Kersevan, Salim Ogur, Kazuhito Ohmi, Frank Zimmermann, and Mikhail Zobov. Mitigation of electron cloud effects in the fcc-ee collider. *EPJ Techniques and Instrumentation*, 9(1):9, 2022.

[64] L Mether, G Rumolo, and A Oeftiger. Modeling of fast beam-ion instabilities. In *CERN Yellow Rep. Conf. Proc.*, volume 1, pages 63–38, 2018.

[65] M Migliorati, S Persichelli, H Damerau, S Gilardoni, S Hancock, and L Palumbo. Beam-wall interaction in the cern proton synchrotron for the lhc upgrade. *Physical Review Special Topics-Accelerators and Beams*, 16(3):031001, 2013.

[66] King-Yuen Ng. *Physics of intensity dependent beam instabilities*. World Scientific, 2006.

[67] Alessandro Drago. Feedback systems for fcc-ee. *arXiv preprint arXiv:1704.06162*, 2017.

[68] E Métral. Imaginary tune split and repulsion single-bunch instability mechanism in the presence of a resistive transverse damper and its mitigation. *Physical Review Accelerators and Beams*, 24(4):041003, 2021.

[69] Mauro Migliorati, Bruno Spataro, Emanuela Carideo, Mostafa Behtouei, Yuan Zhang, Mikhail Zobov, and Chiara Antuono. Studies and mitigation of collective effects in fcc-ee. *JACoW IPAC*, 2022:1583–1586, 2022.

[70] <https://indico.cern.ch/event/1118299/>.

Acknowledgements

This project is supported from the European Union's Horizon 2020 research and innovation program under grant agreement No 951754. Moreover, I will take this opportunity to thank everyone who has supported and stood by me, especially during this PhD thesis.

Firstly, I would like to thank my professor, Mauro Migliorati, for being my mentor and guiding me through this demanding, but rewarding period. Thanks to his patience, he supports me during the difficult years of pandemic. I would also like to say thanks to my supervisors: Frank Zimmermann for choosing me to participate in this exciting project and gave me the opportunity to enrich my wealth of experience.

I am extremely thankful to all my colleagues and friends who were there for me every time I needed. In particular, I want to mention Barbara, a new wonderful discovery, with who I love to share thoughts and fears. I want to say thanks to brighten up my days when I was feeling a bit sad.

I would also say thanks to my family, who even far, is always with me in my heart and in my mind. A special mention for my little prince Giuseppe and for the little fagiolino, aunt loves you so much.

To my mum, who guides me in the most difficult and important moments...you are my strength, my commitment, my tenacity. She is an example for being determined and showing what fighting for what you want is.

I also want to thank the new family which is entered in my heart suddenly and quickly, bringing in my life so much joy and love. In particular to you, Gen, one of the best people that I have ever met, always kind and ready to help everyone. Entering the family has been an honor for me.

It is necessary to thank you, mio amore, who constantly supports and endures me. You gave me so much energy and so much love, you are the first to believe in myself. You have encouraged me to achieve my goals. Wherever the life will bring us, I cannot imagine my life without our laughs any more.

These past years of doctoral program in addiction with the pandemic have been very tough, I passed through difficult moments, but they gave me the strength and courage to never give up.

